UNIVERSITÀ DEGLI STUDI DI PARMA

Dottorato di ricerca in Fisica

Ciclo XXVI

New developments in CdZnTe semiconductors for X and Gamma-ray detection

Coordinatore:

Prof. Pier Paolo Lottici

Tutor:

Dott..sa Maura Pavesi

Dott. Andrea Zappettini

Dottorando: Nicola Zambelli

The future influences the present just as much as the past.

Friedrich Nietzsche

Acknowledgements

First of all I would like to express my gratitude to Dr. Maura Pavesi and Dr. Andrea Zappettini, for all the supports and patience throughout my student career. I would also like to thank the other members of my research group: Giacomo Benassi, Dr. Davide Calestani, Dr. Marco Villani, Laura Marchini, Dr. Nicola Coppedé, Massimiliano Zanichelli, Daniele Zanaga, Giovanni Piacentini, Nicola Castagnetti, Maurizio Culiolo, Sathish Chander and Dr. Lucio Zanotti; they were always present whenever I needed help.

I would also like to thank Dr. Irfan Kuvvetli for all the suggestions and to have believed in our capabilities.

Thanks to "The Pant" for the beautiful time spent together.

I would also like to express my thank to the person of other group who have all been a fundamental part of my life at IMEM institute and outside: Elisa Bonnini, Matteo Bronzoni called "Bronz", Davide Delmonte, Mari1, Francesco Patini, Edi Gilioli and Paolo Fedeli. I will never forgot the beautiful soccer table match played at "Tecnopolo" game field.

Thanks to Alain and Berselli for all the transmitted enthusiasm during the CZTech period of my life.

Thanks again to Giacomo Benassi, Andrea Zappettini, Davide Calestani and Massimiliano Zanichelli as due2lab s.r.l. partner.

Finally I would especially like to thank my family, my friends and all the person who have loved me for their support and encouragement throughout my studies and my crazy project.

Publication List

[1] A. Zappettini, L. Marchini, M. Zha, G. Benassi, N. Zambelli, L. Zanotti D. Calestani, E. Gombia, R. Mosca, M. Zanichelli, M. Pavesi, N. Auricchio, and E. Caroli. Growth and Characterization of CZT Crystals by the Vertical Bridgman Method for X-Ray Detector Applications. *IEEE TRANSACTIONS ON NUCLEAR SCIENCE*, 58(5, 2):2352–2356, OCT 2011.

[2] N. Zambelli, L. Marchini, M. Zha, and A. Zappettini. Three-dimensional mapping of tellurium inclusions in CdZnTe crystals by means of improved optical microscopy. *JOURNAL OF CRYSTAL GROWTH*, 318(1):1167–1170, MAR 1 2011.

[3] L. Marchini, A. Zappettini, M. Zha, N. Zambelli, A. E. Bolotnikov, G. S. Camarda, and R. B. James. Crystal Defects in CdZnTe Crystals Grown by the Modified Low-Pressure Bridgman Method. *IEEE TRANSACTIONS ON NUCLEAR SCIENCE*, 59(2):264–267, APR 2012.

[4] L. Marchini, N. Zambelli, G. Piacentini, M. Zha, D. Calestani, E. Belas, and A. Zappettini. Characterization of CZT crystals grown by the boron oxide encapsulated vertical Bridgman technique for the preparation of X-ray imaging detectors. *NUCLEAR INSTRUMENTS & METHODS IN PHYSICS RESEARCH A*, 633(1):S92–S94, MAY 2011.

[5] A. Cavallini, B. Fraboni, A. Castaldini, L. Marchini, N. Zambelli, G. Benassi, and A. Zappettini. Defect Characterization in Fully Encapsulated CdZnTe. *IEEE TRANSACTIONS ON NUCLEAR SCIENCE*, 60(4, 2):2870–2874, AUG 2013.

[6] G. Benassi, N. Zambelli, M. Villani, D. Calestani, M. Pavesi, A. Zappettini, L. Zanotti, and C. Paorici. Oriented orthorhombic Lead Oxide film grown by vapour phase deposition for X-ray detector applications. *CRYSTAL RESEARCH AND TECHNOLOGY*, 48(4):245–250, APR 2013.

[7] A. Zappettini, L. Marchini, M. Zha, G. Piacentini, N. Zambelli, G. Benassi, and D. Calestani. Study of the anomalous zinc distribution in vertical Bridgman grown CdZnTe crystals. *CRYSTENGCOMM*, 15:2227–2231, October 2012.

[8] N. Zambelli, L. Marchini, G. Benassi, D. Calestani, E. Caroli, and A. Zappettini. Electroless gold contact deposition on CdZnTe detectors by scanning pipette technique. *JOURNAL OF INSTRUMENTATION*, 7, AUG 2012.

[9] N. Zambelli, L. Marchini, G. Benassi, D. Calestani, and A. Zappettini. Modification of the Luminescence Properties of CZT Crystals Around Tellurium Inclusions. *IEEE TRANSACTIONS ON NUCLEAR SCIENCE*, 59(4, 3):1526–1530, AUG 2012.

[10] A. Zappettini, M. Zha, N. Zambelli, A. E. Bolotnikov, G. S. Camarda, and R. B. James. Crystal defects and charge collection in CZT x-ray and gamma detectors. *Nuclear Science Symposium Conference Record (NSS/MIC), 2010 IEEE*, 1(1):3674–3677, 1 2010.

[11] N. Zambelli, N. Armani, L. Marchini, G. Benassi, D. Calestani, and A. Zappettini. Luminescence properties of CZT crystals in the presence of tellurium inclusions. *Nuclear Science Symposium and Medical Imaging Conference (NSS/MIC), 2011 IEEE*, pages 4668–4671, 2011.

[12] N. Zambelli and A. Zappettini. A method and system for the three-dimensional reconstruction of formations dispersed in a matrix of a material, in particular of inclusions in crystalline matrices (eu patent), 09 2013.

Contents

Introduction

Semiconductor ionizing radiation detectors have experienced a rather rapid development in the last years. Recently, a substantial international effort has been invested in developing a range of compound semiconductors with wide band gap and high atomic number for X-ray and Gamma ray detectors. Among the compound semiconductors Cadmium Zinc Telluride (CdZnTe or simply CZT) is the most promising material for radiation detectors with good energy resolution, high detection efficiency and room temperature operation [1].
Nowadays there is a large number of fields where CdZnTe can be employed as a X-ray and Gamma ray detector. These include medical imaging (SPECT, CT), homeland security (cargo and luggage control), environmental monitoring (control of the background radiation) and astrophysics (study of X and Gamma ray emission from celestial bodies). Industrial research have recently discovered the potential of this material, and began to produce large scale devices based on this large band gap material that can operate at room temperature. CZT properties make it a particular appealing material for the realization of portable and easy to handle devices, unlike other materials, like Si and Ge, that requires cryogenic cooling.

One of the fast growing application fields is the homeland security. The increasing fear of terrorist attacks related to airplane security, the constantly increase of the volume of traveling people and object shipping all over the world, made it a must to create a radiation device able to produce a fast and accurate response. Body and luggage control find a huge market in the airport scanning equipment, and especially in this field, considering the number of people flying everyday from the main airports, the need of a response within a few second is necessary. The use of a highly sophisticated device, like CZT based detectors, reduces also the dose necessary to detect dangerous object in a luggage.

A second, but equally interesting application field is in the medical imaging area. The use of solid state devices reflects in the production of new medical devices, with far higher performances with respect to scintillators or other devices. SPECT (Single Photon Emission

Computed Tomography) or CT (Computed Tomography) are techniques that are becoming more and more common in the preventative medicine or surgical applications and the use of such devices have been a great help in the cure and detection of diseases.

Environmental monitoring is currently performed using Geiger Mueller counters, with this equipment it is not possible to acquire information about the nature of the contamination and the position of the X- ray source. Monitoring consist in two main types of applications: control of the background radiation (controlling the natural X-ray emission by elements present in the soil) and monitoring of the areas in the proximity of nuclear facilities, where the possible poisoning due to a malfunctioning of the facility needs to be controlled constantly.

CZT has always been a focus material in the detection of X-ray emission in the space. Astronomical equipment found it necessary to reduce the dimensions of the detection packet and to improve the photo-sensitivity of the device, in order to acquire the largest amount of information possible.

This thesis includes some efforts and results, reached at IMEM-CNR institute and Physics Department of the University of Parma during the last three years, on understanding of CZT physical properties and on CZT-based device production technology improvements.

- First part of the thesis introduces CZT semiconductor for radiation detection. Basic radiation detection physics is given and CZT strength and weaknesses are reported.

- Second chapter treats the problem of inclusions in CZT crystals. A new diagnostic technique based on near infrared transmission microscopy is proposed by the author of this thesis in order to characterize tellurium inclusions in CZT crystals. By means of the described technique it was possible to perform an interesting study on the role played by these inclusions on the performance of CZT based detectors and on the influence of the latter on transport properties of photo-generated carriers inside the material. All measurements, sample preparation, instrumentation development and data analysis was carried out at IMEM institute by the undersigned except for the X-ray charge collection mapping carried out by Laura Marchini at the National Synchrotron Light Source at Brookhaven National Laboratory (USA).

  The last part of the chapter propose a new approach to eliminate tellurium inclusion in CZT crystals. A novel laser-induced thermo-migration system is proposed and evaluated. Samples preparation were carried out at IMEM institute while laser beam calibrations and

preparation were carried out at Physics Department of Parma University by the author of this thesis.

- Chapter third takes into account the importance of metallization process during the CZT device production. A very interesting technique to realize metal deposition on CZT surfaces is proposed and a special metal deposition equipment was developed. Entire system was designed by the author of this thesis, each part of the equipment was personally evaluated, bought and assembled. The ability to reproduce different pattern geometry was investigated. Furthermore reliability of the process was demonstrate by means of a study on the influence of the contact deposition technique on the detection performance, in term of charge collection efficiency.

- Last part of thesis encloses the results reached in the preparation and characterization of four CZT detectors developed in range of "3D CZT High Resolution Detectors", project funded by European Space Agency (ESA). This project started from original idea of Doc. Carl Budtz-Jorgensen and Doc. Irfan Kuvvetli, from National Space Institute of Technical University of Denmark (DTU Space Center), that developed a novel type of CZT based detector: the drift stripes 3D detector. The aim of this project was to demonstrate that the good energy resolution of the CZT drift strips detector can be combined with 3D sensing capabilities, very important features for X and Gamma ray detectors for high energy astrophysics missions. IMEM institute was involved in some important parts of the project such as detector preparation, detector characterization and data analysis. The detector characterization was performed at European Synchrotron Radiation Facility (ESRF) in Grenoble. All these process were carried out by the author of this thesis in collaboration with Giacomo Benassi

Chapter 1

Basic radiation detection physics in CZT

1.1 Room-temperature compound semiconductor radiation detectors

Silicon (Si) and germanium (Ge) are traditional semiconductors used for radiation detectors that offer good performance in a wide range of applications. The growing field of applications has stimulated the development of detectors based on compound semiconductors. A great advantage of compound semiconductors is the possibility to grow materials with a wide range of physical properties (band gap, atomic number, density) making them suitable to almost any application. For many years the high energy radiation detection field was dominated by Si and Ge. These two materials are able to produce devices with a very high energy resolution and the corresponding read out electronic was already developed. However the use of these material requires a cooling down to cryogenic temperatures, usually at liquid nitrogen (77 K). The need of making a device able to work at room temperature has pushed the research in the direction of the exploitation of a new class of semiconductors characterized by a high and direct energy gap. Moreover, for X-ray and Gamma ray detection, compound semiconductors with high atomic number were preferred in order to emphasize photoelectric interaction, as will be further discuss. Compound semiconductors are generally derived from elements of groups III and V (e.g. GaAs) and groups II and VI (e.g. CdTe) of the periodic table. Besides binary compounds, ternary materials have been also produced, such as CdZnTe and CdMnTe. Among

semiconductors CdZnTe has emerged as a particularly suitable material in the realization of efficient X-ray and Gamma ray detectors. Due to the high atomic number, the high density and the wide band gap, CdZnTe detectors ensure high detection efficiency, good room temperature performance and are very attractive for X and Gamma ray applications.
Difficulties in producing detector-grade materials and in growing chemically pure and structurally perfect crystals are the critical issues of CdTe and CdZnTe detectors. In fact, the great potential of these compounds has not been exploited for many decades due mainly to the limited commercial availability of high-quality crystals. This situation has changed dramatically during the mid-nineties with the emergence of a few companies committed to the advancement and commercialization of these materials [1].

1.2 X and Gamma ray detection with semiconductors: principles of operation

The typical operation of semiconductor detectors is based on collection of the charges, photogenerated electrons and holes, through the application of an external electric field. The choice of the proper semiconductor material for a radiation detector is mainly influenced by the energy range of interest. Among the various interaction mechanisms of X-rays and Gamma rays with matter, three effects play an important role in radiation measurements:

- photoelectric absorption
- Compton scattering
- pair production

Photoelectric absorption is, in most cases, the ideal process for detector operation. All of the energy of an incident photon is transferred to one of the orbital electrons of the atoms within the detector material, usually to an electron of the K-shell. Otherwise when a photon interacting through Compton process transfers only a fraction of its energy to an outer electron, producing a hot electron and a degraded photon. In pair production a photon with energy above a threshold energy of 1.02 MeV interacts within the Coulomb field of the nucleus producing an electron and positron pair. Neglecting the escape of characteristic X-rays from the detector volume, fluorescent lines, only the photoelectric effect results in the total absorption of the incident energy and thus gives useful information about the photon energy. The interaction

cross sections are highly dependent on the atomic number. In photoelectric absorption it varies as Z^n with $4 < n < 5$, Z for Compton scattering and Z^2 for pair production. An optimum spectroscopic detector must favor photoelectric interactions and so semiconductor materials with a high atomic number are preferred. Fig. 1.1 left shows the linear attenuation

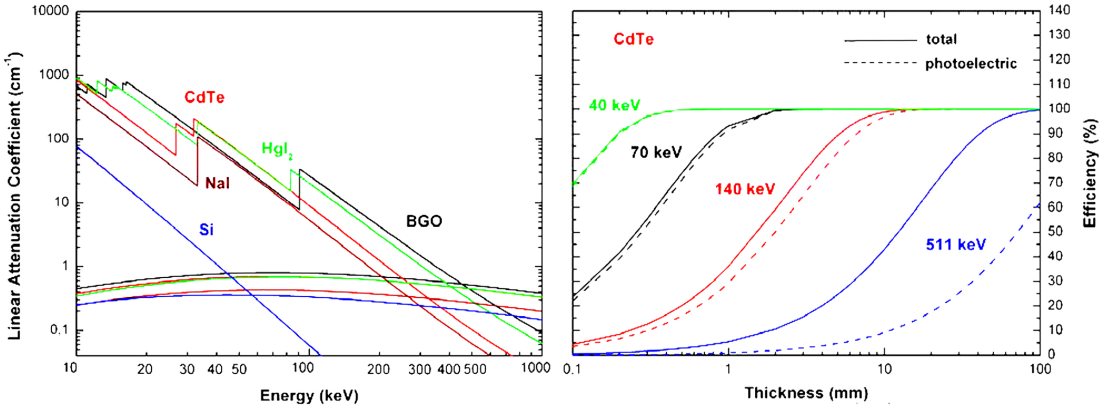

Figure 1.1: linear attenuation coefficients for photoelectric absorption and Compton scattering of CdTe, Si, HgI_2, NaI and BGO (left). Efficiency of CdTe detectors as function of detector thickness at various photon energies (right).

coefficients, calculated by using tabulated interaction cross section values[2], for photoelectric absorption and Compton scattering of Si, CdTe, HgI_2, NaI and BGO. NaI and BGO are solid scintillator materials typically used in radiation measurements. Photoelectric absorption is the main process up to about 200 keV for CdTe. The efficiency for CdTe detectors versus detector thickness and at various typical photon energies is reported in Fig. 1.1 right. For example 10 mm thick CdTe detector ensures good photoelectric efficiency at 140 keV (> 90), while a 1 mm thick CdTe detector is characterized by a photoelectric efficiency of 100% at 40 keV.

Semiconductor detectors for X-ray and Gamma ray spectroscopy behave like solid-state ionization chambers operated in pulse mode. The simplest configuration is a planar detector, a slab of a semiconductor material with metal electrodes on the opposite faces of the semiconductor (Fig. 1.2). Photon interactions produce electron-hole pairs in the semiconductor volume through the discussed interactions. The interaction is a two-step process where the electrons created in the photoelectric or Compton process lose their energy through electron-hole ionization. The most important feature of the photoelectric absorption is that the number of electron-hole pairs is proportional to the photon energy. If E is the incident photon energy, the number of electron-hole pairs N is equal to E/w, where w is the average pair creation energy. The generated charge

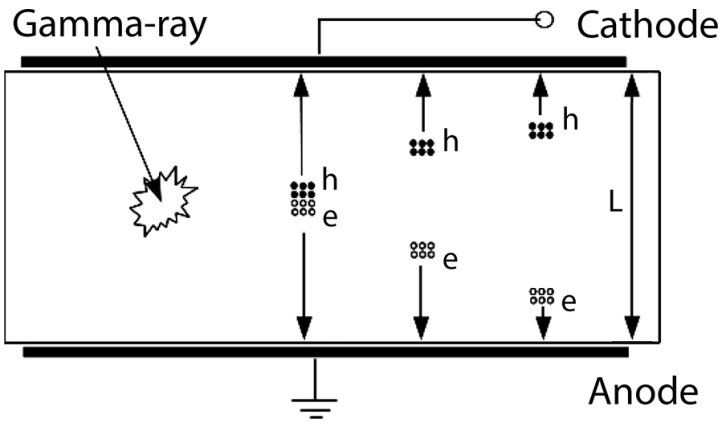

Figure 1.2: Planar configuration of a semiconductor detector. Electron-hole pairs, generated by radiation, are swept towards the appropriate electrode by the electric field.

cloud is $Q_0 = eE/w$. The electrons and holes move toward the opposite electrodes, anode and cathode for electrons and holes, respectively (Fig. 1.2). The movement of the electrons and holes, causes a variation ΔQ of induced charge on the electrodes. It is possible to calculate the induced charge ΔQ by the Shockley-Ramo theorem [3] which makes use of the concept of the weighting potential Φ, defined as the potential that would exist in the detector with the collecting electrode held at unit potential, while holding all other electrodes at zero potential. According to the Shockley-Ramo theorem, the induced charge by a carrier q, moving from x_i to x_f , is given by:

$$\Delta Q = -q[\Phi(x_f) - \Phi(x_i)] \tag{1.1}$$

where $\Phi(x)$ is the weighting potential at position x. It is possible to calculate the weighting potential by analytically solving the Laplace equation inside a detector [4]. In a semiconductor, the total induced charge is given by the sum of the induced charges due both to the electrons and holes. For a planar detector, the weighting potential Φ of the anode is a linear function of the distance x from the cathode: $\Phi(x) = x/L$ where L is the detector thickness and $0 \leq x/L \leq 1$. Neglecting charge loss during the transit time of the carriers, the charge induced on the anode electrode by N electron-hole pairs is given by:

$$\Delta Q = \Delta Q_h + \Delta Q_e = -\frac{Ne}{L}(0 - x) + \frac{Ne}{L}(L - x) = Ne = Q_0 \tag{1.2}$$

$$t > t_h = \frac{x}{\mu_h E} t > t_e = \frac{L - x}{\mu_e E} \tag{1.3}$$

where t_h and t_e are the transit times of holes and electrons, respectively.

Charge trapping and recombination are typical effects in compound semiconductors and may prevent the full charge collection. For a planar detector, having a uniform electric field, neglecting charge de-trapping, the charge collection efficiency CCE (the induced charge normalized to the generated total charge) is given by the Hecht equation [5]:

$$CCE = \frac{Q}{Q_0} = \left[\frac{\lambda_h}{L}\left(1 - e^{-\frac{x}{\lambda_h}}\right) + \frac{\lambda_e}{L}\left(1 - e^{-\frac{L-x}{\lambda_e}}\right)\right] \tag{1.4}$$

where $\lambda_h = \mu_h \tau_h E$ and $\lambda_e = \mu_e \tau_e E$ are the mean drift lengths of holes and electrons, respectively. CCE depends not only on λ_h and λ_e, but also on the incoming photon interaction position. The random distribution of the interaction point increases the fluctuations on the induced charge and thus produces peak broadening in the energy spectrum.

The charge transport properties of a semiconductor, expressed by the hole and electron mobility lifetime products, $\mu_h \tau_h$ and $\mu_e \tau_e$, are key parameters in the development of radiation detectors. Poor mobility lifetime products result in short λ and therefore small λ/L ratios, which limit the maximum thickness and energy range of the detectors. Compound semiconductors, generally, are characterized by poor charge transport properties due to charge trapping. Trapping centers are mainly caused by structural defects, impurities and irregularities, such as inclusions as will be discussed in next chapter. In compound semiconductors, the $\mu_e \tau_e$ is typically of the order of $(10^{-5} \div 10^{-2})$ cm^2/V while $\mu_h \tau_h$ is usually much worse with values around $(10^{-6} \div 10^{-4})$ cm^2/V. Therefore, the corresponding mean drift lengths of electrons and holes are $(0.2 \div 20)$ mm and $(0.02 \div 2)$ mm respectively, for typical applied electric fields of 2000 V/cm.

The energy resolution of a detector is the ability to resolve fine details of the incident radiation spectra. Consider now a mono energetic source of radiation that interacts via photoelectric absorption in the detector. The response of the device will be a distribution centered around an average pulse amplitude E. The energy resolution of the detector is connected to the full width half maximum ($FWHM$) of this distribution calculated removing an eventual background from the peak. The formal definition of energy resolution R is the ratio between $FWHM$ and the value of the position of the peak E.

$$R = \frac{FWHM}{E} \tag{1.5}$$

The distribution should have a Gaussian shape because the total number of charge carriers generated N is normally very high. The $FWHM$ of any Gaussian can be calculated through the relation $FWHM = 2.35\sigma$.

Charge collection efficiency is a crucial property of a radiation detector and affects the spectroscopic performance and in particular the energy resolution. High charge collection efficiency ensures good energy resolution which also depends by the statistics of the charge generation and by the noise of the readout electronics. Therefore, the energy resolution of a radiation detector is mainly influenced by three terms:

$$\Delta E = \sqrt{(2.355)^2 (F \cdot E \cdot w) + \Delta E_{el}^2 + \Delta E_{coll}^2} \tag{1.6}$$

The first term is the Fano noise due to the statistics of the charge carrier generation (again, E is the incident photon energy and w the average pair creation energy). In semiconductors, the Fano factor F is much smaller than unity $(0.06 \div 0.14)$ [6]. ΔE_{el} is the electronic noise, which is generally measured directly using a precision pulser, while ΔE_{coll} is the contribution of the charge collection process. Several semi-empirical relations have been proposed for the charge collection term of different detectors [7, 8].

1.3 CZT detectors

$Cd_{1-x}Zn_xTe$ is a more recent candidate for room temperature radiation detectors [9, 10]. The addition of a few percent of zinc to the melt results in an increased band gap as well as the energy of defect formation. CdTe and ZnTe form a solid solution throughout the entire alloy range, however only the range x = $(0.1 \div 0.2)$ is used for detector applications. The increased band gap (1.57 eV for x = 0.1) ensures high bulk resistivities and reduces the dislocation density, resulting in lower leakage currents and higher temperature operation. Specifically, resistivities of CdZnTe are typically between $(10^{10} \div 10^{11})\Omega cm$; one and two orders of magnitude greater than that of CdTe and thus leakage currents are correspondingly lower. This is very important in the detector development, because allows to obtain a lower leakage current or to apply a larger voltage bias. This ternary compound has a cubic, zincblende-type lattice with average atomic number $Z \approx 50$. The main drawback of CdZnTe crystals is the low value of $\mu\tau$ of the carriers and, especially the major difference between the $\mu\tau$ values of electrons and holes in respect to CdTe. However, the main advantage of CdZnTe over CdTe detectors is the absence of the polarization effect, that limits the exploitation of CdTe detectors. CdZnTe crystals are usually grown by using the high pressure Bridgman (HPB), low pressure Bridgman (LPB), vertical Bridgman and THM methods. The supply of spectrometer grade CdZnTe is nowadays limited to a small number of companies. Due to their low leakage currents (< 10 nA at room temperature), CdZnTe detectors are usually fabricated with ohmic contacts (Pt, Au) by using

metal-semiconductor-metal (MSM) structures. CdZnTe detectors with ohmic contacts (Pt) showed good energy resolution of 1.4% (FWHM) at 59.5 keV (T = -37 °C) [7]. Nevertheless, the poor hole charge transport properties produce long tails in the measured spectra. In order to overcome this problem single carrier devices (electron sensitive detectors), have been developed, such as drift strip method as it will be discussed in the last chapter.

In spite of the research efforts to improve the crystal growth technology, the yield of detector quality material remains low. This is because the growth of CdZnTe crystals presents some intrinsic difficulties:

- the superheating required for eliminating polymer in the melt above the melting point that makes seeding very difficult
- the low thermal conductivity of the solid
- the not-congruent evaporation of CdZnTe at the melting point
- the tendency of the matrix to incorporate tellurium inclusions
- the low value of the critical resolved shear stress that facilitates the formation of a large number of dislocations

In this frame, at IMEM institute, a new technique for the growth of CdZnTe crystals was developed [11]. That is known as boron oxide vertical Bridgman technique.
In parallel to the main activity on the tuning of grown technique to produce CZT crystals with the required performance, such as high resistivity, good charge collection efficiency and low tellurium inclusions density; several efforts have been also dedicated on the development of a reliable method to metalize the surface for the realization of efficient contacts and to control surface resistivity. They are still an open challenge in the detector preparation technology. Undersigned's phd work fits in this background as will be exposed in the following.

Chapter 2

The problem of inclusions in CZT crystals

In the current stage of development CZT crystals typically contain macro defects such as pipes, cracks, grain and twin boundaries as well as tellurium inclusions and precipitates. At the present time, CZT materials used for radiation detectors are grown under Te-rich conditions with deliberate introduction of n-type impurities such as Cl, In, and Al that ensure the high-resistivity required for radiation detection applications.
Solidification from Te rich melts results in the generation of two different kinds of crystal imperfections, inclusions and precipitate.

Precipitates are released due to the retrograde slope of the solidus line towards lower temperatures. Precipitates are formed via condensation of Cd vacancies; typical size of Te precipitates are $(0.01 \div 0.1)\mu$m. If the precipitation process goes nearly to completion, it means that more than 90% of the Te excess will be precipitated; the precipitated amount of Te is equal to the maximum solubility of Te in solid CdTe near the melting point.
Those precipitates dispersed in CZT appear to have only little effect on the electrical properties [12]. The same is not necessarily true for Te precipitates along grain and twin boundaries. With the relatively low bandgap (0.33 eV) of Te the electrical resistivity of the Te-rich precipitates will be several orders of magnitude lower than the surrounding CZT and might account for the higher leakage found along grain boundaries [13].

Inclusions are assumed to originate due to morphological instabilities at the growth interface. Te-rich Cd-Te melt will be captured from the diffusion layer in front of the interface.

Therefore, the appearance of inclusions mainly depends on the relation between growth rates and temperature gradients at the interface. Typical diameters of such inclusions are $(1 \div 3)\mu$m, but diameters up to $(10 \div 30)\mu$m have also been observed.
Unfortunately, inclusions severely limit the performances of CdZnTe-based detectors, particularly in the case of imaging devices [14]. Hence monitoring tellurium inclusion density is very important for assessing the material quality, for studying the formation mechanisms of inclusions during growth, and finally for checking the effectiveness of post-growth thermal treatments to reduce inclusion concentration.

In the following sections a novel technique to reveal Te-inclusions presence inside CdZnTe are presented. This technique allowed to study the effects of these defects on the performance of X and Gamma ray detectors based on this CdZnTe semiconductor. Results will be show in this chapter.
In the last section a new approaches for the reduction of these particles will be also presented.

2.1 3D mapping of tellurium inclusions in CZT crystals

Tellurium inclusion presence can be revealed by means of different techniques. One of them consists of the determination of equilibrium vapor pressure of samples at high temperature: if the tellurium phase is present, the total pressure is dominated by tellurium partial vapor pressure and the overall stoichiometry deviation can be determined [15, 16]. However, all information on dimensions and distributions of the inclusions is lost.
Inclusions can be revealed also by optical transmission in the near-infrared. Tellurium and cadmium inclusions are actually opaque in the infrared, in the transparent region of the material. A relation between the infrared extinction spectra and inclusion density was found [17], however, this technique suffers the same limitation as the latter.
Dimensions and distribution of the inclusions can rather be studied by infrared optical microscopy. The determination of concentration of inclusions is complicated by the fact that at high magnification depth of the field is much less than sample thickness, so that in a single photograph only a few inclusions appear really sharp. In order to overcome this problem, a set of photographs is taken at different focal planes, reconstructing all inclusions on a single focal plane [18]. This technique, known as “extended focus”, also provided with some commercial micro-scopes, suffers from two main problems: if one inclusion is present beneath a second one, only one is detected and, because the single focal plane, any information on the depth of each

inclusion in the sample is definitively lost. If the first limitation results in an incorrect counting of the overall inclusion density, the second one makes it impossible to reconstruct the distribution of inclusions in three dimensions. An ad hoc system for 3D reconstruction of inclusion distribution based on optical microscopy was recently proposed [19], but it requires the setup of a full optical bench and, according to the authors, can precisely determine the dimension only of inclusions larger than 3 μm.

The following section show in details the functioning of 3D reconstruction system assembled by the author of this thesis. Pictures are taken at different focal planes, images are then elaborated by a personally developed specific software, that ascribes each inclusion to the proper focal plane. As a result, all inclusions are counted and precisely localized in 3D. Using different objective lenses of the microscope it is possible to choose the optimal compromise between resolution and extent of the monitored area. Due to intrinsic diffraction limit of light at these wavelength it is possible to map inclusions down to 1 μm diameter. The system can be practically installed on any optical microscope that can operate in transmission mode.

2.1.1 System description

The most important part of the system is constituted by an optical microscope with the possibility to work in the transmission mode. The axial (vertical) movement is motorized so that the focusing is directly and automatically controlled by the software installed on a personal computer. Being the energy gap of CZT in the near infrared region, a silicon camera can be used to collect images. If the system is used to study a lower band gap material a different camera can be adopted (for example an InGaAs camera). Fig. 2.1 shows the scheme of the developed instrumentation. When using high magnification in the microscope many pictures must be taken at different positions on the vertical axis due to the low depth of focus with respect to sample thickness. A combination of all these pictures ensures a good 3D reconstruction of the sample. The PC moves the vertical axis, controls the camera, and acquires and elaborates the images.

The final spectral response of the described system is given by the product of emission spectra of the employed LED, the transmission spectra of the analyzed sample, and the quantum efficiency of the digital camera. Fig. 2.2 shows the spectral response in the case of a CdTe and a CZT sample. Of course, in the case of the former the total transmission is lower, due to lower energy gap of CdTe with respect to that of CdZnTe. Different objectives of the microscope can be alternatively used according to the performance required by the analysis. Table 2.1

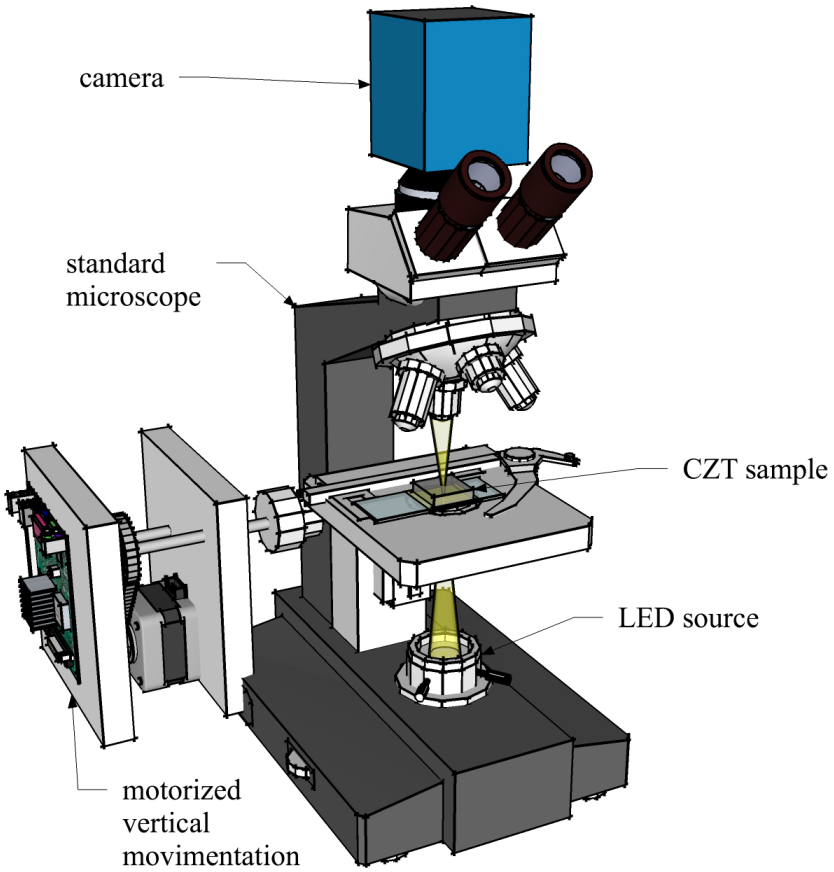

Figure 2.1: Scheme of Te 3D mapping inclusions instrumentation.

summarizes the characteristics of the objectives employed in the microscope present at IMEM institute, where the described instrumentation is currently in use. Once the objective has been chosen, the total area of the sample investigated by the camera is fixed; of course the larger the area, the smaller the magnification. Moreover, each objective has a numerical aperture NA, which depends on the construction parameter. On the basis of the numerical aperture it is possible to calculate the depth of field using the Eq. 2.1 [20],

$$P = \frac{n\lambda}{2 \cdot NA^2} \tag{2.1}$$

where n is the index of refraction of the sample and λ the wavelength of the radiation. As previously mentioned the microscope uses a near-infrared high power LED, and, as shown in Fig. 2.2, the transmission of the system is peaked at a wavelength that is conveniently used to calculate depth of the field by Eq. 2.1. In order to entirely map the sample, without skipping portions of material, it is necessary to take pictures at a vertical distance lower than

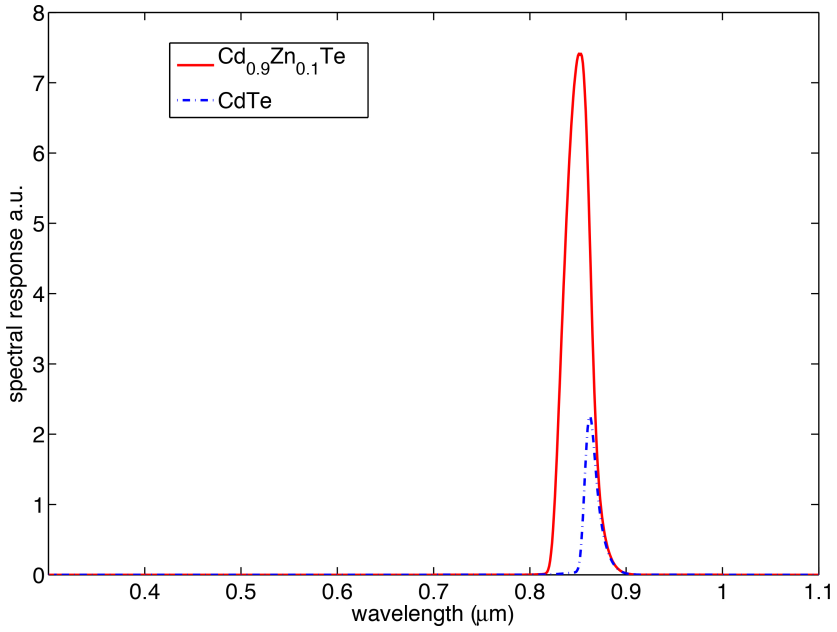

Figure 2.2: Spectral response of the system in the case of a CdZnTe (red plain curve) and a CdTe (blue dash-dotted curve) 2 mm-thick sample.

the depth of field P of the considered objective (at least equal). The depth of field of the objective also represents the vertical resolution of the system. For each objective, it is also possible to find out the area of the sample scanned by each pixel of the camera. This parameter was determined, for the described system, for each objective (Table 2.1) and it's related to the horizontal resolution of the system. Another important parameter to be determined is the maximum sample thickness that can be scanned. This is defined by the maximum distance to which the objective can focus before the objective itself comes in contact with the upper surface of the sample. This parameter depends on the focal length of the objective and, for a given objective, on the index of refraction of the sample. In fact, it can be demonstrated [20] that moving the sample with respect to the objective of a quantity Z' results in an effective movement of the focal plane inside a medium of index of refraction n of the quantity

$$Z = Z'n \tag{2.2}$$

In Table 2.1 the maximum scanning distances D of each objective are also reported. After acquisition, the PC processes the pictures in order to reconstruct the 3D image: this can be done with the aid of the methods described in the deposited patent [21].

Magnification	Area (μm^2)	NA	P^a (μm)	pixel/Area (μm^{-2})	D (mm)
5x	1280 x 1024	0.1	124	1	27
10x	640 x 512	0.25	20	4	9
20x	320 x 256	0.4	8	16	7.5
40x	160 x 128	0.65	3	64	2.5

Table 2.1: Properties of the objectives used. ^{a}For CdZnTe with Zn = 10%

2.1.2 Results and discussions

The system was tested with CdZnTe (Zn 10%) samples routinely grown at IMEM laboratory for the preparation of X-ray detectors [11, 22]. The crystals are grown from tellurium rich melt; thus Te inclusions are typically present [23]. Assuming inclusions to have spherical geometry,

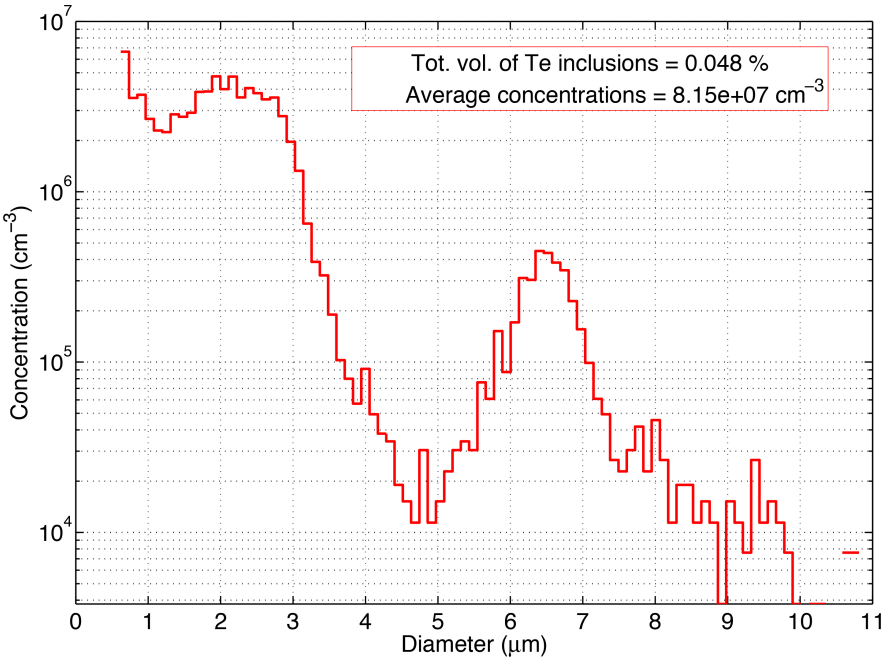

Figure 2.3: Inclusion concentration as a function of inclusion diameter.

the total Te excess N_{Te} per cm^3 represented by them can be calculated as

$$N_{Te} = \frac{4\pi\rho_{Te}N_A}{3A_{Te}} \sum_{i=1}^{n} r_i^3 \rho_i \tag{2.3}$$

with r_i the radius and ρ_i the density of the inclusions, A_{Te} the relative atom mass of Te and ρ_{Te} the mass density of Te. The index i stands for each class of particle diameter. Fig. 2.3 shows

the inclusion distribution in a 2 mm thick sample. The measurement was carried out using an objective with a 20x magnification. At this magnification, the resolving power is around 1 μm. According to Table 2.1, 1 μm^2 corresponds to 16 pixels, so that the inclusion can be certainly identified. Fig. 2.3 shows the first result of the data processing, which illustrates the number of inclusions as a function of inclusion diameter. Keeping in mind the extent of the examined volume it can be realized that a concentration of about $7 \cdot 10^3$ cm^{-3} corresponds to the identification of only 1 inclusion. Of course, this limit can be lowered by acquiring more data. This can also be done automatically by moving the sample on the horizontal plane. Another important parameter that can be obtained is the total volume occupied by the inclusions: this is directly related to off-stoichiometry, (which can be obtained by other destructive techniques [15, 16, 17]). It should be pointed out that histograms like the one shown in Fig. 2.3 can also be obtained by other techniques like the "extended focus", but the latter technique cannot distinguish inclusions in the same vertical position at different planes, and thus tends to underestimate the inclusion concentration, especially in thicker sample. Moreover, the method described in this thesis also provides the distribution of inclusions in 3D. In Fig. 2.4 all

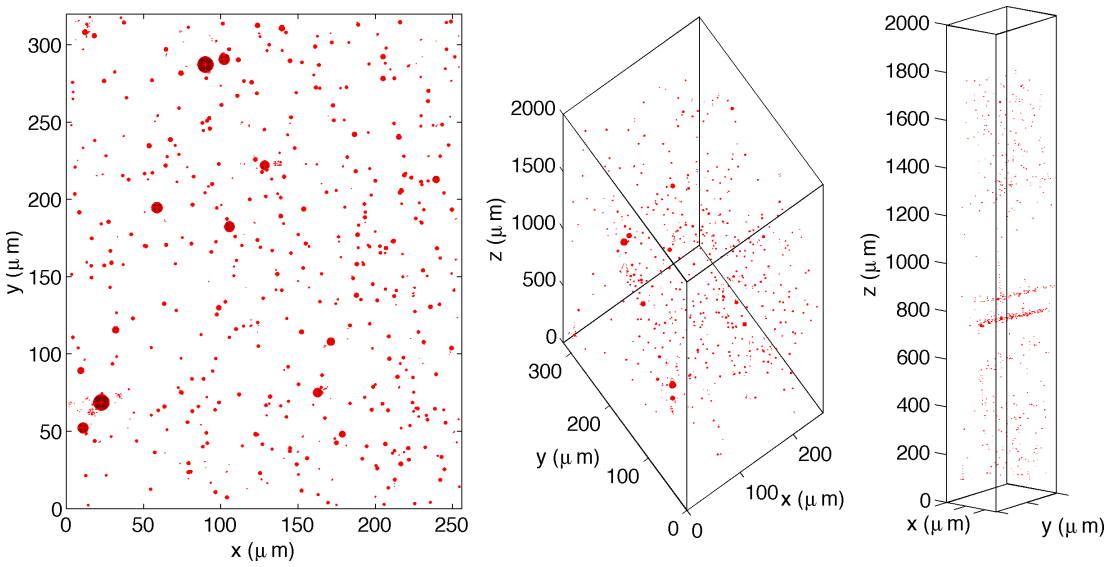

Figure 2.4: general 3D representation of the inclusion distribution (left), top view of the inclusion distribution (center) and representation of the inclusion distribution along a particular direction (right).

the inclusions are shown as red sphere, with its proper diameter. Actually Fig. 2.4(left) presents the top view of the sample, which corresponds to the typical view that can be obtained by means of the "extended focus" technique. It is possible to see that an almost uniform distribution of

inclusions goes by with some inclusion clusters. No information is obtained on the distribution of inclusions in the third dimension. Fig. 2.4(center) shows a general 3D representation of the inclusions in our sample. If we consider a proper section of the sample Fig. 2.4(right) we can see that the inclusions are actually mainly distributed along particular planes, two of which are almost parallel to the surface of the sample close to its center; a third one is located in the lower half of the sample at an angle of about 60°with respect to the lower surface. The first two planes are actually perpendicular to the growth direction. We can make the hypothesis that the inclusions along these planes are the consequence of some fluctuations at the interface during crystal growth. Of course these features are not revealed in the top view (Fig. 2.4a). Our observations are in accordance with those previously observed by other authors: tellurium inclusions in some regions appear homogeneously distributed in the matrix, but sometimes decorate grain boundaries or sub-grain boundaries [24, 19].

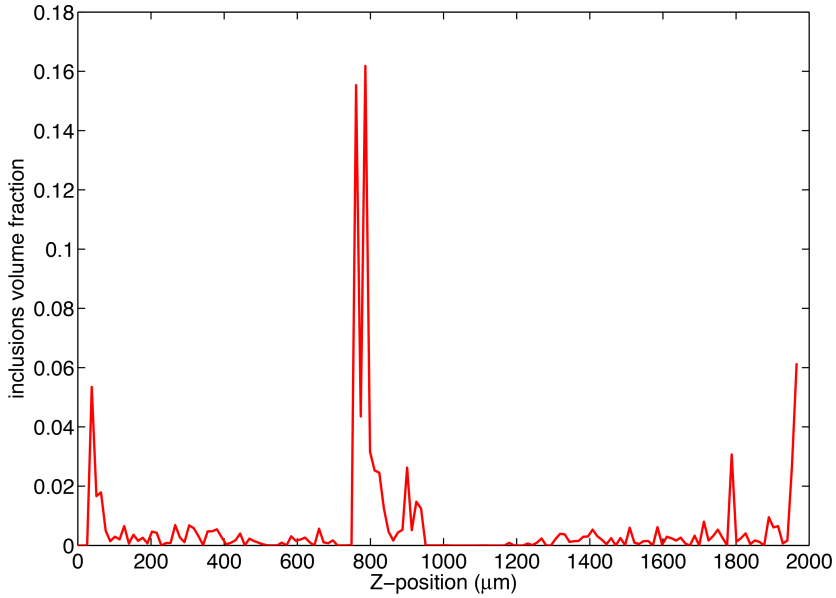

Figure 2.5: Inclusion concentration along the vertical axis.

Another possible way to visualize the inclusion distribution is to plot inclusion density along a particular directions. Fig. 2.5 for example shows inclusion density along the vertical direction. A high concentration of inclusions close to the sample center is clearly visible.

2.1.3 Conclusions

In this section was described a setup for the determination of the inclusion distribution in 3D. The proposed method can be implemented on standard transmission optical microscopes. Inclusions down to 1 μm can be detected and evaluated. The vertical resolution of the system is controlled by the numerical aperture of the employed objective and can be decreased to 9 μm. Thanks to a proper collection of images and use of ad hoc software in image reconstruction, it is possible to obtain a fully 3D reconstruction of the inclusion distribution, so that the position and the dimension are identified for each inclusion. Using this system, it is possible to study in much better detail important features of the inclusion distribution that can be directly correlated with the growth parameters and possible exploitation of the material for the preparation of X-ray detectors.

2.2 Tellurium inclusions and charge collection in CZT X and Gamma ray detectors

Despite its many attractive characteristics CZT crystals contain several types of defects, which play a role in degrading the charge-carrier transport. Some such defects, like Te inclusions, are related to the growth of CZT crystals from a tellurium-rich melt as above mentioned. Others, like dislocations and sub-grain boundaries, result from difficulties in controlling the optimal growth conditions, and from the low thermal-conductivity of CZT.

Identifying defects in CZT material requires several experimental techniques such as IR transmission microscopy and X-ray response map. By correlating non-uniformities in the detector's responses with particular defects and their spatial distributions, it's possible to gain an understanding of phenomenological influences on the devices' performances.

At the IMEM Institute in Parma, detector-grade CZT material was grown via the modified low-pressure vertical Bridgman method [25, 26, 27]; the resulting material showed high resistivity and good carrier-transport properties that are well suited to detecting X and Gamma rays. In the following section the influence of Te inclusions in these IMEM-grown CZT crystals will be discussed using two experimental techniques, the previous described IR mapping of Te inclusions and X-ray beams at the National Synchrotron Light Source at Brookhaven National Laboratory.

2.2.1 Experimental

At IMEM institute eight CZT ingots were grow by the low-pressure Bridgman technique [25]. The CZT polycrystalline charges were synthesized directly from 7N-purity level elements. After growth, the charge was heated in a high-purity inert gas to improve the stoichiometry of CZT [26]. Growing parameters were optimized for growing the crystals inside a boron-oxide ampoule via the vertical Bridgman method [27]. The thermal gradient at the growth interface was ∼10 °C/cm, and the growth rate was ∼1 mm/h. The ingots were cooled at ∼30 °C/h. Material was doped with indium to induce high electrical resistivity. Over 20 samples, 7 x 7 x 2 mm^3 , were prepared from different locations of the as-grown ingots. Samples' surfaces were polished with diamond paste down to 0.1 μm to remove the damaged layer caused while cutting them. Then, gold contacts were deposited on both surfaces using an aqueous $AuCl_3$ solution [28]. Bulk resistivity was evaluated from fitting the low-voltage region $(-1 \div +1)$V of the I-V curve [29] resulting in the range $(1 \div 4.5) \cdot 10^{10} \Omega$ cm. Spectral responses were measured using standard radiation sources. The mobility-lifetime product ($\mu\tau$) for electrons was analyzed using both an alpha particle source and an X-ray source. Results were in good agreement and the value obtained is $2 \cdot 10^{-3}$ cm^2/V. Size distributions and concentration of the Te inclusions were measured using the previously described IR transmission microscopy system, which gave an accurate measurement of the distribution of Te inclusions in three dimensions. In addition, extended focus image was generated.

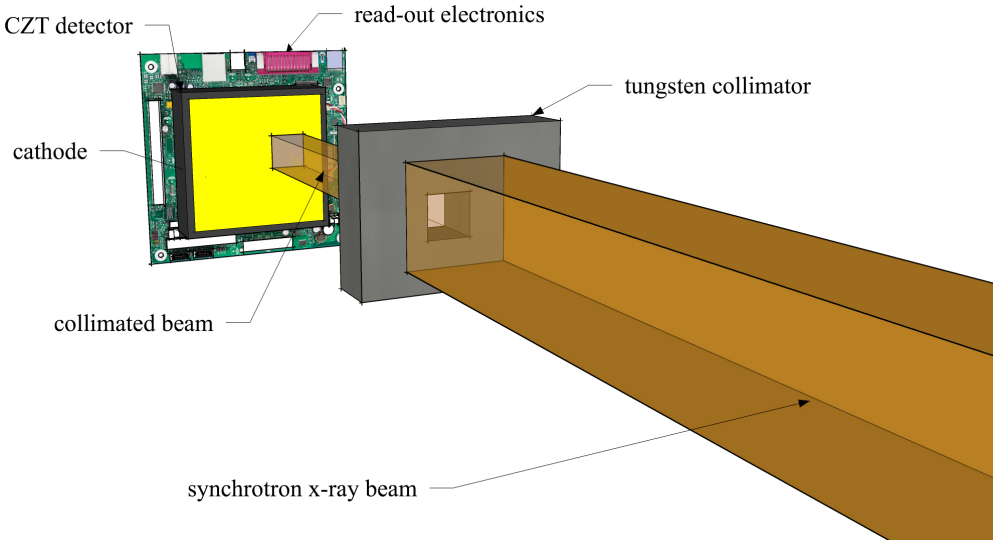

Figure 2.6: Scheme of X-ray mapping experiment.

X-ray microscale mapping is a characterization technique that can provide useful information on the homogeneity of the X-ray response map in the x-y plane. Measurements were performed at the Brookhaven National Laboratory using a 24 keV beam line at the NSLS facility [30]. The mono energetic 24-keV collimated beam ($20 \times 20\mu m^2$ by the use of a tungsten collimator) impinging on the cathode surface of the sample, as described in Fig. 2.6, generated an X-ray spectrum at each beam's position. Gravity center of peaks were determined from these spectra and plotted as two-dimensional maps. Such maps, acquired in 20μm steps, represent the spatial variations of the device's charge collection efficiency.

Using these data was possible to correlate the volumetric distributions of Te inclusions with the non-uniformities of the X-ray response maps measured with the collimated synchrotron X-ray beam.

2.2.2 Results and discussions

IR measurements show the presence of Te inclusions with a concentration of about $6 \cdot 10^5$ cm^{-3}. The size varies between $(2 \div 30)\mu$m. A characteristic IR transmission image of IMEM samples is shown in Fig. 2.7. Dark spots are Te inclusions; also some residual scratches from

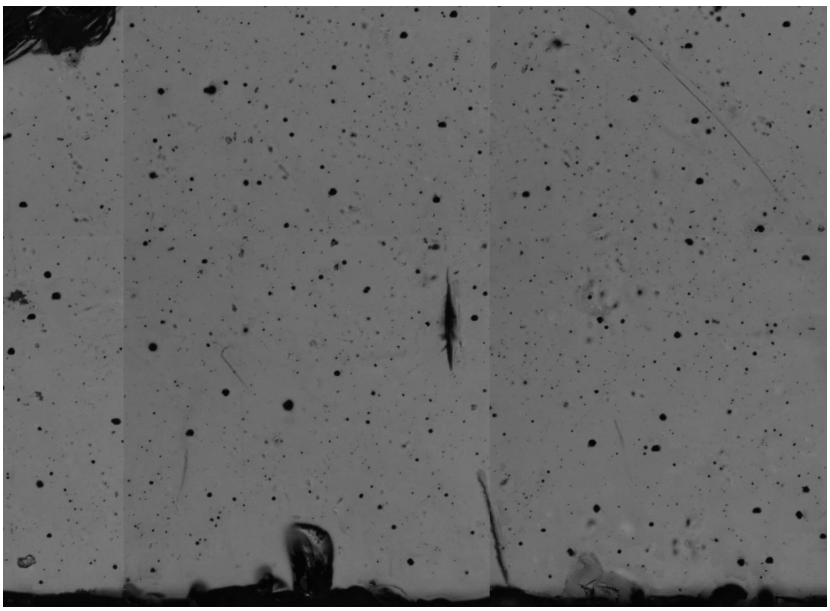

Figure 2.7: An IR multi-focus image of IMEM samples, the dark dots are Te inclusions, their size is $(10 \div 100)\mu$m. Some surface features (scratches) are also present.

the polishing procedures are clearly visible. About the X-ray microscale mapping, it can seen

from Fig. 2.8 that it showed very good response (the copper color of the image is arbitrary). The detectors response is very uniform and the fluctuation in the X-ray response are less then 2%. The brighter parts in the map are areas with a good response, while the darker spots are connected with e degradation of the X-ray response. The map appears very bright, meaning

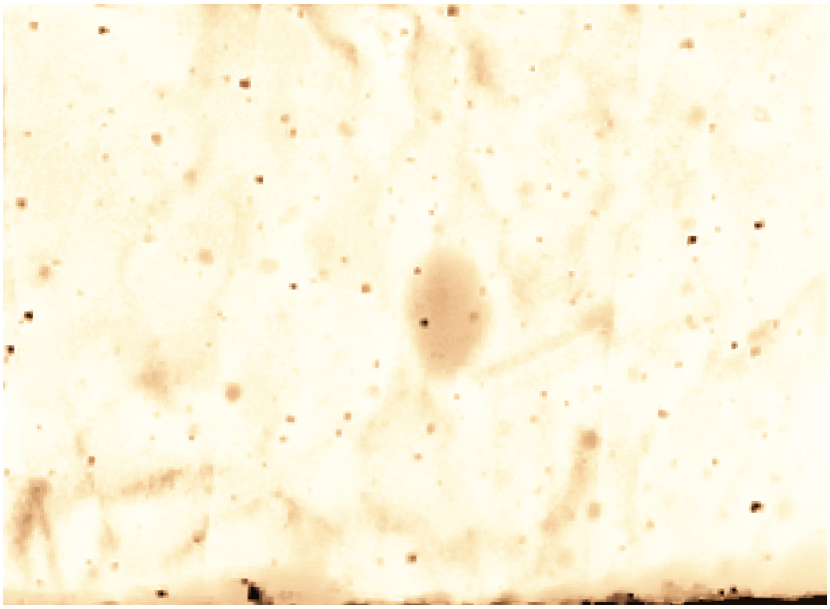

Figure 2.8: X-ray response map of a IMEM sample. Raster scan resolution is 20 μm, beam energy is 25 keV.

that the detector has good charge collection efficiency, but some darker spots are also present.

The results of these two techniques were compared to each other. First of all the IR collapsed (extended-focus) image was compared with the X-ray response map. Contrast of X-ray response map was enhanced in order to highlight the presence of features in the response (Fig. 2.9). These two images show several similarities; in fact in the X-ray response map many dark dots are present. The dark dots are associated with the presence of Te inclusions and the comparison with the IR collapsed image confirms that. The features present in the X-ray map correspond to Te inclusions in the IR image. Some of the Te inclusions are identified and marked with circular dots in Fig. 2.9, the selected inclusions are selected randomly all over the sample. The size of the Te inclusions that are visible in the X-ray response map vary between $[8 \div 30]\mu$m. Smaller inclusions, that are visible in the IR image, cannot be seen in the X-ray response map. This is due to the raster scan resolution used for the X-ray response map. All the big inclusions (30 μm) can be identified in the IR map. In order to understand the correlation within the effect of Te inclusions on the X-ray response map and the positions of the same in the sample,

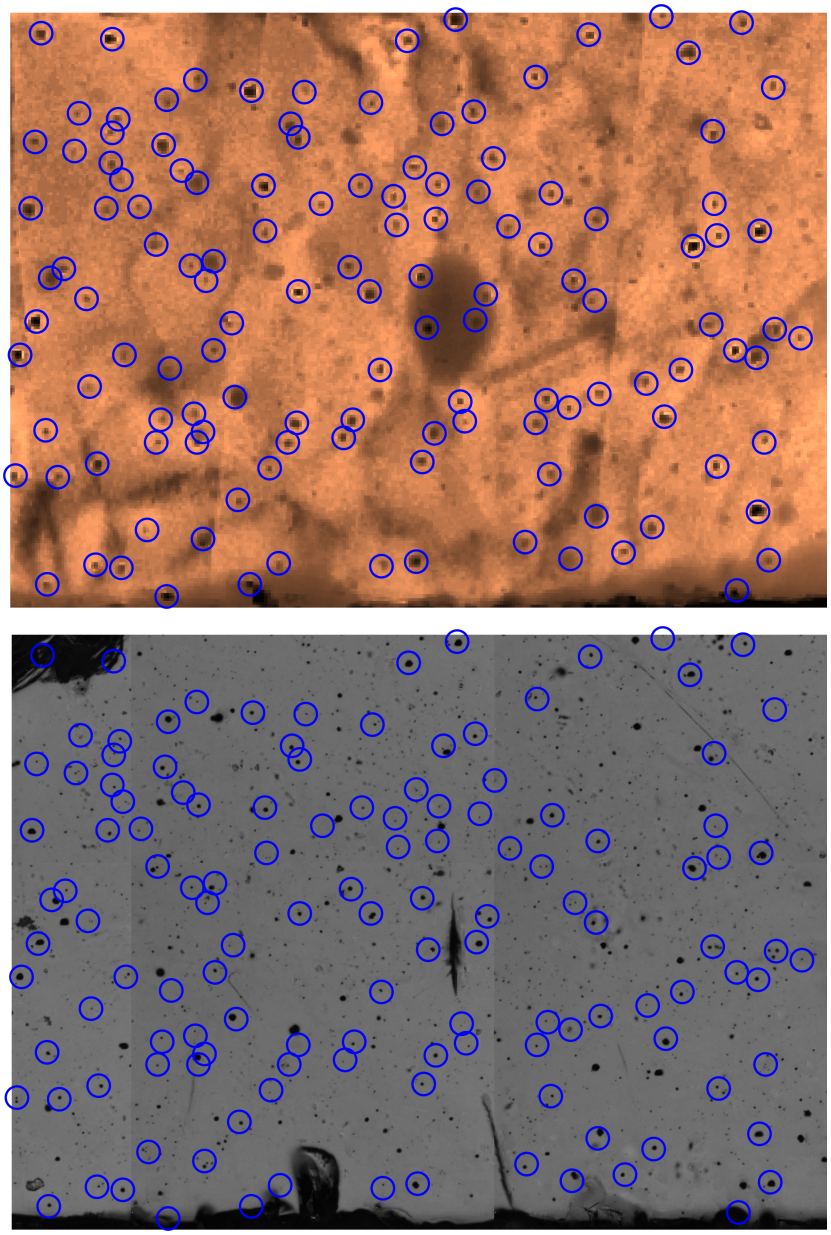

Figure 2.9: Correlation between the X-ray response map and the IR collapsed image, Te inclusions can be identified in both maps.

the IR collapsed image was split into images with different focal planes.

X-ray response map was so compared with a bottom IR image; the bottom part of the sample is the part close to the anode, close to the read-out electronics. Fig. 2.10 shows that the inclusions previously identified in the collapsed image do not belong to this region of the sample. In fact only a small number of big Te inclusions can be identified.

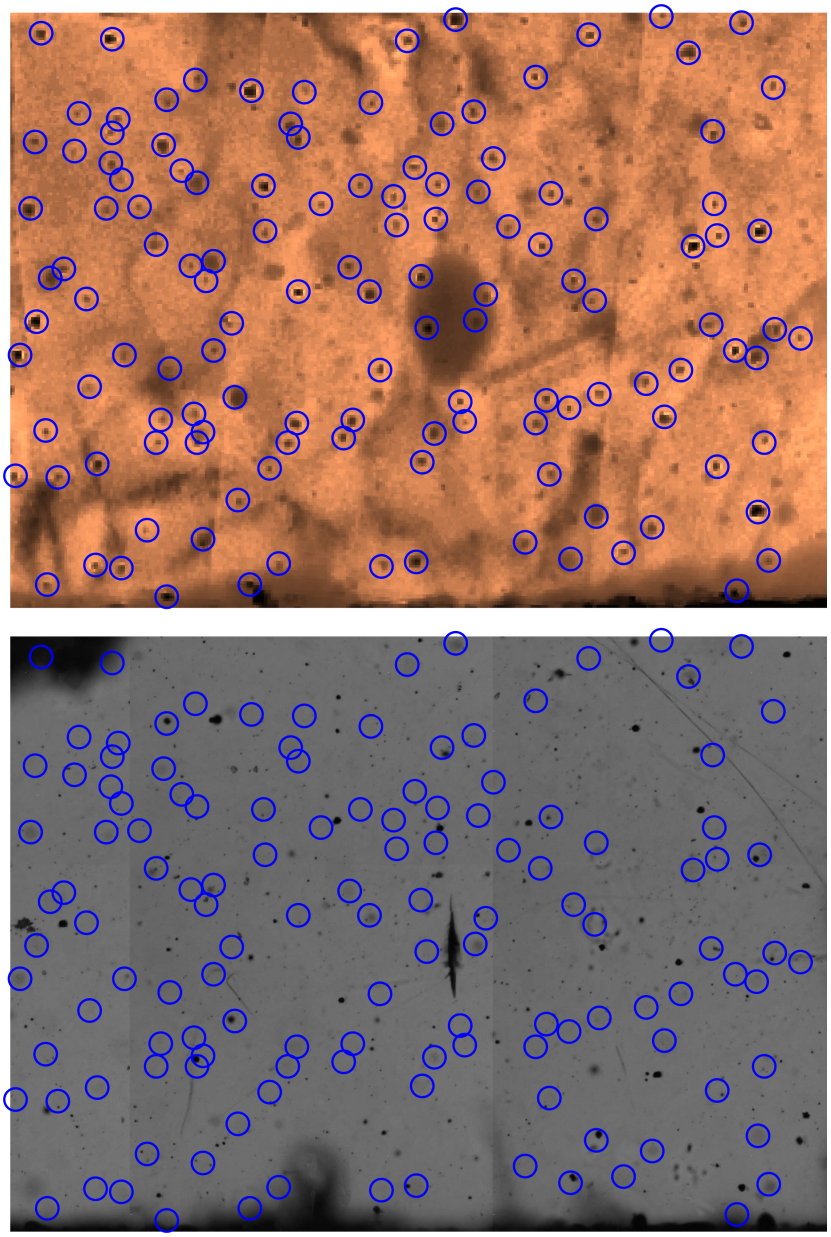

Figure 2.10: Correlation between the X-ray response map and the IR bottom image, only a few inclusions belong to this region of the sample.

The X-ray response map is then compared to a top IR image, an image taken close to the cathode part, close to the interaction area of the photons from the synchrotron. A comparison between the two images, in Fig. 2.11, shows that the majority of the Te inclusions are in this region of the sample. In fact this is the area where the charge carriers are generated, and the influence on the collection is higher. It must be noted that in this region also small Te inclusions

can be detected.

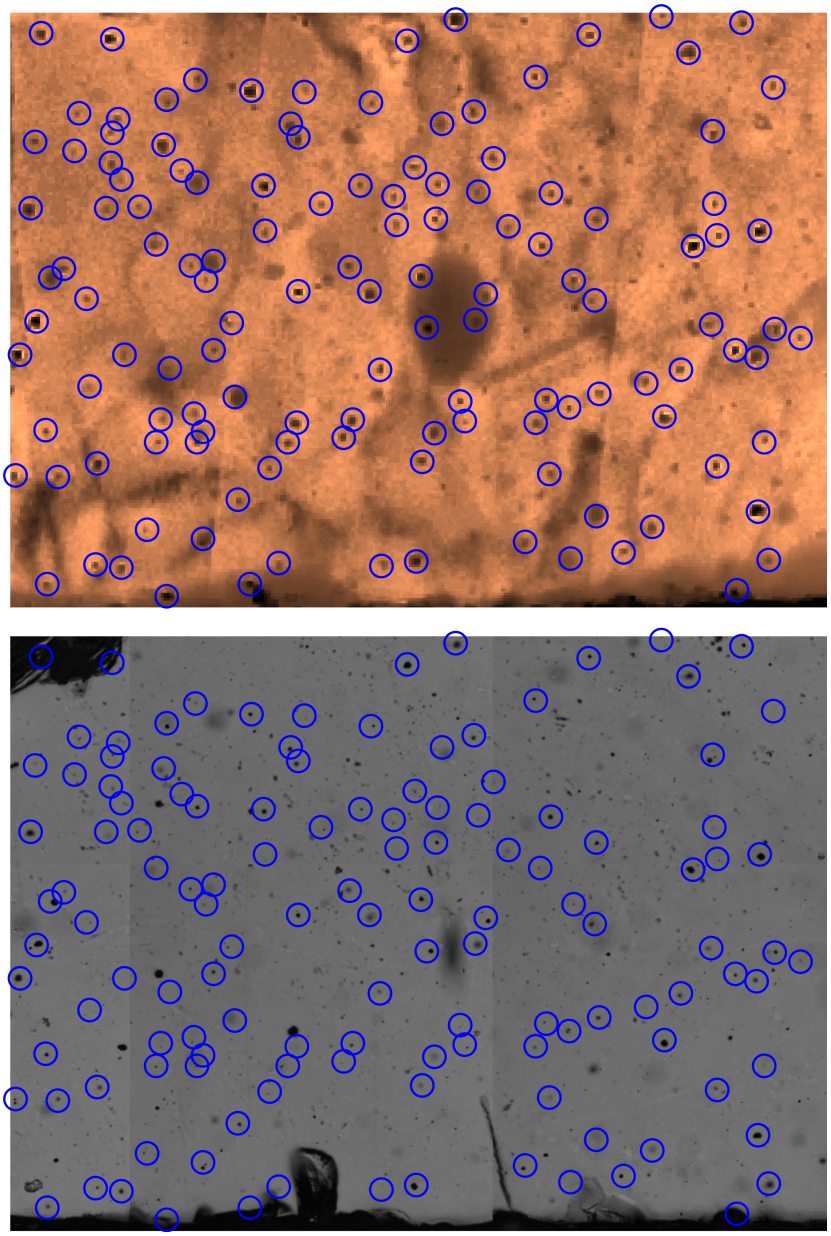

Figure 2.11: Correlation between the X-ray response map and the IR top image. Many identified inclusions belong to this region.

2.2.3 Conclusion

A set of IMEM grown CZT samples was studied in collaboration with the Brookhaven National Laboratory. Several high resolution techniques were used, leading to complementary results

in the characterization of the well known defects affecting the material. Te inclusions were identified using IR microscopy. The entire thickness of the sample was scanned and a collapsed image, containing information on all the sample depth, was acquired on the entire area of the sample. X-ray response map were performed using a 24 keV synchrotron X-ray beam and a raster scan resolution down to 20 μm, on a large number of samples. The response map showed high uniformity of the response, with a fluctuation of about 2% in the device charge collection efficiency. The degradation of the detector response was correlated with the presence of Te inclusions in the IR images. A correlation was found between the spatial position of the inclusions in the detector thickness and the local effect on charge collection, as expected by theoretical models proposed in the literature [31]. In that models Te inclusions can be considered as extended local defects with a very high local concentration of trapping centers. In this case, an unpredictable amount of charges will be trapped and the fluctuations in the charge loss become proportional to the total number of such defects encountered by the electron cloud. Moreover, any distortions of the electric-field around that defects can also contribute to dispersion of the collected charges (and to degradation in the spectroscopic performance). From the results of this studies, we see that defects close to the cathode widely affect the local Gamma response when the 24 keV beam was used. At this energy, and for CZT material, the penetration of the photons is about 100 μm; it suggest that if we consider more energetic photons, defects positioned deeper in the crystal became more important. In conclusion, Te precipitates located in the IR images fully correlate with the deterioration of the X and Gamma ray spectroscopic response of detectors by producing degraded localized zones within the devices.

2.3 Luminescence properties of CZT crystals around tellurium inclusions

Once achieved important informations about phenomenological effects of the presence of Te inclusions on detectors performances, the study was directed on the investigation of defects' nature. Nature of these defects, in the performance decreasing of the device, has been studied also in other works [31, 32, 33]. In the latter the deteriorating effect associated with inclusions is mainly ascribed to the effective trapping of carriers at the inclusion sites. Moreover, it is also well-known that tellurium inclusions are typically surrounded by dislocations [34, 35].

Particular attention should be paid to the study of deep levels in the energy gap of the semiconductor and their possible correlation with common features and structural defects that

are present in the material. It is well known the effect of deep levels on carrier lifetime and hence the problems induced by their presence in radiation detector materials.
More recently, the region that surrounds tellurium inclusions has been investigated by photoluminescence (PL) mapping [36]. The authors observed a blue shift of the donor-bound-exciton peak that is attributed to the presence of a strain field. However analyzed energy range of the emitted light was limited to $(1.3 \div 1.7)$eV.

For these reasons photoluminescence mapping were performed in the region surrounding tellurium inclusions in order to study possible intensity changes of the intra-gap energy level emission of CdZnTe due to the presence of inclusions.

2.3.1 Experimental

As in the previous analysis, CZT samples studied were grown at IMEM institute using the Vertical Bridgman furnace. Samples were prepared by cutting ingots into wafers perpendicularly with respect to the growth axis and, then, selecting single crystal regions inside the wafer. The selected samples were cut with standard dimensions of 5 x 5 mm with thickness ranging from 1 to 2 mm. Sample surfaces were polished with diamond pastes with a mesh down to 0.1 μm.

The as-polished samples were finally placed on the IR microscope stage in order to create a map of inclusions within the entire volume with the technique described above. We focused our attention onto large inclusions (20 μm or more), being the choice of a large inclusion preferred because the influence on surrounding lattice properties was expected to be stronger and hence more easily studied with PL. Exact position of inclusions was identified by the 3D IR reconstruction (Fig. 2.12). Inclusions with dimensions larger than 20 μm were rarely observed in these samples. However, once a large inclusion was identified, the optimal location of the inclusion for the PL study could be obtained by chemically etching the surface. Standard etching solution based on Br-methanol was used [37, 38]. At the end of etching procedure, the chosen inclusions were not visible using the reflection mode of an optical microscope with visible light, however they were clearly identified by switching the system in transmission mode in the near IR. For example, in the case of the inclusion shown in Fig. 2.13, both the inclusion and the small scratch induced near it on the sample surface appear in focus in the IR picture even at the higher possible magnification allowed by our microscope (800 x). At this magnification, the depth of field is about 4 μm. Thus, we estimated that the inclusion must be less than 4 microns beneath the sample surface. This value is actually lower than the minority carrier diffusion length in low conductivity CdZnTe crystals that was reported to vary between $(6 \div 15)\mu$m [39].

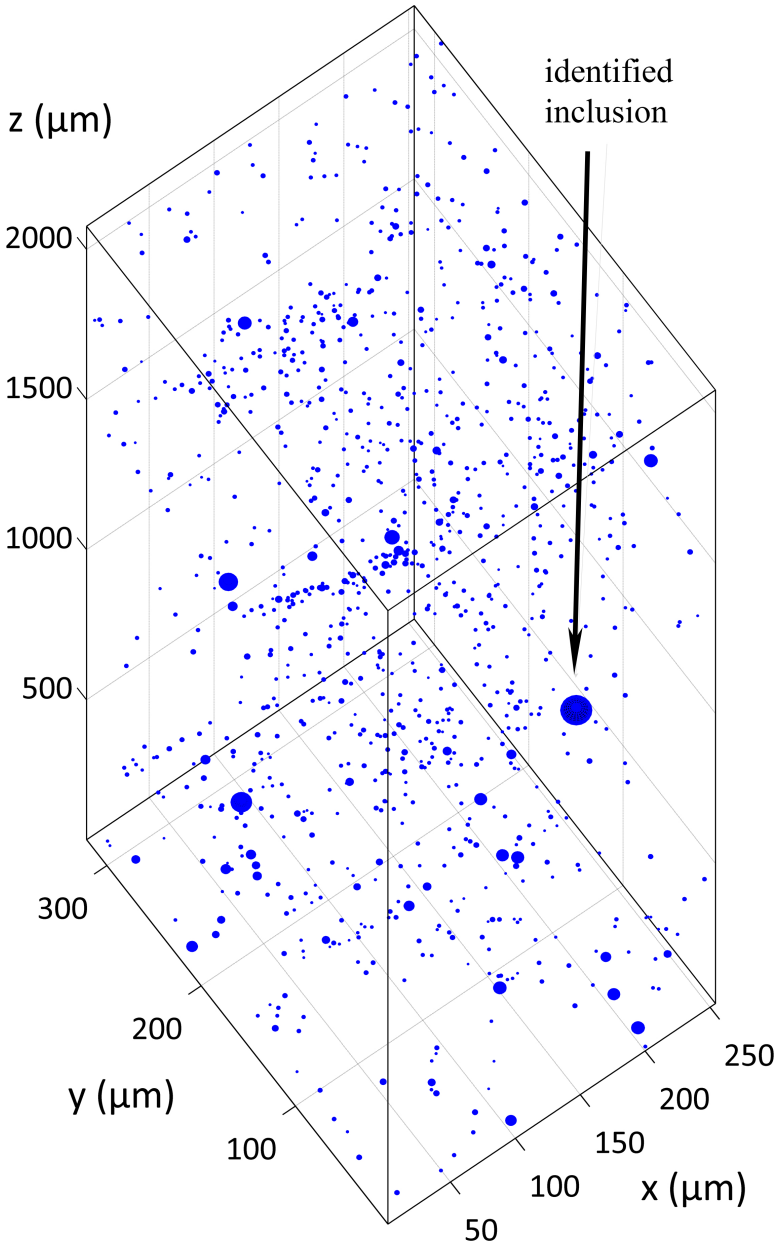

Figure 2.12: 3D inclusions distribution in a CZT sample. The inclusions size is ranging between 1 and 30 μm. Largest identified inclusion is highlighted by the arrow.

So, a PL mapping experiment on that surface analyzed a portion of the CdZnTe matrix that was close to the large tellurium inclusion.

Photoluminescence mapping was carried out at 77 K. PL spectra were detected using the Bruker IFS66 Fourier spectrometer equipped with both Si and InGaAs detectors. The instrument is equipped with an automatic x-y movement for the acquisition of micron-scale maps.

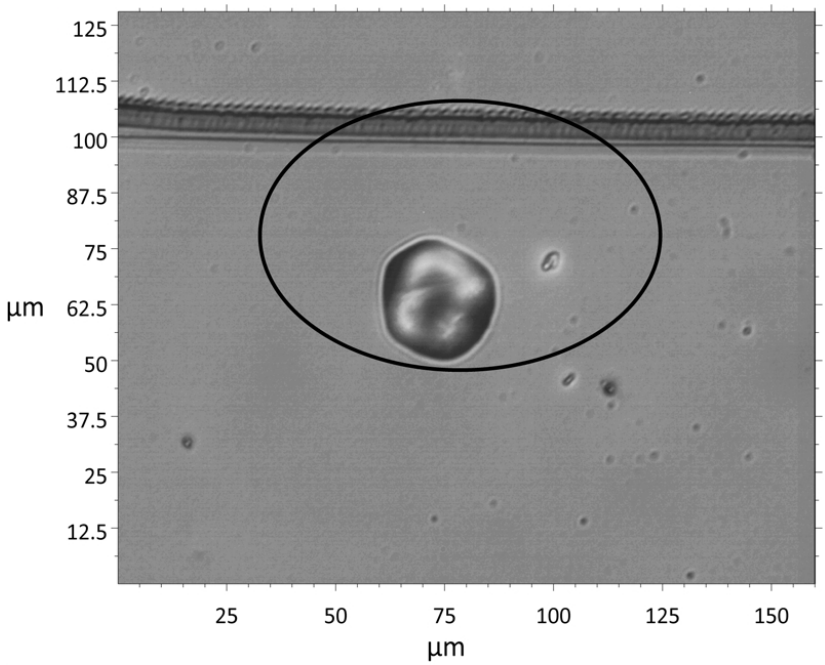

Figure 2.13: IR image of the near surface region of the sample, the large feature at the center of the photograph is a 27 μm Te inclusion. In the upper part of the image the identification scratch is visible.

The spatial resolution of the system is estimated to be 10 μm. The measurement is controlled by Bruker commercial software for elaboration of obtained raster scans. By raster scanning the sample, it was possible to obtain a full emission spectrum for every point interrogated. By data processing, the desired information was extracted, such as the band-edge emission energy or the integrated intensity under a certain PL emission. In this way, it was possible to obtain several maps and extract different information starting from a single set of spectra. In order to correctly superimpose the IR picture and the PL maps, a gold grid was deposited on the samples. This ensures an alignment of IR pictures and PL maps with an error of about 1 μm.

2.3.2 Results and discussions

First of all, PL spectra were recorded at 77 K in a region far from any tellurium inclusions.

Two different types of PL spectra were recorded. The first type is shown in Fig. 2.14 and is characterized by four main contributions. The peak at higher energy (1.64 eV) is due to near band-gap recombination. The broad band emission centered around 1.4 eV is commonly related to a complex formed by a cadmium vacancy and indium in the cadmium site, the so-called A-center [40]. The band centered at 1.07 eV was attributed to Te-vacancies [41] or a Fe-related

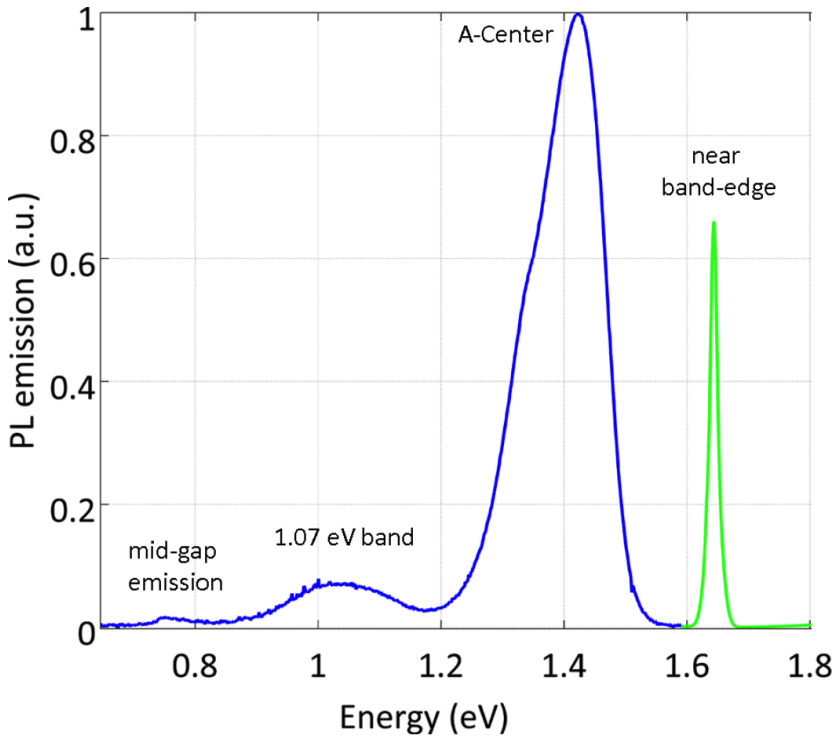

Figure 2.14: 77 K PL spectrum of a CZT sample acquired in a region far from the inclusion. Tree main emission band are clearly visible: the 1.4 eV A-center emission, the 1.07 eV band and the mid-gap emission centered about 0.78 eV.

complex [42, 43]. These bands are features commonly observed in PL emission spectra and widely studied in literature. The fourth one at 0.78 eV is instead not always reported and was sometimes related to Te-antisites (Te_{Cd}) [44]. The intensity of this peak was much lower than the intensity of 1.4 eV peak, however still much larger than detector noise. More recently, an emission band at 0.82 eV has been observed in CdZnTe crystals as a consequence of surface damaging by the scribing process [45]. Due to this reason, it has been ascribed to the presence of dislocations originated by the scribing process. The second type of recorded spectra is similar to the one obtained in Fig. 2.14, except for the absence of the mid-gap emission band. The cause of the two different behaviors is still under investigation, however we suggest it could be related to small variations of Fermi energy position. In fact, in case of high resistivity detector material, the Fermi level is close to mid gap, so that the occupation state of mid gap levels (and the intensity of the related emission) can drastically change as a consequence of small variation of Fermi energy position.

In Fig. 2.15 the PL maps are shown correspond to the portion of the sample reported in Fig.

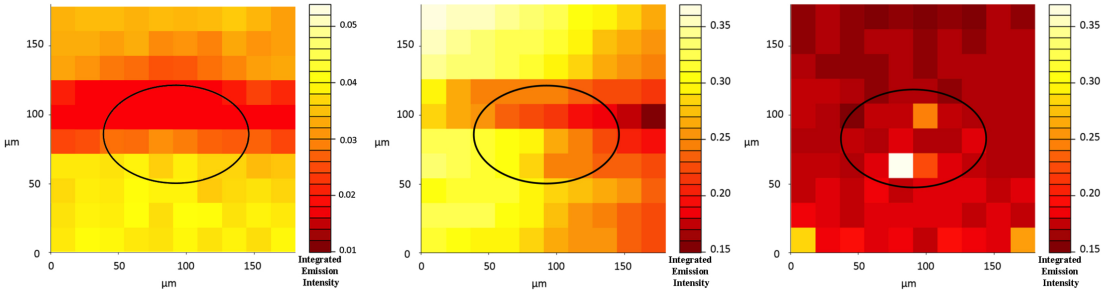

Figure 2.15: 77 K PL maps reporting the integrated intensity of the near band-gap emission peak (left), A-center emission peak (center), and mid-gap emission peak (right). The black oval highlights the same region of the sample as in Fig. 2.13

2.13. The same region containing both the large Te inclusion and a part of the surface scratch is highlighted by a black oval in Fig. 2.13 and Fig. 2.15. The PL spectra composing the maps of Fig. 2.15 were acquired with a scan resolution of 20 μm per step and every pixel corresponded to an emission spectrum. The PL spectra were processed by integrating over the near band-gap emission peak (Fig. 2.15 left), the A-center emission peak (Fig. 2.15 center), and 0.78 emission peak (Fig. 2.15 right). Different colors in maps of Fig. 2.15 correspond to different values of integrated intensity over the relative peak emission. Light scattering produced by the surface damage reduces the intensity of the emission in correspondence with the scratch in the case of band-gap and A-center emission. On the contrary, no considerable variation of integrated intensity over these two emission peaks can be associated with the presence of the large tellurium inclusion. The same holds when integration over 1.07 eV emission band is considered. A different behavior is observed in case of the integrated intensity over the mid-gap emission (Fig. 2.15 right). The integration shows a strong enhancement (the value of the integrated intensity doubles), of mid-gap emission in correspondence with the large Te inclusion. Raster scan resolution is comparable with the dimensions of the studied inclusion, according to that the maximum of the emission intensity is occurring in one single pixel and a weaker emission enhancement is noted away from the region surrounding the inclusion. Thus, a second scan was carried out focusing on inclusion region and increasing the scan resolution to 8 μm per step. The resulting map is shown in Fig. 2.15, and in this case the convoluted intensity profile is also shown. Spectra were processed with the same integration parameters used for generating the map in Fig. 2.15 (right). The presence of enhanced mid-gap emission, correlated to the inclusion, was confirmed by this second measurement. PL measurements show a clear spatial correlation between the position of Te inclusion and an enhancement of the emission

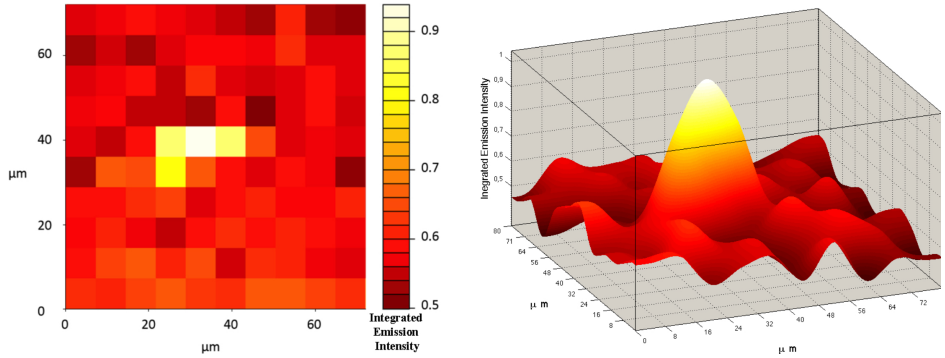

Figure 2.16: 77 K PL maps reporting the integrated intensity of the mid-gap emission band: color-map (left) and PL intensity profile (right). The resolution of the scan is 8 μm.

intensity over the peak at 0.78 eV. Thus, it is supposed that the presence of tellurium inclusion entails an increase of defect concentration, which is responsible for the emission at 0.78 eV with respect to the inclusion-free zone. The increase of mid-gap level emission close to inclusions is typical of samples that show an appreciable emission from these levels also far from inclusions. On the contrary, samples not showing emission from the level at 0.78 eV in the regions free from inclusions do not show emission from this level also around tellurium inclusions. This is not surprising, in the hypothesis that the lack of deep level emissions is mainly related to Fermi level position. Different hypotheses can be formulated about the origin of the mid-gap defect. Any hypothesis must take into account the experimental results shown in Figs. 2.14-2.16 and previous experimental results on the optical emission at 0.78 eV. It seems that two main explanations can be formulated. First, we can suppose that around tellurium inclusions, CZT lattice is tellurium rich, thus promoting the formation of tellurium antisite defect that is often reported to produce an energy level close to 0.78 eV [44]. A second possible explanation originates from the observation that the region surrounding Te inclusions is characterized by the presence of dislocations [35]. As pointed out before, dislocations were considered to be responsible for optical emission at mid gap. Hence, the enhancement of the 0.78 eV emission band close to tellurium inclusions could be attributed to the presence of dislocations surrounding inclusions. Actually, we must also take into account that dislocations usually getter impurities, so that the emission at 0.78 eV could be in principle a consequence of the dangling bonds caused by dislocations or an effect of particular impurities gettered by dislocations. Whatever the origin of this emission, mid-gap levels are known to be potentially active as recombination centers for non-equilibrium carriers. Thus, the presented data are in agreement with other

studies that showed a deterioration of the detector properties in presence of Te inclusions [31]. However, while previous studies are mainly focused on the detrimental effects of inclusions on the charge collection, the shown results suggest that the degradation can be caused by the presence of deep levels generated by defects surrounding inclusions. The present result is in accordance also with the correlation observed between carrier life time and medium inclusion density in detector grade CdZnTe crystals [46].

2.3.3 Conclusion

Thanks to the use of instrumentation for 3D reconstruction of tellurium inclusion position it was possible to prepare samples having large tellurium inclusions close to the surface. In this way, the modification of the luminescence properties of a CdZnTe sample in the presence of large Te inclusions was studied. PL maps showed a strong enhancement of mid-gap emission band in the volume of the sample surrounding the inclusions. The origin of this emission band can be ascribed to the dislocation network surrounding the inclusion or to the presence of large density of point defects such as tellurium anti-sites. However, whatever the defect responsible for this emission, mid-gap levels act typically as lifetime killers for carriers. Thus, the shown results indicate that the degradation of detector properties induced by inclusions could be attributed to the recombination properties of defects surrounding them.

2.4 Inclusion density reduction in CZT crystals by pulsed laser irradiation

Different post-growth annealing treatments have been proposed to eliminate Te inclusions. Thermal treatments under Cd-pressure [47], Te-pressure [48], or evaporating CdZn alloy powders were proposed [49].

Two step annealing (the first in Cd vapors, the second in Te-vapors) demonstrated to be effective in order to preserve the material high resistivity [50].

In the case the sample experienced a temperature gradient during the heat treatment, it was shown that Te inclusions thermo-migrate towards the high temperature region [51]. This happens due to the increasing solubility of CdZnTe in liquid Te with temperature.

However, in spite of the efforts, the ideal post-growth thermal treatment, capable of eliminating Te inclusions, keeping electrical resistivity very high, and at the same time improving detector

performances in terms of charge collection efficiency and energy resolution is still missing. This is also because, during the heat treatment, impurities segregated inside Te inclusions are dissolved in the crystal matrix and, in general, a different defect equilibrium is obtained, with string consequences on material resistivity and carrier traps.

A different approach to eliminate Te inclusions was based on the thermo-migration of Te impurities under the presence of a pulsed laser source [52]. At the employed wavelength (10.2 μm from a CO_2 laser source) not only CdZnTe crystals are transparent, but also Te inclusion absorption is low: for this reasons the sample was heated at 300 °C. Laser-induced thermo-migration was observed, but the movement of Te inclusions was low (3 μm/h at most).

In the following sections it will be show that, by means of a pulsed laser at 1.064 μm, is possible to eliminate Te inclusions at room temperature, avoiding high temperature processes that can modify the defect equilibrium in CdZnTe crystals. Moreover, the whole process is live-monitored so that parameters can be easily optimized.

2.4.1 Experimental

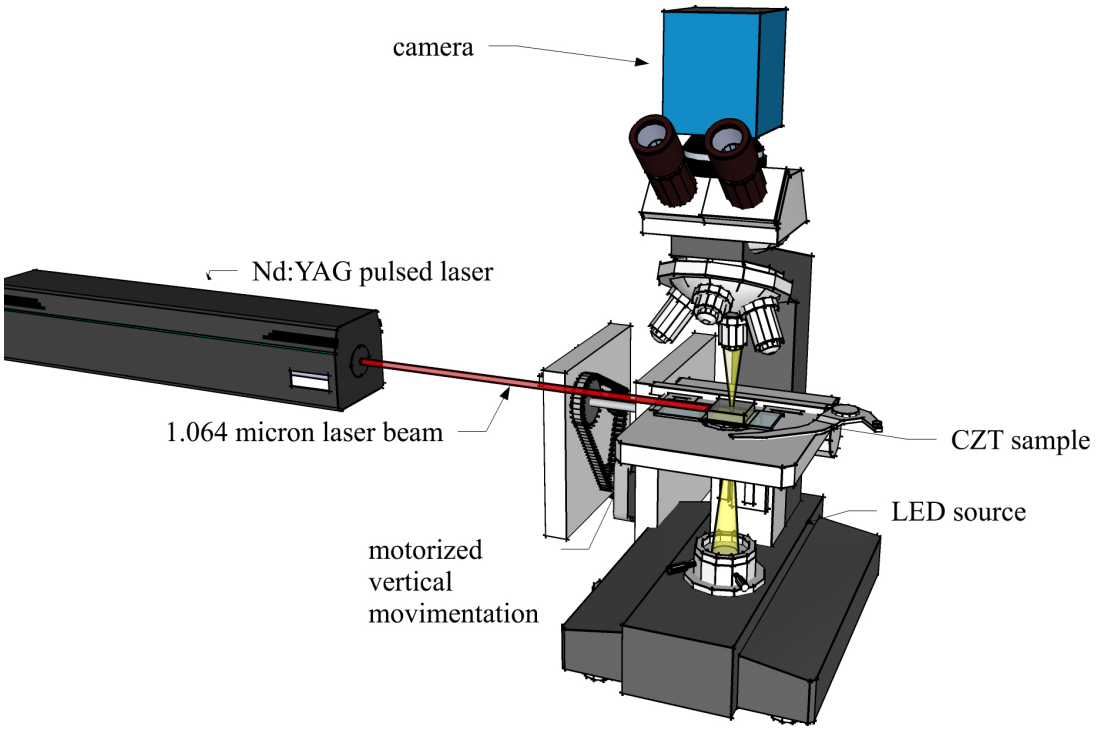

Figure 2.17: Scheme of proposed laser-induced thermo-migration system. Pulsed Nd:YAG laser radiation at 1.064 μm was adopted.

An innovative experimental setup based is shown in Fig. 2.17. Customary IMEM-grown CdZnTe sample was both side polished so that infrared spectroscopy is possible. Moreover, other two opposite sample surfaces are polished in order to ease the lateral laser irradiation. The sample is mounted on the x-y stage of the microscope used to evaluate the 3D reconstruction of tellurium inclusion described above. It is worth repeating that microscope infrared radiation is given by a 0.870 μm LED: at this wavelength CdZnTe is transparent, while Te inclusions appear like dark spots (see for example Fig. 2.18). CdZnTe sample is irradiated through one of the polished lateral surfaces by a 1.064 μm Nd:YAG pulsed laser beam. The duration of the pulses is 5 ns and the repetition rate can be increased up to 20 Hz. During the laser irradiation pictures are taken (laser trigger is used to trigger also the digital camera so to avoid that pictures suffer from stray pulsed laser radiation), and the whole process is live-monitored.

2.4.2 Results and discussions

As soon as the laser beam start to irradiate the sample, Te inclusions start to move toward the direction of the incoming laser beam. In Fig. 2.18 the typical evolution of Te inclusions under laser radiation is shown at three different process times.

During this particular experiment, repetition rate was 10 Hz and energy density for each pulse was 0.16 J/cm^2. Fig. 2.18 (top) show the sample before laser irradiation starts.

Three sets of inclusions are considered: inclusions with a diameter lower than 2 μm, red circled in Fig. 2.18, inclusions with a diameter in the range $(2 \div 5)\mu$m, green rectangle in Fig. 2.18 and inclusions larger than 10 μm, blue pentagon in Fig. 2.18. That figure also show system evolution after 5 hours and 15 hours.

Inclusions with diameter lower than 2 μm thermo-diffuse towards the laser beam and are finally dissolved in the CdZnTe matrix as it can be seen in Fig. 2.18 (red circle). Inclusions with $(2 \div 5)\mu$m diameter do not move as a whole, but are broken into smaller parts that thermo-diffuse, generating a tail that becomes longer with time, and finally also dissolve in the crystal matrix, Fig. 2.18 (green rectangle). Also the largest inclusions, do not move, neither are dissolved at the end of the treatment (15 hours, Fig. 2.18 (blue pentagon). After 15 hours the process was stopped, also because, it was observed that dissolution process of inclusions is not proportional with time. At the beginning, the process seems to be quite fast, then, with time, the overall efficiency seems to reduce. This can be understood if a closer look is given to the tail originated by the laser activated thermo-diffusion process. The tail seems to be formed by small tellurium inclusions, whose dimensions is close to the spatial resolution of the optical system

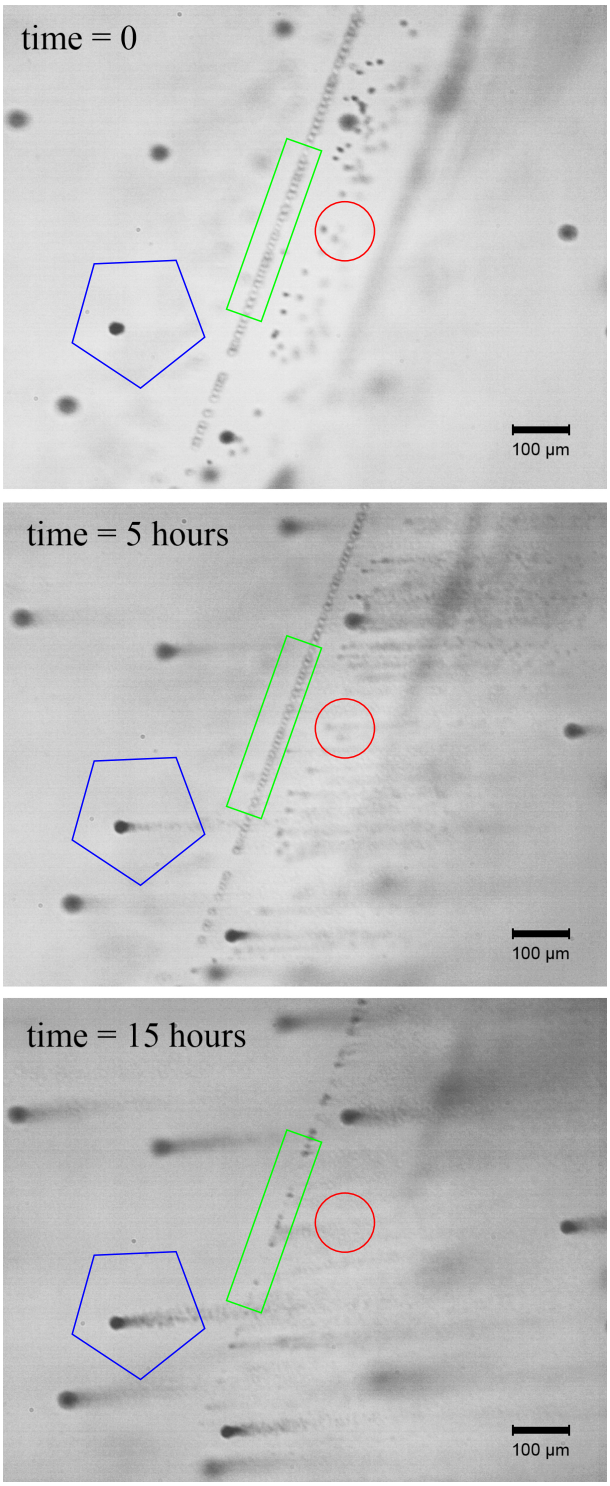

Figure 2.18: System evolution : sample before laser irradiation starts (top), after 5 hours (middle), and after 15 hours (bottom).

Fig. 2.19. Thus, the tail also absorbs laser radiation, so that the quantity of laser energy that reaches large inclusions diminishes with time.

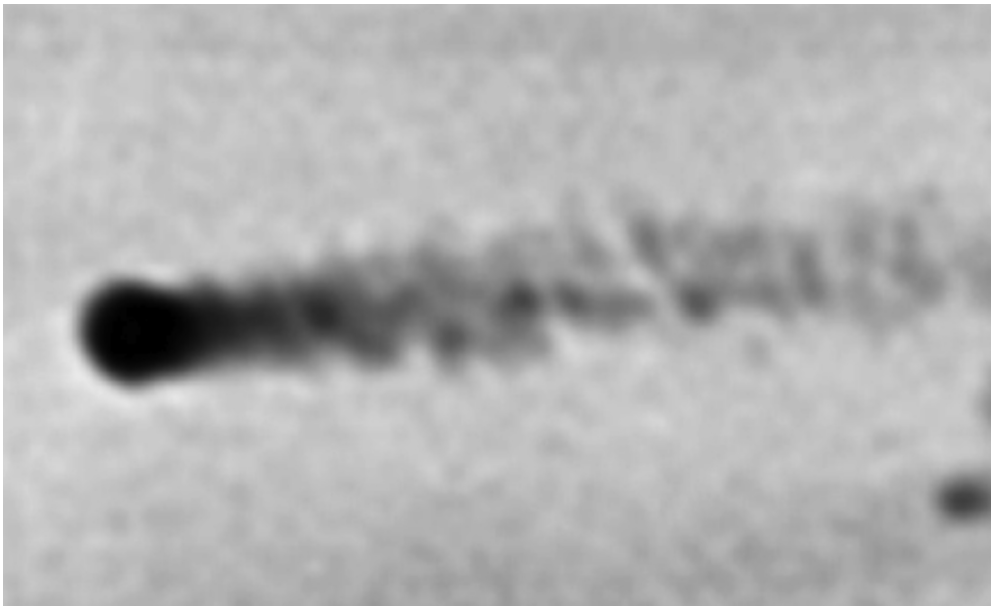

Figure 2.19: The tail formed as a consequence of the laser irradiation of large inclusions is actually formed by smaller tellurium inclusions.

The mechanism for diffusion of inclusions under laser irradiation can be described as follows. Tellurium inclusions efficiently absorbs 1.064 μm laser radiation, melt, and reach a temperature high enough that the solubility of CZT in Te is not negligible. At 800 °C solubility of CdTe in Te is about 20% [53]. Heat is transferred from the inclusion to the surrounding CZT matrix, however, the surface of the inclusion exposed to laser radiation is hotter than the other, so that the part of the crystal in contact with inclusion towards the laser beam is preferentially solved. Then, the system cools down, the result being the movement of the inclusion towards the laser beam.

In order to activate the mechanism it is necessary that the laser pulse energy density J_0 is at least:

$$\begin{aligned} J_0 =& \frac{1}{\pi R^2}\left(Q_{Te(s)} + Q_{Te(l)} + Q_{Tef} + Q_{CZT} + Q_{CZTSol}\right) = \\ =& \frac{1}{\pi R^2}\left(\int_{20}^{450} n_{Te}\rho_{Te}c_{Te(s)}dT + n_{Te}H_{f(Te)} + \int_{450}^{800} n_{Te}\rho_{Te}c_{Te(l)}dT\right) + \\ +& \frac{1}{\pi R^2}\left(\int_{20}^{800} n_{CZT}\rho_{CZT}c_{CZT}dT + n_{CZT}H_{f(CZT)}\right) \end{aligned} \tag{2.4}$$

where R is the inclusion radius, $Q_{Te(s,l)}$ is the heat necessary to raise the tellurium inclusion

temperature up to the melting point (450°C) and from melting point up to 800°C, Q_{Tef} is tellurium latent heat, Q_{CZT} is the heat to raise CZT temperature up to 800°C, and Q_{CZTSol} is the heat that is necessary to spend to solute CZT in Te at 800°C. The first four quantities are easily determined taking into account Te and CZT thermodynamic data [54, 55] and making the hypothesis, as a first approximation, that only the CZT that solves into the Te inclusion is actually heated. The last quantity in Eq.2.4 is more difficult to evaluate, however, the heat necessary to solve CZT into Te can't be larger than the latent heat of CZT, and, also this is only 15% of the quantity in Eq.2.4. Fig. 2.20 shows the dependence of J_0 with inclusion diameter

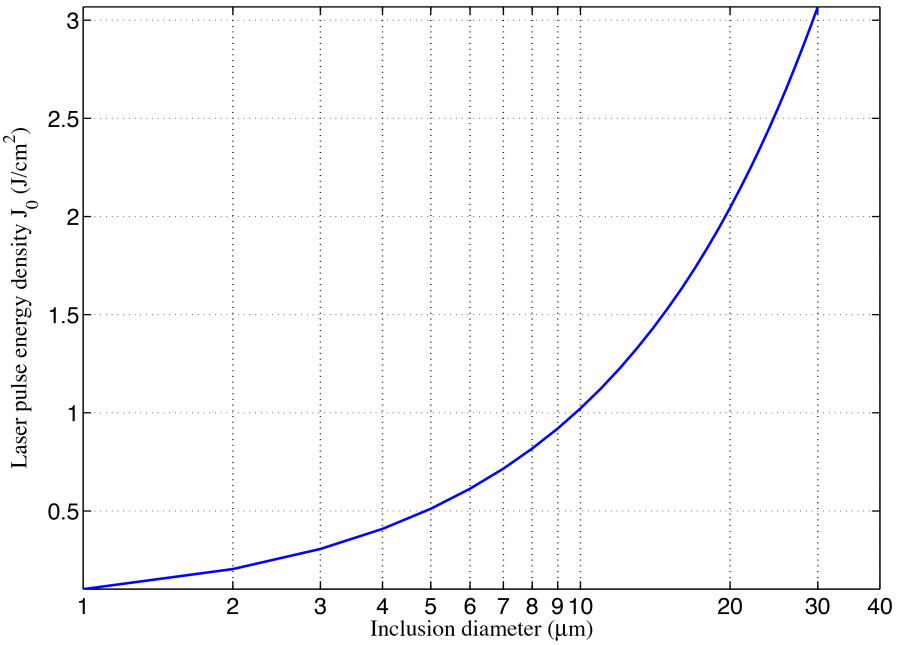

Figure 2.20: Calculated laser pulse energy density to melt inclusion, as function of inclusion diameter.

$2R$ as calculated by Eq.2.4. If we consider that in the described experiment, the energy fluency was 0.16 J/cm^2, we deduce that only inclusions with a diameter between $(1 \div 2)\mu$m can be actually moved, as shown by experimental data. Larger inclusions require a higher energy to heat up and melt. In this case only a part of them melts and diffuse, originating the tail shown by Fig. 2.18 and Fig. 2.19.

Fig. 2.20 also suggests that in order to melt the largest inclusions found in our samples (about 20 μm), the pulse energy fluency must be larger than 2 J/cm^2. For this reason, laser pulse energy was increased, causing the damage of the sample surface. We observed a damage of the sample entrance surface, after a lot of pulses, for energy fluency larger than 0.32 J/cm^2, that

correspond to an intensity of 0.064 GW/cm^2. Following the interpolation of the curve for laser damage threshold as a function of pulse duration reported in [56], it is obtained a value of 0.14 GW/cm^2 for one-shot pulse; so the result is not in contrast with our observations. In the same paper, it is shown that the laser damage threshold is inversely proportional to the square root of pulse duration. This means that the pulse energy density can be increased by increasing pulse duration. Following the dependence reported in [56], it is possible to calculate the maximum energy density that can be used before surface damage occurs a s a function of pulse duration. The results are synthesized by Fig. 2.21. From that figure is also clear that with a pulse of 100

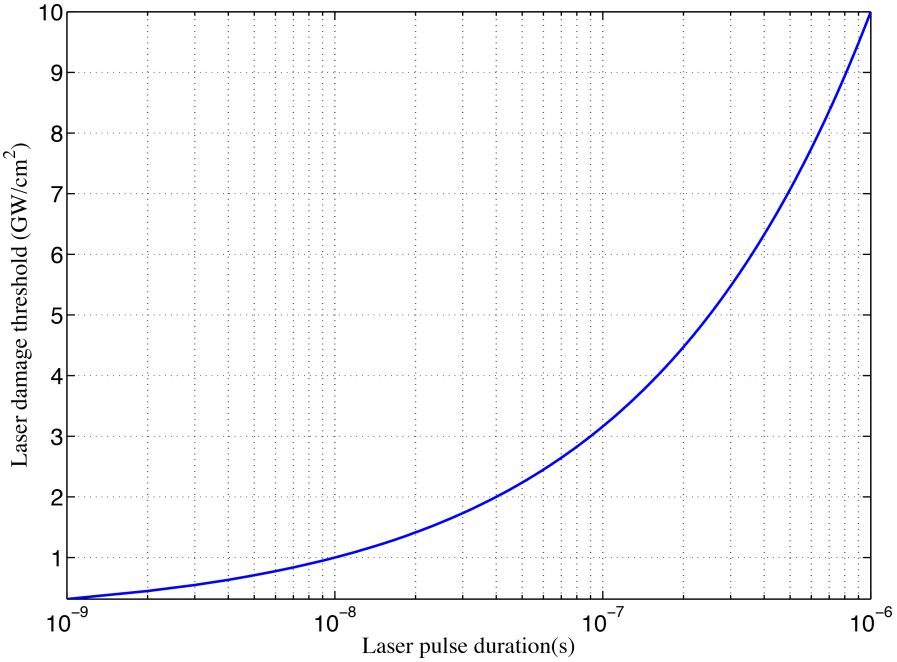

Figure 2.21: Calculated laser power density threshold as function of pulse duration.

ns it is possible to transfer to the system an amount of energy that is enough to move inclusions without damaging the sample surface.

On the other side, the considered pulse duration (100 ns) is still small enough to prevent energy dissipation. In fact, the heat diffusion length δ is given in first approximation by $\delta = \sqrt{D \cdot t}$ where D is the thermal diffusivity of CdZnTe. Considering a pulse duration of 100 ns and the thermal diffusivity of CdZnTe 0.013 cm^2/s [54], the diffusion length is only 0.3 μm. This means that during the pulse, there is no heat dissipation over a distance larger than the quantity of material that we want to dissolve.

2.4.3 Conclusion

In conclusion, we have shown that tellurium inclusion can thermo diffuse in the presence of Nd:YAG laser irradiation. The mechanism is driven by the strong absorption of the light by tellurium inclusions. The amount of energy transferred to the system is compatible with the proposed diffusion mechanism. Even if it was not possible to obtain thermo diffusion of large inclusions, however, calculations showed that by using laser pulses of longer duration (about 100 ns) also large tellurium inclusions can diffuse without damaging the sample surface.

Chapter 3

Electroless gold contact deposition on CZT detectors by scanning pipette technique

The final cost of CdZnTe devices remains a limiting factor for large-scale applications of this type of semiconductor. One of the problems is connected with realization of metal contacts on semiconductor surfaces. Due to the difficulty to reproducibly obtain large single wafers with excellent detector properties, usually photolithography is carried out on a single device, strongly increasing the time required for device preparation and thus, detector cost. On the other hand, because of the important role played by metal-CZT interface on the performance of final device, special attention should be paid to the technology employed in metal contacts realization. Another difficulty arises due to thermal instability of CdZnTe crystals. Contacts must be deposited at low temperature and no thermal treatment above 150 °C can be carried out after deposition. As a result, evaporated contacts usually suffer for poor mechanical stability. Moreover, due to the fact that diffusion is extremely low at 150 °C, it is difficult to obtain ohmic contacts. For these reasons, one of the most exploited procedures for contact deposition is the so-called electroless technique [57]. Gold chloride solution reacts with CdZnTe surface and a gold layer is deposited. Actually, intra-layers are formed between the top gold layer and the bulk of the semiconductor as a consequence of the reaction, whose composition and thickness generally depend on the reaction parameters [58, 59, 60]. As a consequence, electroless gold contacts usually show a better mechanical stability and are more reproducible than evaporated

contacts. Of course, patterned contacts can be obtained also with electroless deposition by means of photolithographic procedures.

Recently, different ways for depositing liquids or suspensions were proposed having the advantage to control with high resolution the deposition pattern [61, 62]. In these cases, liquids or suspensions are basically delivered by a pipette moved by a high resolution PC controlled scanning system. Reproducible and low-cost method for gold deposition on CZT surface has been personally developed during PhD work, combining the scanning pipette technique and electroless deposition. Entire system was designed by the author of this thesis, such as management software that drive motors. Each part of the equipment was personally evaluated, bought and assembled. With this technique it is possible to avoid the photolithography process and still obtain complex contact patterns with good spatial resolution and high reproducibility. In particular it is shown that contacts with dimensions down to a few tenths of microns can be obtained. The contacts show good mechanical stability and optimal current-voltage characteristics. High-resolution CZT detectors have also been demonstrated by the use of this technology.

3.1 Electroless gold deposition on CZT

The development of a reproducible and high performance contact deposition technique met some difficulties. At IMEM institute the electrical contacts on CZT are deposited using a wet technique called "electroless deposition". In this technique an aqueous solution of $HAuCl_4$ (5%) is used to deposit a thin layer of gold on CZT surface. When $HAuCl_4$ salt is in an aqueous solution, the following reaction takes place:

$$HAuCl_4 + H_2O \rightleftharpoons H[AuCl_3OH] + HCl \tag{3.1}$$

In particular, without any external current, two reactions (one anodic and the other cathodic) take place simultaneously at the surface of the CZT crystal. The complete reaction is:

$$2H[AuCl_3OH] + CdZnTe \rightleftharpoons 2Au + CdCl_2 + ZnCl_2 + TeCl_4 + 2H_2O \tag{3.2}$$

In this reaction Au atoms are deposited on CZT surface and $CdCl_2$, $ZnCl_2$ and $TeCl_4$ salts are dissolved in the solution. The thickness of the gold layer roughly increses as the square root of the time of reaction and the typical deposited thickness is around 600 Angstrom. In this type of process a significant amount of gold diffuses into the bulk following the same square root law creating a thin highly doped region under the contacts. Due to the low doping efficiency

of gold, however, perfect ohmic contacts cannot be achieved by using this method on CZT. At IMEM-CNR institute the standard deposition is obtained with 1 min of reaction at 20°C. Using this procedure a good reproducible contact can be deposited on CZT crystals.

3.2 The scanning pipette techinque, system description

The scheme of the scanning pipette technique is given in Fig. 3.1. The pipette, filled with 5% gold chloride solution in water, is moved in three dimensions by three stepper motors with resolution down to 1 μm.

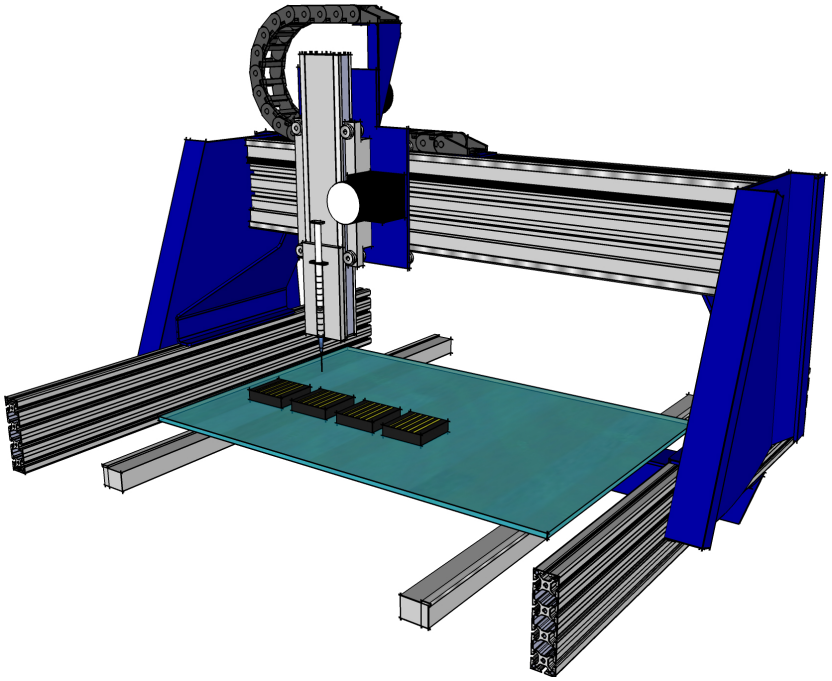

Figure 3.1: Scheme of scanning pipette system for the deposition of electroless gold contacts.

Pipette made of different materials were adopted. Iron-based pipettes suffered from corrosion effects originated by the acid solution. Glass showed an excessive wettability. Alumina and polyvinyl chloride (PVC) pipettes both guaranteed chemical stability and proper wettability, however the former also had a superior mechanical stability, because is more rigid. The surface scanned is 14x14 cm^2, that is typically larger than the dimension of CdZnTe or CdTe wafers available on market. A fourth stepper motor controls the movement of pipette piston and so the final fluid flux delivered by pipette. A digital microscope is mounted on the scanning head so that delivery process in continuously monitored. All stepper motors are controlled by a

personal computer by means of dedicated software.

3.3 Deposition process: pattern reproduction investigation

Deposition process is carried out as follows; first of all, pipette tip is brought close to sample surface. Then, pipette piston is moved, so that a drop of solution gets out of tip, wets sample surface, and a stable meniscus is formed. A typical picture of the begin of deposition process is shown in Fig. 3.2; in this type of deposition 15 μm inner hole Al_2O_3 pipette was used. It is evident that the resulting gold contact is slightly larger than the pipette outer diameter (50 μm).

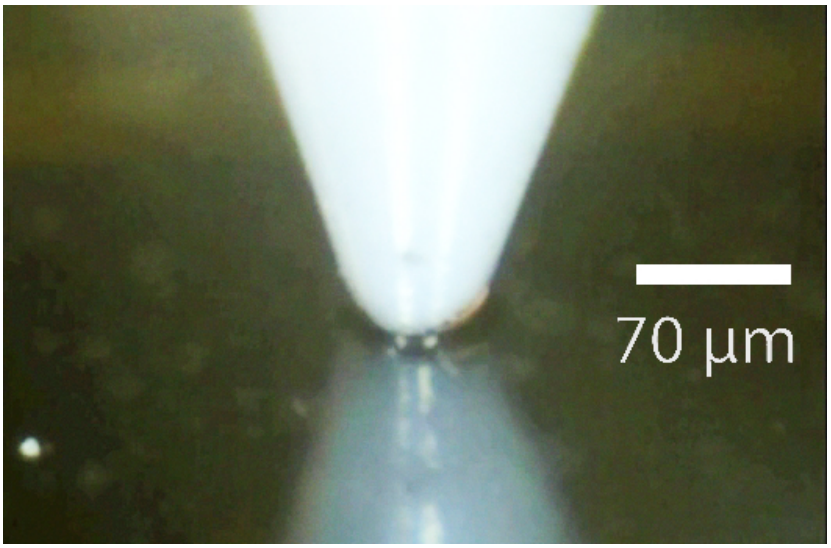

Figure 3.2: Picture taken during contact deposition with Al_2O_3 pipette with 15 μm inner hole and 50 μm of outer diameter.

The contact pattern defined on personal computer is reproduced on sample by scanning the pipette parallel to sample surface. Software also manages scanning speed and solution flux out of pipette. These parameters can be optimized in order to obtain a homogeneous contact thickness, together with a proper design of the path followed by the pipette. After deposition, water evaporates in a few hundreds seconds from the thin deposited layer and a stable contact is formed on CdZnTe surface.

Fig. 3.3 shows three examples of gold contact deposition by the scanning pipette technique.

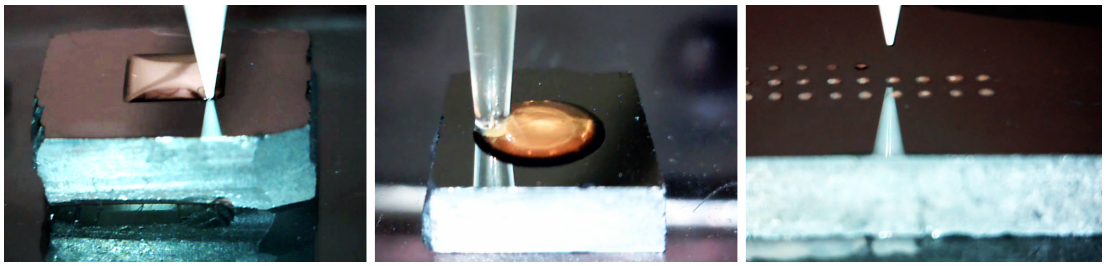

Figure 3.3: Deposition of electroless gold contacts. Square contacts with an alumina pipette (left), large circular contacts with PVC (center), small dots with alumina pipette (right).

Square contacts (Fig. 3.3 left), or circular contacts (Fig. 3.3 center and right) were deposited. In the case of Fig. 3.3 left and Fig. 3.3 right, 100 μm inner diameter alumina pipette was used, while in the case of Fig. 3.3 center 1 mm diameter PVC pipette was employed. Accordingly, square, circular contacts or small dots could be obtained. As will be discussed later the final dimension of the dot depends on the dimension of the liquid drop that forms out of the pipette.

Recently, sub-micron pipette were successfully used for depositing, for example, conducting polymers [62]. This is well beyond the resolution required in the context of x-ray detection that is in the range of tenths of microns. The time required to deposit contacts depends on the scanning speed of the system and the complexity of the pattern. However the total time for the deposition process is $(1 \div 100)$s that is much less than the time required by photolithography process.

By means of an appropriate software it is also possible to recognize the sample position on the bench and to optimize the alignment of each sample and the pattern of the contacts to be deposited.

In the following sections it will be reported some deposition results obtained using Al_2O_3 pipette (15 μm inner hole, 50 μm of outer diameter).

First of all we tested the system for the deposition of 150 μm dot contacts. The result is shown in Fig. 3.4. The dots show reproducible geometry and dimensions. The contacts are disposed in the nodes of a 350 μm grid pattern with the 1 μm resolution of the scanning system. The thickness of the gold deposition was 58 nm as determined by the use of a profilometer, which is quite a typical thickness for electroless gold contacts [58, 63].

Gamma rays imaging devices can be obtained realizing pixels directly on the CdZnTe detector surface [64]. For this reason, it was important to demonstrate that it is possible to obtain pixels by means of the scanning pipette technique. Fig. 3.5 reports the results relative to the

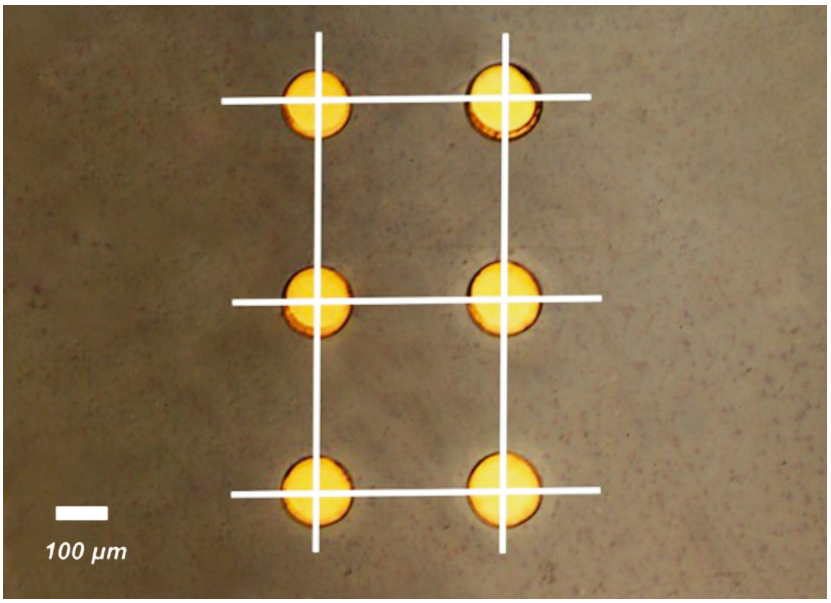

Figure 3.4: Electroless gold dots deposited on a CdZnTe sample by the scanning pipette technique. Dots show reproducible dimensions and are located at the nodes of a 350 μm grid pattern.

realization of a 250 μm pixel. In fact most of the imaging applications require pixels even larger than 250 μm, also due to the fact that for smaller pixel dimensions charge sharing phenomena occur [65].

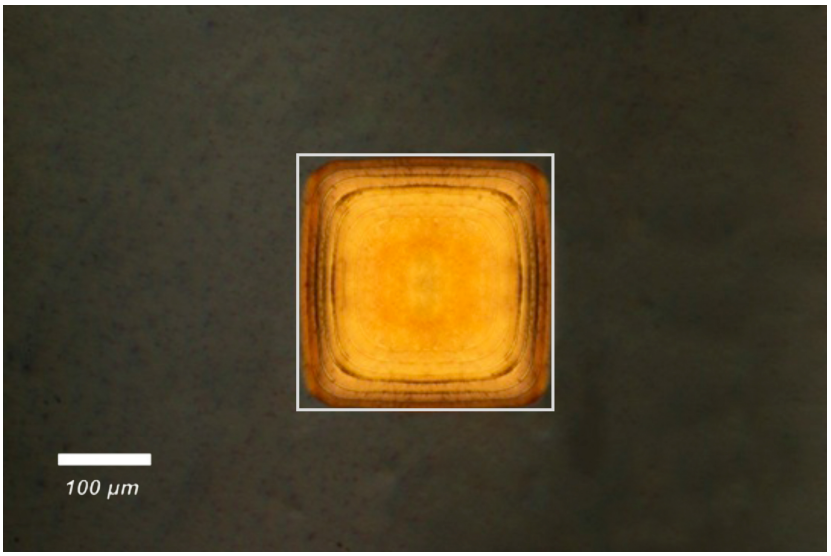

Figure 3.5: 250 μm pixel deposited by the scanning pipette technique. A perfect 250 μm square is also plotted with a white line for comparison.

A perfect 250 μm square is also plotted for comparison. The obtained pixel deviates from the perfect shape only at the corners that are slightly rounded (area deviation less than 2%). Actually round corners could also avoid not-uniform field effects.

Finally, as we shall see in the last part of the thesis, it was demonstrated that it is possible to obtain 2D and also 3D detectors also by the use of micro-strips devices. Thus, we deposited on a CZT sample a set of stripes with 300 μm pitch. The result is shown in Fig. 3.6. The stripe width is 70 μm. This is also the minimum stripe width that was possible to obtain with the alumina pipette.

Figure 3.6: Gold electroless stripes deposited by the scanning pipette technique on a CZT sample.

This dimension is actually larger than the inner diameter of the pipette (15 μm), and also larger than the outer diameter of the pipette tip (50 μm). This is because, due to surface tension effects, the liquid drop that is formed between pipette tip and CZT surface has a truncated conical shape, with an upper surface that coincides with the whole pipette tip (see Fig. 3.2).This means that the intrinsic spatial resolution of the scanning pipette technique is, in first approximation, limited by the outer diameter of the pipette.

3.4 Detector characterization:contact quality investigation

In the following sections we report some characterization performed on CdZnTe spectroscopic grade detectors in order to test the quality of the metallization realized with the scanning

pipette technique. First of all gold electroless contacts were realized on opposite sides of CdZnTe samples by scanning pipette technique. 7x7 mm^2 samples, about 2.5 mm thick, were cut from high resistivity crystals doped with indium and grown in our laboratory by Vertical Bridgman [25, 27].

A second issue concerns the formation procedure of the gold contacts by means of the scanning pipette technique. In the typical electroless procedure, a CZT detector is sunk in the gold chloride solution for a fixed time, than it is cleaned with the proper solvent. In the case of the scanning pipette technique, a fixed quantity of solution is delivered on the detector surface, gold chloride reacts with CZT and solvent mainly evaporates before the washing procedure. In order to test the quality of the obtained contacts, we realized detectors on a spectroscopic grade CZT sample, also obtained in our laboratories. In particular direct comparison between normal and "printed" contacts on the same CZT crystal was explored.

3.4.1 Electrical measurement

The contacts were initially tested by current-voltage measurements at 23 °C. The typical current-voltage characteristics obtained by electroless gold contacts deposited by scanning pipette technique are reported in Fig. 3.7. The characteristic is typical of two back-to-back diodes realized on high resistivity material [29]. In case of X-ray detectors, while injecting contacts should be avoided, it is still controversial if ohmic or blocking contacts should be preferred. However, different authors report that blocking contacts as shown in Fig. 3.7 are optimal for obtaining good quality X-ray detectors [29, 66, 67]. In any case, the current-voltage characteristic shown in Fig. 3.7 is similar to the one that we usually obtain on our crystals by standard electroless procedure [28].

3.4.2 Spectral response measurement

The obtained devices were moreover irradiated with uncollimated Am-241 radiation source. An electric field of about 100 V/mm was applied and a shaping time of 2 microseconds was used to form the signal. The acquisition was achieved by means of a Cremat CR110 preamplifier, a ORTEC 570 shaping amplifier, and a Aptec 8000 multi-channel analyzer. Detectors realized using scanning pipette technique showed good response when exposed to Am-241 nuclear source, as shown in Fig. 3.8. No correction was applied to acquired data. The spectral resolution at 59 keV is 5% that is typical for the detectors prepared using CdZnTe crystals grown in our lab. The lowest energy peak (< 8 keV) is only due to electronic noise.

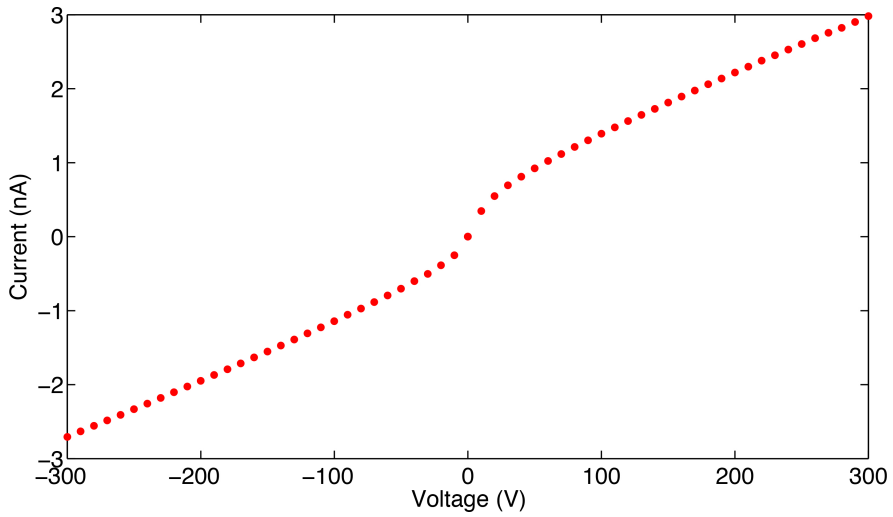

Figure 3.7: Current voltage characteristics of planar contacts obtained by the scanning pipette technique.

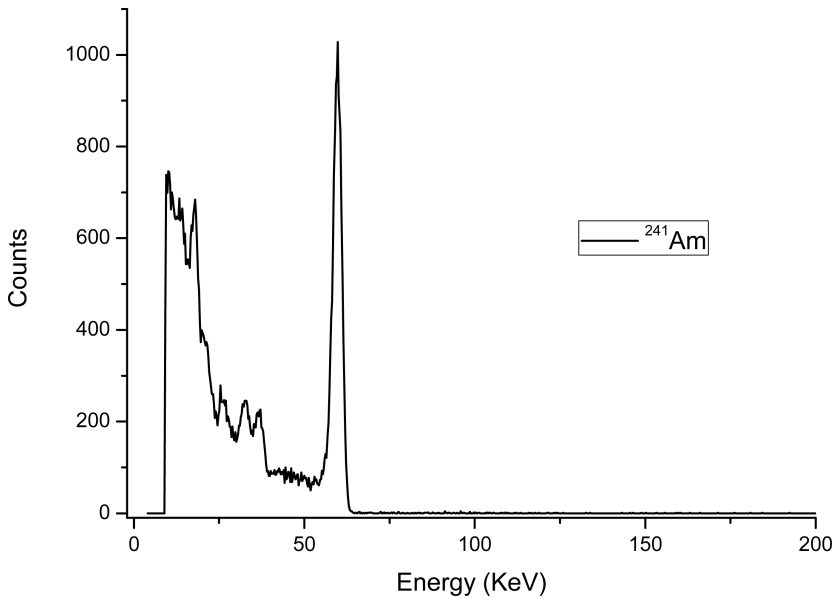

Figure 3.8: Response to Am-241 nuclear source of a CdZnTe detector with electroless gold contacts realized by the scanning pipette technique.

3.4.3 Collection efficiency measurement

As previously stated, in order to test the quality of the obtained contacts, we realized detectors on another set of spectroscopic grade CZT samples. Direct comparison between normal and "printed" contacts on the same CZT crystal was explored. At first we realize a planar detector with electroless gold contacts deposited by scanning pipette technique.

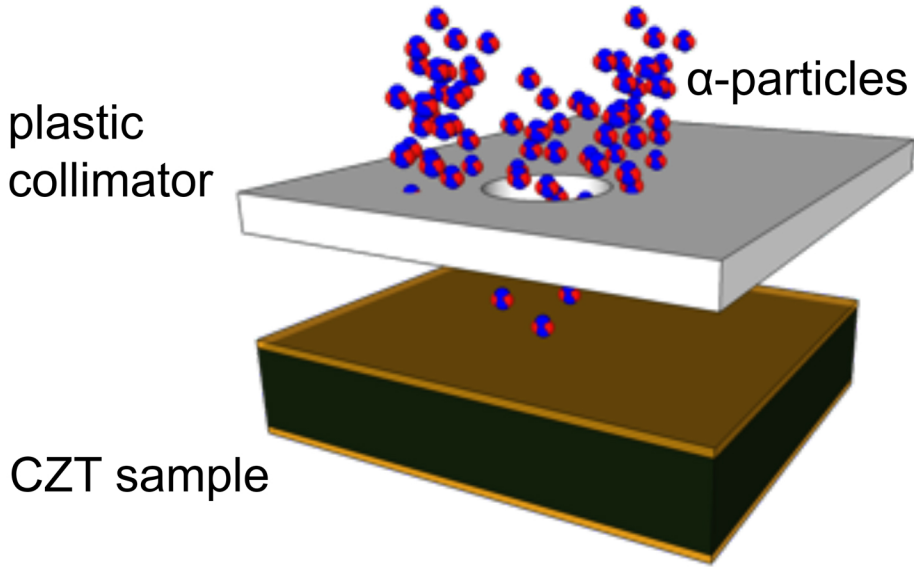

Figure 3.9: Geometry of the experiment for detector characterization with alpha particles.

After test we removed the contacts and we realize on the same crystal electroless contacts using the standard procedure (5% gold chloride water solution, and washing with water after 1 minute of reaction). This procedure was described in many papers [58, 60] and it ensures the formation of contacts with good spectroscopic performances, even if the mechanical adhesion is not completely satisfactory, and in any case comparable to other deposition technologies, such as sputtering or thermal evaporation [68]. The dimensions and the shape of the contacts were the same (8x5 mm^2). In both the cases, alpha spectra was recorded in order to test the contact behavior. The alpha particle source (Am-241) was fixed on a plastic collimator (see Fig. 3.9) with 1 mm hole. The sample was centered beneath the hole at a distance of about 5 mm from the americium source. The detector and the source were mounted inside a metal box (in air) connected to electronic chain. Applied voltage (200V), shaping time (2 ms), electronic gain, and measurement time (4 hours) were kept the same for the two measurements.

In order to study collection efficiency, comparison of the alpha spectra taken on the same sample with standard electroless contacts (black line) and electroless contact prepared with the scanning pipette technique (red dashed line) is shown in Fig. 3.10. As it can seen in the spectra, the center of the peak occurs at the same channel. This means that there is no change in the charge collection efficiency by changing the contact deposition technique. As it can be seen in the case of standard deposition process, the peak is broadened with respect to the scanning pipette technique case. This could be explained in terms of small different scattering

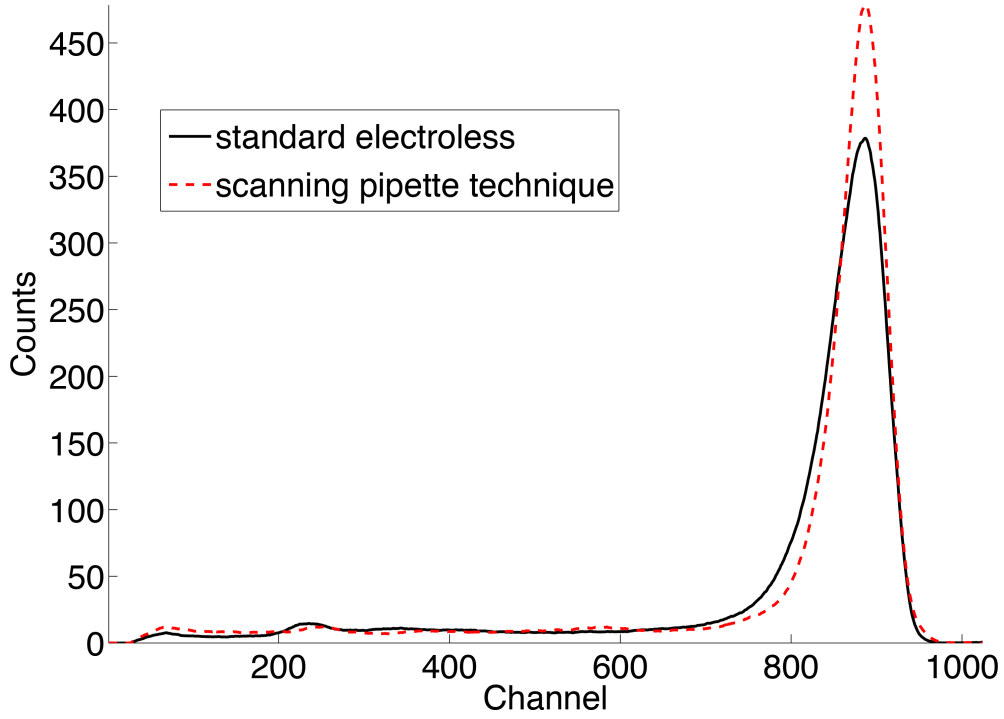

Figure 3.10: Alpha particle spectra of the same CdZnTe sample provided with standard electroless gold contacts (black line) and contacts realized by the sacnning pipette technique (red dashed line).

lengths of alpha particles in air, due to possible different distances between source and sample in the two measurements. This explanation is also confirmed taking into account the small diference in the integrated counts over all the channel (less than 3%). In any case Fig. 3.10 demonstrates that contacts prepared with the scanning pipette show at least the same charge collection performances of contacts prepared by standard water-based electroless deposition.

3.5 Conclusion

In conclusion, it has been shown that the scanning pipette technique can be used to deposit patterned contacts with electroless method without using photolithography procedures. The possibility to deposit different patterns has been tested: large area squared and circle contacts, micro-dots, pixels, micro-stripes, whose dimensions are compatible with the ones required by typical devices. Alumina pipettes can be advantageously employed because inert to acid solution, mechanical stable, and enable the formation of a proper meniscus between the pipette and the sample surface. PVC pipette can also be adopted, although in the case of alumina one, pipettes with nozzle diameter down to few microns are available on the market (the same is not

true for PVC pipettes).

Obtained electrical characteristic of deposited electrodes was optimal for realization of X-ray detectors. X-ray detector response was measured showing good spectroscopic characteristics.

Moreover, detectors with contacts deposited by the scanning pipette technique show at least the same energy resolution and charge collection efficiency of detectors with standard electroless gold contacts.

The scanning pipette technique showed to be versatile and can be used also for deposition of others metals by using proper metal precursor solution. In fact by the use of the scanning pipette technique it is in principle possible to deposit different metal contacts such as platinum, ruthenium, and rhodium, by using the correct metal precursor solution [69, 70].

During PhD the author of this thesis was involved, as Bachelor's thesis co-supervisor, in an interesting collaboration with computer Engineering department of University of Parma. Purpose of this joint venture was design and develop an ad hoc management software to optimize equipment scanning head trajectory in order to obtain uniform surface contact deposition. Very interesting preliminary results were obtained and testing is still in progress.

Chapter 4

3D-CZT detectors

4.1 Introduction

During this work, the undersigned was involved in a very interesting project, funded by European Space Agency (ESA). The project, entitled "3D CZT High Resolution Detectors", was leaded by Doc. Carl Budtz-Jorgensen and Doc. Irfan Kuvvetli, from National Space Institute of Technical University of Denmark (DTU Space Center). This project started from original idea of Doc. Carl Budtz- Jorgensen and Doc. Irfan Kuvvetli that developed a novel type of CZT based detector: the drift stripes 3D detector.
IMEM-CNR institute was involved in some important parts of the project:

- Detectors preparation. All detectors and prototypes were completely made at IMEM by Nicola Zambelli and Giacomo Benassi.
- Detectors characterization. The detector characterization was performed at European Synchrotron Radiation Facility (ESRF) in Grenoble.
- Data analysis. The data analysis of the Synchrotron characterization.

In particular the undersigned and Giacomo Benassi were directly involved in the characterization at ESRF and the data analysis of the 3D detector.

4.1.1 3D drift stripes detector concept

Requirements of X and Gamma ray detectors for high energy astrophysics missions include high detection efficiency and good energy resolution as well as fine position sensitivity even in

3D. X-ray astrophysics missions in the keV to MeV band require advanced instrumentation with both spectral and imaging capabilities. The instrumentation for these types if telescopes require detectors of high efficiency, with energy resolution in the order of few keV and capability of 3D position sensitivity [71]. Compound room temperature semiconductor detectors such as CZT are good candidates for hard X-ray (higher than 10 keV) and Gamma-ray astronomy instrumentation. The most significant disadvantage for these type of detectors is the ineffective charge collection within the detectors, especially for holes which affect and degrade the detectors' spectral performances. The most significant improvement in this field was proposed by the DTU Space Center and it involves the application of the drift strip method on CZT detectors.

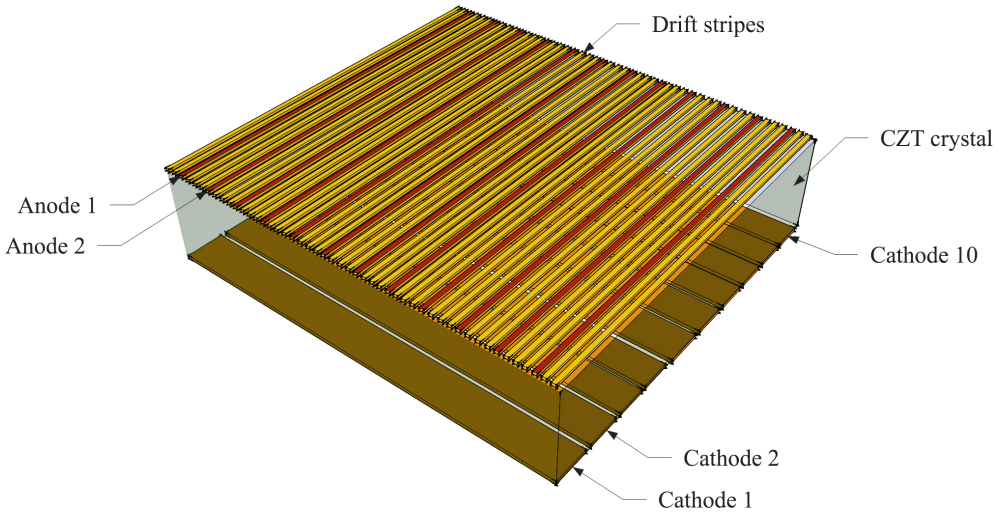

Figure 4.1: Principle of the CZT drift strip detector. The drift strip electrodes and the segmented cathode are biased in such a way that photo-generated electrons moves to the anode strips.

Fig. 4.1 shows the principle of CZT drift strip detectors, the detector structure is similar to the Silicon drift detector which was first time introduced by Emilio Gatti and Pavel Rehak in 1983 [72]. The structures employs a number of drift strips (three) separating each anodes readout strips on the upper side and a segmented (ten) cathode on the lower side. A voltage divider supplies each drift while the anodes strips are held at ground potential. The detector is biased such that the electrons, produced by the interaction of the incoming photons with CZT crystal, are drifted to an anode readout strip thanks to their transport properties; specifically $\mu_e\tau_e$ up to 10^{-2} cm^2/V for CZT. As we cited above, the positive charges (holes) produced by the photon interaction have a poor mobility-lifetime product ($\mu_h\tau_h$ up to 10^{-5} cm^2/V for CZT) and will, with high probability, be trapped in the detector. However, the anode signal is

unaffected by the holes since the anode strips are screened by the bias strips [73]. The anode signals are therefore proportional to the photon energy and high spectroscopic performance is ensured for CZT materials with good electron drift properties. Although the spectroscopic properties of these detectors type are almost independent of material holes transport properties, they are obviously very dependent on the electron transport properties; for this reason crystals with fluctuating electron trapping length will result in degraded detector performances.

4.1.2 Detector prepared during the project

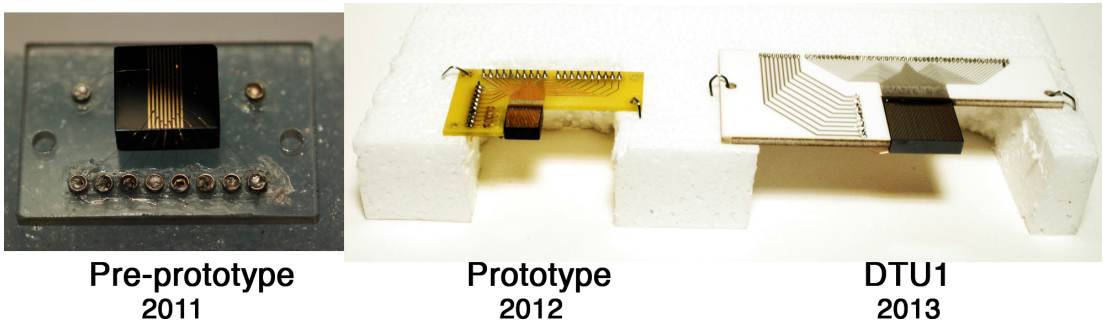

Figure 4.2: 3D CZT detector evolution.

For the 3D CZT detector project several detectors were made:

- The first 3D detector called "pre-prototype" was made in 2011 (Fig. 4.2 left) with dimensions of 10mm x 10mm x 5mm. It had only one drift cell (1 anode and 8 drift stripes) and a full area cathode electrode. Therefore this detector was not a real 3D but 2D images were measured.

- The second 3D detector called "prototype" was made in 2012 (Fig. 4.2 center) with dimensions of 10mm x 10mm x 5mm . It had 4 anode stripes and 13 drift stripes on one surface and 5 cathode stripes on the other side. This was a real 3D detector but, due to some problems related to the crystals-quality, it was impossible to characterize the properties of the final device.

- In 2013 (Fig. 4.2 right), four 3D detectors were made, labeled according to the order of preparation as DTU1, DTU2, DTU3 and DTU4. These detectors have 12 anodes, 37 drift stripes and 10 cathode stripes. The dimension of the crystals were 20mm x 20mm x 5mm. DTU1 was the only one detector without alumina layer among the anodes, the

drift stripes were deposited directly on passivated CZT surface. DTU2, DTU3 and DTU4 were realized depositing an alumina layer on the passivated CZT surface among the anode stripes, with the aim to reduce the leakage current between adjacent drift stripes. The DTU2 in particular was the detector that was characterized with the synchrotron beam at ESRF.

4.2 Detector preparation

The detector preparation still remains a critical step for obtaining high performance CZT detectors. Each step of preparation requires special attention and, for this project in particular, a lot of technological problems had to be solved. All the processes, that will be discussed in this chapter were performed by the undersigned and Giacomo Benassi using the IMEM-CNR facilities.

IMEM has a long experience in CZT detector preparation, in particular in the last 5 years several detectors were fabricated. The aim of these detectors was the characterization of the material grown at IMEM institute and therefore stan- dard detectors (planar detectors) were normally fabricated on relatively small CZT samples. For this reason the complexity of these 3D detectors required a different approach and an incredible effort was made in order to increase the quality and to solve problems of standard fabrication procedure.

The detectors were realized on crystals produced by Redlen. This choice was imposed by the committers (DTU), who selected the best commercial material on the market in a previous step of the project. The main challenge of the project can be described listing some features of these detectors:

- **size of the 3D detector**. Before this project the standard dimensions for detectors made in IMEM were 7mm x 7mm for 2 or 3 mm thick. For 3D CZT project the crystal size increased to 20mm x 20mm x 5 mm thick (commercial Redlen crystals) and, as will be discussed later, due to this reason, many processes had to be changed.

- **electrodes geometry complexity**. 49 stripes with 0.4 mm pitch (150 μm stripes width and 250 μm of space) constituted the anode electrode and 10 stripes constituted the cathode electrode. Therefore a double (at least) photolithography process on both surfaces was done representing one of the main challenge. Moreover such high number of independent electrodes required an extremely high uniformity of photolithography and contact deposition processes that was not trivial to reach.

- **extremely low currents requirement**. For 3D project there was the requirement to have the currents between adjacent stripes lower than 2 nA at -100V at T=22 °C. This because for this type of detector is very important to decrease the noise due to currents between stripes. As discussed before the control of surface resistivity is still an open challenge in the detector preparation technology. For this reason an alternative passivation process was developed during this project in order to decrease the currents between stripes. This process was used for the first time during this project and a lot of time was spent in order to develop all the procedures.

- **detectors bonding**. This process, as will be discussed later, was one of the main challenges in the project and in some cases was the critical step of the 3D detector realization. It was not trivial to make 50 electrical connections between detector and PCB, moreover these connections had to be mechanical stable (the detector were sent to Denmark) with a good electrical contacts (without any noise). For bonding a semi-automatic machine was developed, with this machine the bonding resulted more reproducible and faster than the manual process (used before this project).

- **detector PCB alignment**. These detectors had to be perfectly aligned to the PCB and, for making bonding, to the pads of PCB. The alignment with the PCB was fundamental for the characterization with Synchrotron beam. This because, due to the small dimensions of the beam (50 μm x 50 μm) any small change in the alignment angle of the detector with PCB could be a strong change in the real dimension of the beam detector interaction volume.

For all these reasons this project was a personal and a group challenge. All these problems represented a very interesting challenge that involves a lot of personal energies and time. Several persons of the IMEM-CNR institute were involved in some parts of the detector realization. It was impossible to solve all the problems for such as complex detector but finally very good results were observed during the characterization at synchrotron facility.
We are very proud with the results of this project and for all the developments that we made in all the detector preparation processes.

4.2.1 Detector preparation steps

All the 3D detector fabrication steps are shown in Fig.4.3 and they can be summarized as follow:

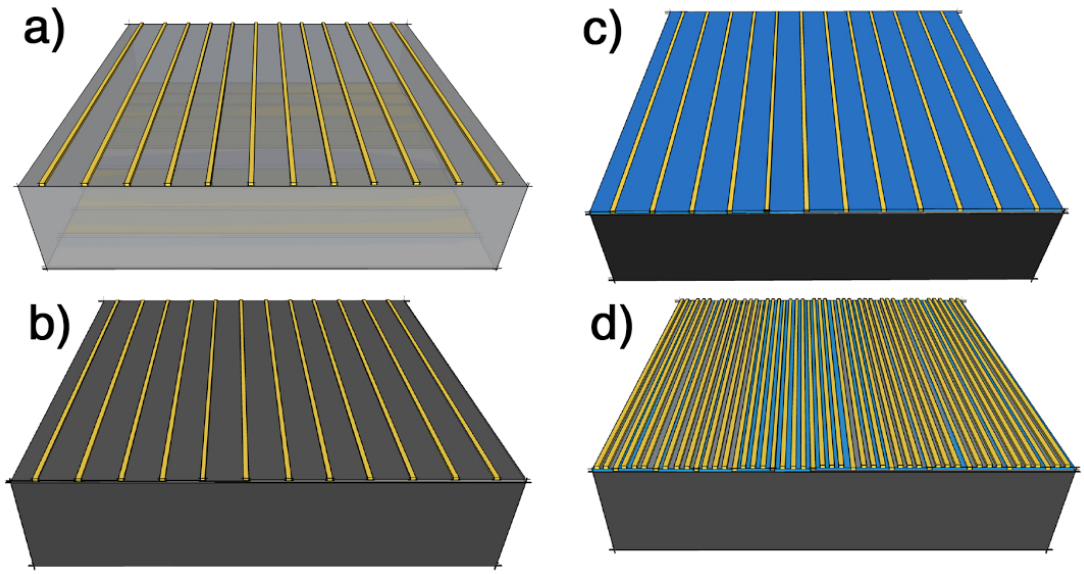

Figure 4.3: Sketch of the detector preparation steps. a) deposition of anode and cathode stripes, b) passivation of surfaces, c) alumina deposition (only for detectors DTU2,3 and 4), d) deposition of the drift stripes.

- **mechanical process**. In this process all the six surfaces of the crystal are polished and lapped, at the end of the process a sample with six mirror surfaces is made.
- **deposition of collecting electrodes**. In this step, using a double photolithography process, the 12 collecting anodes and the 10 cathodes are deposited. All these contacts are made of gold deposited via electroless technique (Fig. 4.3 a).
- **passivation**. In order to increase the surface resistivity a standard passivation process was made on all the surfaces of the crystals (Fig. 4.3 b).
- **alumina deposition**. First of all the deposited gold anode contacts (step 2) were protected using the photoresist deposited by photolithography process. Then a 150 nm Al_2O_3 layer was deposited with Pulsed Electron Deposition (PED) technique (Fig. 4.3 c). This step was done only for detectors DTU2, DTU3 and DTU4.
- **deposition of drift stripes**. On passivated CZT surface and/or on alumina layer gold drift stripes (non collecting electrodes) were evaporated. Also for this deposition a photolithography process was necessary (Fig. 4.3 d).

In the following, all the single processes will be discussed, in particular: mechanical polish-

ing, photolithography, contact deposition, passivation, alumina deposition and bonding. In Fig. 4.4 some pictures of the detector during the processes are shown.

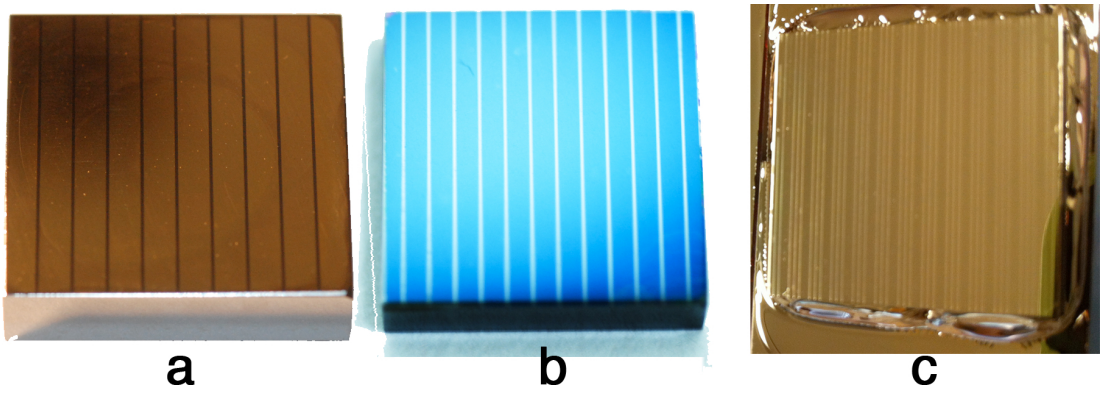

Figure 4.4: Some picture of the detector during the preparation: a) cathode stripes, b) alumina deposited by PED and c) the evaporated drift stripes.

4.2.2 Mechanical polishing

The Redlen crystals (dimension 20mm x 20mm x 5mm) are sold with pixelated gold anodes and planar gold cathodes this represents the standard detector geometry of this company. The first step was therefore to remove all the gold contacts from crystals. For this type of task a semiautomatic polishing technique was used. In this was also the control of the thickness can be made in a better way.
This technique consisted of a rotating plate where sandpapers with different grains were mounted. The system was equipped with bi-distilled water supplier in order to have the best lubrication on the sandpaper without introducing any type of impurities. We developed a standard procedure for mechanical processing that is working very well with CZT crystals.

- In the first step a paper with relatively large grain (p2500, 8.4 μm of average particle diameter) was used. The aim of this first stage was to remove a relative thick layer of material in order to eliminate the existing contacts and eventually the scratches present on the surfaces.

- In the second step p4000 SiC grains sandpaper (5 μm of average particle diameter) was used. This step is fundamental for subsequent machining, with p4000 all the remaining scratches must be eliminated. For this reasons this step is the longest one.

- After the lapping (process with sandpaper), the polishing procedure started. The sandpaper was replaced by polishing cloths. A set of abrasive diamond suspension was used with diameters ranging from 3μm down to 0.1 μm. The entire process required a usually one day for the two sides of each sample.

- After the polishing and the mechanical polishing the sample was cleaned with two hot solvents: acetone (10 minutes at boiling temperature) and isopropanol (10 minutes at boiling temperature).

Due to the big dimensions of these crystal special attention was taken in order to increase as much as possible the uniformity of the surfaces. This because is well known that due to mechanical polishing the peripheral area of the crystals can be reduced more than the central parts. This problem, that can be neglected in the small samples or using a chemo-mechanical process, required special tricks during the polishing (such as the double rotation of the sample).

4.2.3 Photolithography

Photolithography is the process normally used for making micrometer patterned contacts on a semiconductor surface. In this technique a UV light is used to transfer a pattern from a mask (made on quartz) to a light sensitive chemical photoresist, previously deposited, on the substrate. After the exposition of the resist to UV light a series of chemical treatments are used in order to remove the exposed resist if the resist is negative or the contrary if the resist is positive. After this process some parts of the sample are covered by a hard and chemical stable resist, other parts are free to be processed. The main steps of this technique are:

- Using a Sulzer Electro Technic spin coater a uniformly layer of resist, that is a high viscosity liquid, is deposited on the surface of the sample. The thickness of the resist layer spun at 4000 rpm for 30 sec is around 1 μm.

- The sample with resist is than baked in a special furnace at 90 °C for 30 min.

- Using a Karl Suss mask-aligner the patter of the mask is transferred to the resist (Microposit S 1813 G2). The resist used at IMEM is negative, the irradiated parts are removed by developer.

- After exposition the resist is removed by dipping the sample in a basic solution called "remover" at 20 °C for 1 min.

- At the end of the process the sample is cleaned with high purity water and than dried with argon gas.

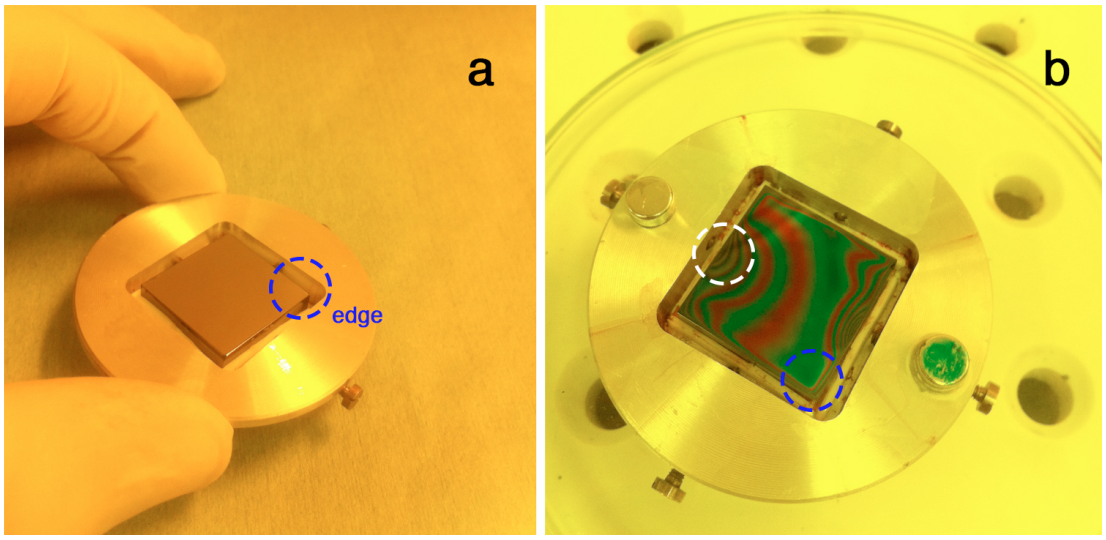

Figure 4.5: a) the chuck for non-rounded sample designed and realized for this project. b) using both chuck and plate a very uniform resist layer can be achieved.

All these process steps were made inside the clean room of the IMEM-CNR institute. Also for the photolithography process several developments were made for 3D detector fabrication. In particular the main problem was connected with the deposition of the resist on the sample. This because the sample area was large (compared with standard samples) with a non-rounded shape, for these reasons a thickening of the resist in the edges was found. During the rotation (that is needed to uniform the liquid resist on the sample surface) the solvent contained in the resist evaporates and the viscosity of the resist increases during rotation time. It is important that evaporation process happens relatively slowly in order to allow the liquid resist to cover the entire surface. If a non-rounded sample is rotated with the resist two main problems must be solved. The 4 edges of the square surface, during rotation, feel a tangential velocity higher than the central part of the sample. This means that the solvent contained inside the resist will evaporate faster in these edges. The result is that at the edges resist is too thick to be developed. To solve this problem a special chuck was designed and realized. This chuck has a rounded shape with a square hole for the sample (Fig. 4.5 a): in this way the geometry of the system is again circular. With this chuck an extremely uniform resist thickness was achieved also at the edges, therefore the either surface of the samples (20mm x 20mm) could be used (as

requested by the specifications of the project). The second problem was connected with surface area of the sample: the speed of the resist on the surface is not enough to eliminate the excess of the resist before the evaporation of the solvent. By putting a metal plate very close (1 mm) to the rotating surface this problem was solved. With a plate a local sovra-saturation of solvent was created close to the rotating surface and the effect was to decrease the evaporation velocity of the resist on the surface. With this plate and the chuck the resist had uniform thickness over all the sample as shown in Fig. 4.5 b, in particular it is possible to see that in correspondence of edges (blue circles) the resist results very uniform. In the white circle it is possible to see that the resist uniformity is completely independent on the non-rounded shape of the sample. Using the described chuck and plate the stripes could be deposited over the whole surface and with a space between stripes edges and crystal edges < 100 μm . In order to collect all the generated carriers it is important that the strips extend up to the edges of the sample as much as possible.

4.2.4 Contact deposition

The development of a reproducible and high performance contact deposition technique has encountered some difficulties. The main problems are connected with CZT characteristics. CZT is fragile, especially near the edges, and a particular care is necessary especially with those techniques, like photolithography, that requires contact between the sample and the mask, with a consequent pressure on the sample. Moreover it's well known the poor adhesion of metals on the CZT surface. This limit cannot be overcome with a thermal annealing, as it's usually done, because of the change of CZT properties at temperatures higher then 100-150 °C. Every contact geometry can be transferred to the sample surface by means of photolithography (as previously discussed) or, for simple geometry, using mechanical masks. Mechanical masks allow only simple geometries and the resolution of the edges is quite poor with respect to other techniques and, for preparation of 3D detectors, cannot be used. Photolithography can instead be applied to any desired contact shape. In particular, after the photolithography process with a negative resist, sample surface is uncovered where illumination occurs (transparent parts of the mask) and covered by the hard resist in all other parts. The parts without resist are therefore ready for the deposition of the metal contacts or any other layer (for example alumina).

Gold electroless deposition

To deposit anodes and cathodes stripes (collecting electrodes) the electroless depositions was used. Electroless represents a very fast contact deposition technique and it does not require special equipment such as ultra-high vacuum. This technique works on the basis of chemical reactions between the sample surface and the metal solution as mentioned in previous chapter. In our case, for the deposition of gold, a standard aqueous solution of $AuCl_3$ (5%) was used. The typical deposited thickness that can be deposited is around 600 Angstrom. Beside the fact that electroless deposition is an extremely versatile technique that can be used with several metals and can be coupled with photolithography, it also shows advantages with respect to thermal evaporation like a better adhesion to CZT and a more reproducible electrical contact.

Gold contact deposition by thermal evaporation

Gold deposition on passivating layer (drift stripes only) by thermal evaporation was performed in a ultra-high vacuum chamber; samples are mounted in the chamber and then a primary vacuum is obtained using a zeolites pump (the average vacuum is 10^{-3} mbar). The secondary vacuum is achieved with a cryo-pump, at this stage the vacuum reaches 10^{-9} torr. The gold charge is positioned on a molybdenum melting pot and then evaporated by Joule effect. The vacuum chamber is equipped with a in-situ system for monitoring the deposited layer. For CZT samples a 800 Angstrom layer of gold is deposited.

4.2.5 Surfaces Passivation

The reduction of surface currents is a main concern in the detector fabrication. Several solutions have been proposed in the literature, most of them including the use of H_2O_2 as oxidizing agent. At IMEM we use a new technique to deposit thin film of alumina (Al_2O_3) at room temperatures (RT) on CZT surfaces.

Standard Passivation

For the realization of devices a solution of $NH_4F + H_2O_2$ (3%) was used for passivating the surface. The process is the simply immersion of the sample for 7 minutes inside the solution at room temperature. The reduction of leakage currents can be ascribed to the increase of the surface resistance as a consequence of the oxide formation. The oxide layer formed by NH_4F-based etching was studied by optical ellipsometry by using a variable angle spectroscopic

ellipsometer working in the range 200-1700 nm. The measured refractive index for the layer is compatible with that of an oxide resulting as a mixture of ZnO, TeO_2 and CdO (n=2.2 and n=2.5 at 1500 nm, respectively). The passivation procedure can be performed on the sample before or after the contact deposition. It has been tested that the oxidizing solution does not affects or removes the metal layers present on the CZT surface.

Alumina Layer

Despite its good transport properties, CZT requires special contact geometries in order to improve the energy resolution using the so called "single charge" techniques. Moreover this segmentation open also the possibility of making 2D and 3D imaging detectors. Nevertheless two main problems affect CZT detectors with patterned contacts:

- The resistivity of the surface is always smaller compared with the bulk resistivity ($> 10^{10}\Omega cm$). The noise associated with the surface currents may deteriorate the energy resolution of the detector. This also because the distance between electrodes is normally very small $(10 \div 100)\mu$m and the electrical resistance between electrodes may result to be low.

- In some devices (for example drift stripes detectors, in coplanar grid devices and in pixel detectors with steering grid) there is a voltage difference between different electrodes in order to collect all the charge only from the electrodes of interest (more positive the electrodes for collecting electrons). The voltage drop between electrodes can increase the noise associated with the current in a dramatic way.

The surface resistivity can be increased for example using an efficacy passivation technique. Unfortunately in some cases the standard passivation is not enough to decrease these currents. For this reason and in particular for the 3D detector project a novel approach was used. The idea was to deposit an additional insulating layer with resistivity higher than the native CZT oxide directly on the CZT material [74]. This idea is not new and it was already proposed in literature to overcame the problem of noise related to the steering grid in pixelated detectors. In 3D detectors (also in pixel detectors) there are always both collecting and non collecting electrodes at different potential on the anode surface of the detector. In order to reduce the leakage current between electrodes a thin layer of high-resistivity material can be deposit on the surface of the CZT between the crystal and the non-collecting electrodes. I. Jung proposed alumina as good material for these types of applications [74]. This because alumina has high

resistivity value and has a good chemical and mechanical stability. The main difference in this work in comparison with the work of Jung was the novel approach to deposit alumina on CZT. In particular a growth technique called Pulsed Electron Deposition (PED) was used.

4.2.6 PED technique

In thin film technology a lot of deposition methods have been studied and still used, also for industrial production of thin film-based devices. Vacuum deposition technique can be grouped in two main categories: Physical Vapor Deposition (PVD) and chemical vapor deposition (CVD). Among PVD processes there are also sputtering and evaporation. In physical vapor deposition (PVD) processes, the coating is deposited in vacuum by condensation from a flux of neutral or ionized atoms of material. These deposition processes require the use of very good vacuums system. The CVD process use some gaseous precursors that react directly on the substrate. The problems related to this technique are due to: reactant costs and toxicity and the low control of chemical, structural and morphologic homogeneity along the whole film. Pulsed Electron Deposition is a process in which a pulsed high power electron beam penetrates approximately 1 μm into the target. The result is a rapid evaporation of target material that generate a plasma. The non-equilibrium extraction of the target material (also called ablation process) facilitates stoichiometric composition of the plasma. Under optimum conditions, the target stoichiometry is thus preserved in the deposited films and this represents the main advantage of this technique (shown in Fig. 4.6b). In contrast to conventional technique as conventional e-beam evaporation, the main feature of the pulsed systems is the ability to generate a high power density of $\sim 10^8 W/cm^2$ at the target surface. As a result, thermodynamic properties of the target material such as the melting point and specific heat become unimportant for the evaporation process. This is particularly advantageous in the case of complex, multi-component materials. As in the case of Pulsed Laser Deposition (PLD), the Pulsed Electron Deposition (PED) technique provides a unique platform for depositing thin films (1 nm to 5 μm) of complex materials on a variety of technologically important substrates, with a unique strength of extending the range of materials and applications.

Another very important characteristic of PED deposition is that Al_2O_3 can be deposited also at room temperature. This characteristic is very important for two main reasons: i) as mentioned above CZT material is very sensitive to the temperature and normally it is better to operate at temperatures lower than 100 °C, ii) The properties of the photoresists (in particular adhesion and stability) are not altered if a room temperature process is used.

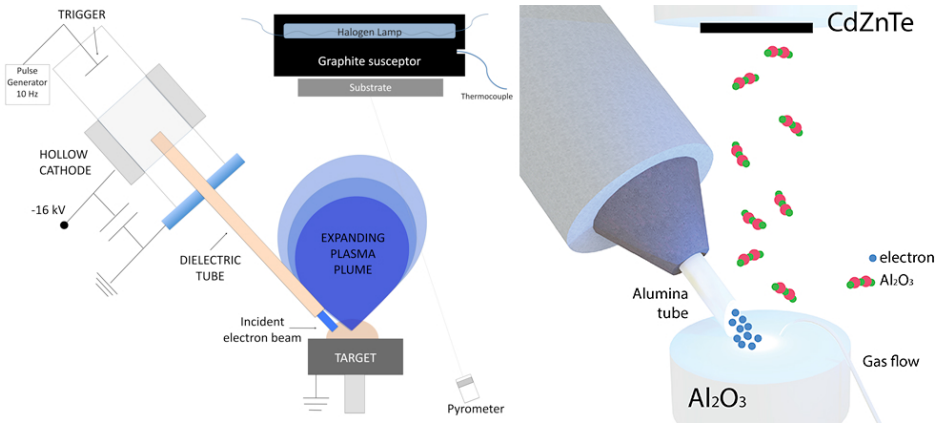

Figure 4.6: PED scheme (left), PED setup for Al_2O_3 deposition on CZT samples (right).

The fundamental steps of PED technique (shown in left part of Fig. 4.6 can be summarized as:

- The electron beam generation is initiated by a pulse of auxiliary low current gas discharge. The pulse is controlled by a trigger with a 10 Hz frequency.
- The plasma penetrates into the hollow cathode (gas pressure inside 1-3 Pa) that is connected to the plate of a low-inductance capacitor, to which a negative static potential (16 KV) is applied. The plasma excites emission from the hollow cathode surface.
- A ceramic tube plays the role of a channel ensuring directivity of the beam, providing the electric insulation, and protecting the cathode from contamination with the beam erosion products.

In IMEM-CNR institute the PED technique was developed for $CuIn_xGa_{(1-x)}Se_2$ (CIGS) based solar cells research.

4.2.7 Attachment Method and Bonding

Semi-automatic procedure to attach the detector to the alumina PCB and make the electrical bonding was developed during this project. This procedure consisted by different steps:

- First of all the detector was aligned to the PCB on a reference plane assumed to be perfectly planar.
- After that the detector was perfectly aligned with the pads of the PCB, this was possible using a digital microscope automatically moved.

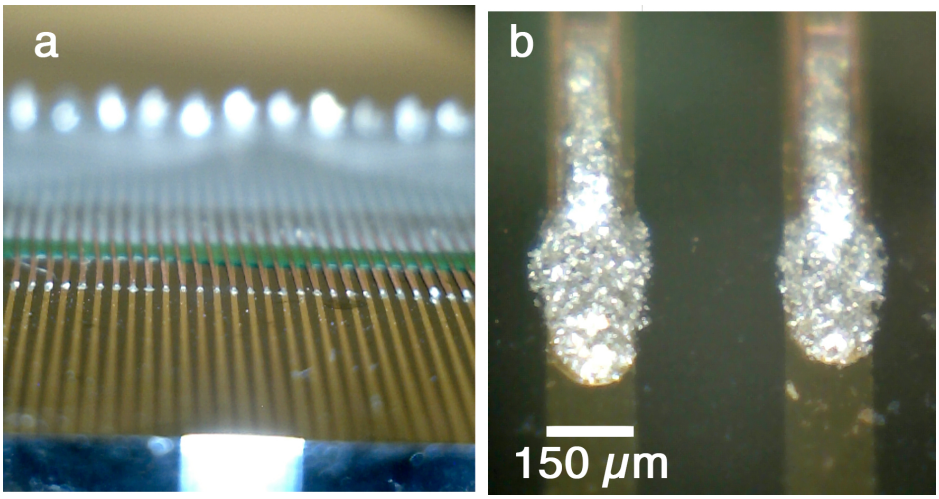

Figure 4.7: a) The copper comb bounded on detector stripes with epoxy glue, b) typical bondings made by the automatic machine.

- When the detector was aligned to the pads it was fixed to the PCB using space qualified high resistivity epoxy glue.
- A special copper comb was aligned with detector stripes and PCB pads and than soldered to the PCB pads (Fig. 4.7 a).
- In order to bond all the 49 anode and drift stripes a semi-automatic process was develop. A special copper comb was aligned to the PCB pads and the stripes of the detector. This copper comb was soldered on the PCB side with a special soldering paste. On the side of the detector the comb was connected using automatic machine that connected the comb to the stripes of the detector using a special glue (Fig. 4.7 b).
- The cathodes stripes were connected using copper wires soldered on PCB side and attached with conductive epoxy on the detector side (this procedure was carried out by manually controlling an especially developed tool)

In order to reduce the noise in the system and to increase the mechanical stability of the PCB in this project alumina PCBs (3 mm thick) were used. Alumina, in fact, guarantees a high rigidity to the PCB reducing the leakage currents between pads. Nevertheless all the soldering procedures are more complicated because of the highly thermal conductibility of the alumina. The main features of this process are: low operation temperature ($< 100°$C), high precision bonding (typical contact area 50μm x 50μm) and very good alignment between detector surface

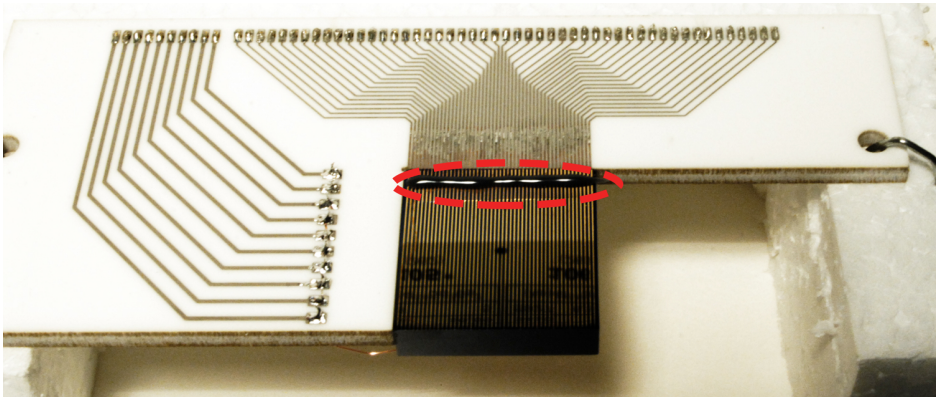

Figure 4.8: The completed detector plus PCB, the red circle indicates the extra epoxy glue for covering bonding on CZT.

and PCB surface. Moreover high stability electrical connections were achieved adding high resistivity epoxy glue on the bonding on CZT as shown in Fig. 4.8. This cover layer was fundamental for the stability of the either system.

4.3 Detector characterization

4.3.1 Resistivity measurements

In order to extrapolate the resistivity of the alumina and to generally test this passivation technique, a 100 nm Al_2O_3 (green layer on Fig. 4.9) was deposited by PED on standard passivated CZT sample (2 mm thickness) before processing the definitive prototypes.

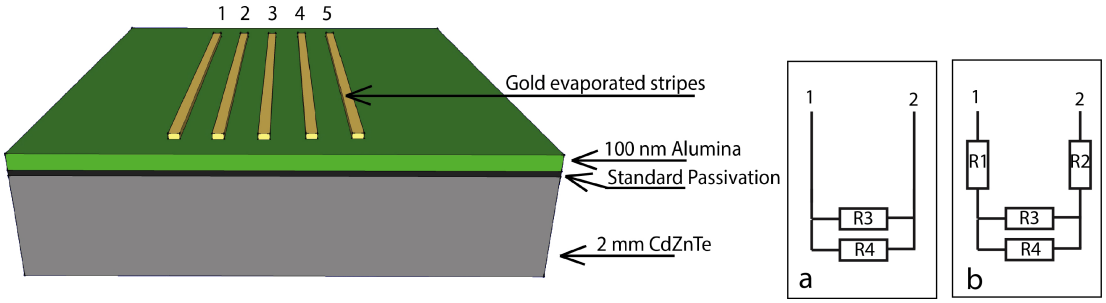

Figure 4.9: CZT detector with the alumina layer between gold stripes and passivated surface. On the right the equivalent electric circuit.

Five gold stripes (60 nm thickness) were evaporated on alumina layer, having 250 μm width, 15 mm length, and with 250 μm pitch. The CZT sample was passivated with the standard

procedure described in the previous section. Without alumina layer, the resistance between stripes in a normal passivated CZT detector depends on the values of R3 and R4 (Fig. 4.9 a). R3 is the resistance due to the surface and R4 is the bulk resistance. Being these two resistors in parallel,the lower resistance (R3) controls the current value. For this reason, the addition of the two resistors in series (R1 and R2 Fig. 4.9 b), due to the alumina layer can decrease the total current of the circuit.

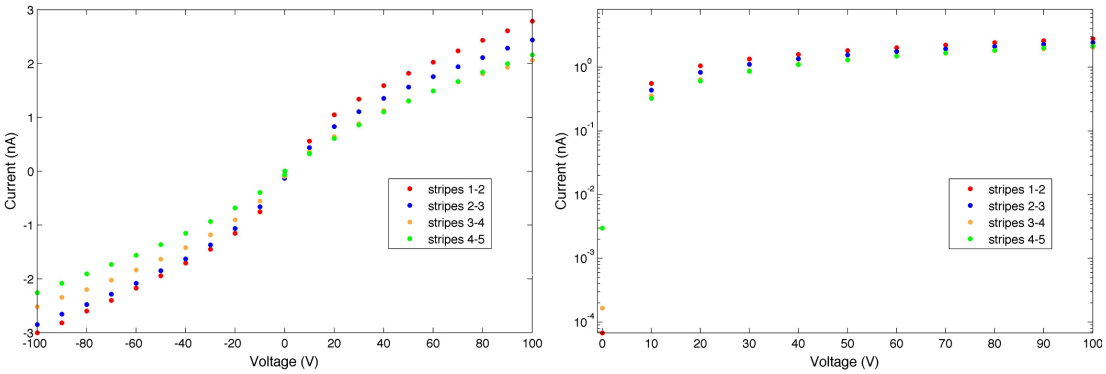

Figure 4.10: Linear (left) and semi-log (right) IV characteristic of the stripes of Fig. 4.9.

The IV characteristic between two adjacent stripes is shown in Fig. 4.10. The IV characteristics are the same for all the stripes and clearly confirm that the thickness and the resistivity of the alumina layer are almost uniform. Considering the geometrical parameters a resistivity in the order of $(5 \div 6) \cdot 10^{13} \Omega cm$ can be extracted in low voltage range.

Using this alumina extra layer the currents between stripes are comparable with the bulk current that normally are in the range $(5 \div 15)$ nA. As shown in Fig. 4.10 the gold-alumina contact has blocking characteristics, thus decreasing further the value of currents at high voltages. The Al_2O_3 layer deposited by PED shown other very interesting properties:

- The film show very good adhesion to CZT passivated surface.
- The layer was very uniform all over the surface. Thickness variations in the order of 5% on 20mm x 20mm area were measured with a standard profilometer.
- The quality of the layer was very good also for room temperature deposition.
- Evaporated gold contacts shows good adhesion on alumina layer (much strong adhesion than evaporated gold on CZT surface).

- PED deposition was compatible with the standard photolithography process. In particular the photoresist, after the Al_2O_3 deposition, was very easy to remove.

4.3.2 I-V measurements

The requirement for the allowable surface leakage current between two 20 mm long strips with 0.15 mm width and 0.25 mm gap was <4 nA at applied -100 V on one strip and measuring return current on the near strip at T=22 °C.

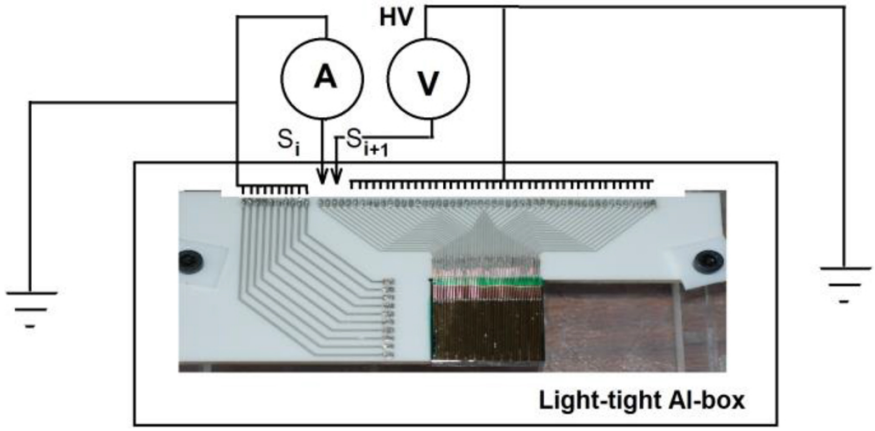

Figure 4.11: Surface leakage current measurement setup.

For the bulk leakage current between cathode strips and one 20 mm long strips with 0.15 mm width and 0.25 mm gap requirement was < 2 nA at applied -100 V, always at T=22 °C. All IV measurements were done at IMEM institute, then repeated and verified at DTU Space.
Fig. 4.11 shows the surface leakage current measurement setup. For the surface leakage current measurements, all strips (including cathode strips) were held at ground potential except S_i and S_{i+1}. Surface leakage current were recorded between S_i and S_{i+1} with HV (-100 V). The measurement was repeated for all strips by shifting S_i and S_{i+1} to the right.
Fig. 4.12 shows bulk leakage current measurement setup diagram. For the bulk leakage current measurements, cathode strips were biased with HV (typ. -100 V or -500 V). Bulk current between cathode and S_i was recorded while the other strips help at ground potential. The measurement was repeated for all strips by shifting S_i to the next strip.
Tab. 4.1 and 4.2 shows the measured leakage current data for the DTU2 detector measured during ESRF synchrotron experiments. As it can be see from that tables, very good results were obtained. About surface leakage current, DTU2 shows very low currents between adjacent

Strip Nr.	**1-2**	**2-3**	**3-4**	**4-5**	**5-6**	**6-7**	**7-8**	**8-9**	**9-10**	**10-11**
Current (nA).	1.10	1.03	0.86	0.86	0.86	1.07	0.83	0.86	0.84	1.10
Strip Nr.	**11-12**	**12-13**	**13-14**	**14-15**	**15-16**	**16-17**	**17-18**	**18-19**	**19-20**	**20-21**
Current (nA).	0.87	0.85	0.89	1.16	0.97	1.09	1.50	1.15	3.28	1.52
Strip Nr.	**21-22**	**22-23**	**23-24**	**24-25**	**25-26**	**26-27**	**27-28**	**28-29**	**29-30**	**30-31**
Current (nA).	16.80	1.73	1.60	1.08	1.31	1.46	1.11	1.16	4.67	1.42
Strip Nr.	**31-32**	**32-33**	**33-34**	**34-35**	**35-36**	**36-37**	**37-38**	**38-39**	**39-40**	**40-41**
Current (nA).	1.18	1.63	1.30	1.53	1.30	1.44	1.28	1.55	1.22	1.26
Strip Nr.	**41-42**	**42-43**	**43-44**	**44-45**	**45-46**	**46-47**	**47-48**	**48-49**		
Current (nA).	1.45	1.62	1.31	1.51	1.68	3.98	3.62	3.27		

Table 4.1: Surface leakage current measurement of Detector measured at ESRF (HV = -100 V, T=22 °C).

Strip Nr.	**1**	**2**	**3**	**4**	**5**	**6**	**7**	**8**	**9**	**10**
Current (nA).	0.62	0.39	0.17	0.09	0.09	0.09	0.10	0.09	0.09	0.08
Strip Nr.	**11**	**12**	**13**	**14**	**15**	**16**	**17**	**18**	**19**	**20**
Current (nA).	0.10	0.08	0.06	0.06	0.09	0.06	0.09	0.10	0.13	0.09
Strip Nr.	**21**	**22**	**23**	**24**	**25**	**26**	**27**	**28**	**29**	**30**
Current (nA).	0.11	0.13	0.18	0.13	0.15	0.13	0.22	0.13	0.10	0.10
Strip Nr.	**31**	**32**	**33**	**34**	**35**	**36**	**37**	**38**	**39**	**40**
Current (nA).	0.13	0.11	0.16	0.17	4.45	0.12	0.13	0.11	0.12	0.12
Strip Nr.	**41**	**42**	**43**	**44**	**45**	**46**	**47**	**48**	**49**	
Current (nA).	0.09	0.07	0.07	0.04	0.04	0.05	0.05	0.05	0.05	

Table 4.2: Bulk leakage current measurement of detector measured at ESRF (HV = -100 V, T=22 °C).

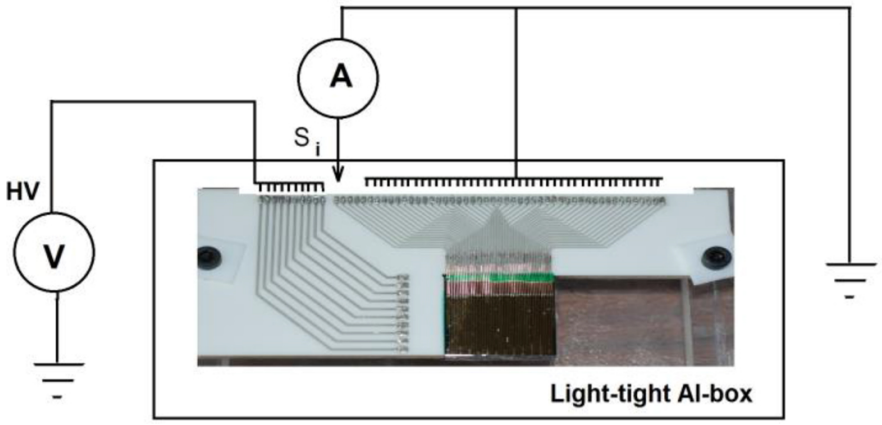

Figure 4.12: Bulk leakage current measurement setup.

stripes, except for strip Nr. 21-22 that was 16.80 nA. The only other out-requirement value is for strip Nr. 29-30 that with its 4.67 nA at -100 V exceeding the target value (4 nA) for only a small amount.

About bulk leakage current measurements, DTU2 completely fulfill requirement of 2nA currents at -100 V of applied bias, except for stripe 35 that behave 4.45 nA.

4.3.3 ESRF synchrotron experiments

Due to the limited amount of time available at the European Synchrotron Radiation Facility (ESRF) characterizations were performed only for one detector (DTU2) of four. Experiments were carried out at ESRF at the beam line 15A. This beam line provides an high intensity beam in a wide energy range (100-600 keV). The aim of this type of experimental investigations on CZT drift strips detector was to demonstrate that CZT drift strips detector combines a good energy resolution with 3D sensing capabilities of this detector configuration. Fig. 4.13 shows a real picture of the CZT drift strips detector used for the ESRF synchrotron beam test experiment. It is worth repeating that CZT drift strips detector realized on spectroscopic grade material from Redlen with size of 20 x 20 x 5 mm^3. The strip pitch was 400 μm with 150 μm of strip width and consist of the Au layer as described above.

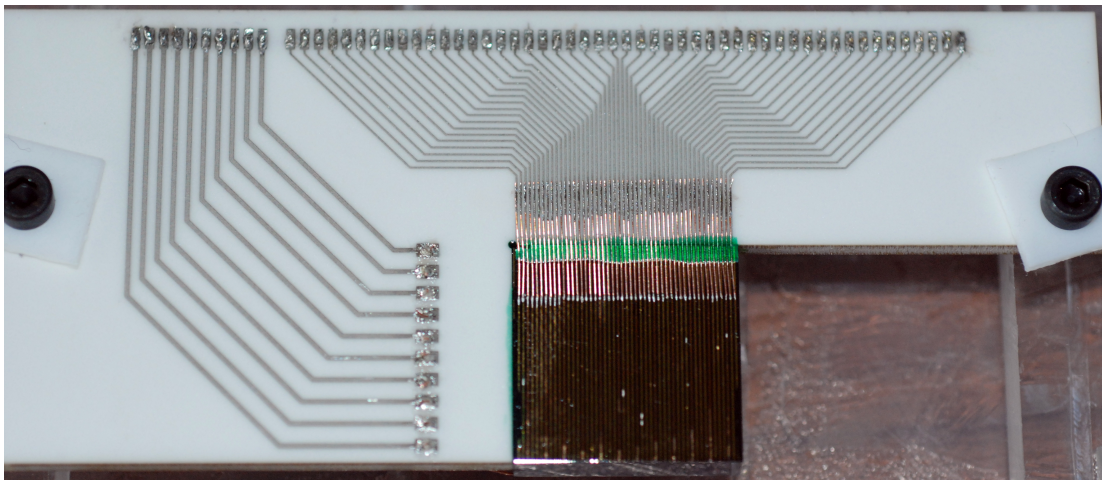

Figure 4.13: Real picture of 3D CZT drift strips detector mounted on alumina PCB used for ESRF beam test.

Detector calibration

Detector system was energy calibrated at DTU Space using Am-241, Co-57, Ba-133 and Cs-137 radiation sources. Calibration was then repeated and verified using Ba-133 at ESRF. Fig. 4.14 shows the Ba133 spectra recorded by the detector setup at DTU Space and at ESRF. Fig. 4.15

shows the detector calibration data used for the data analysis. The gain and offset for the cathode and drift strips were all adjusted for the experiment.

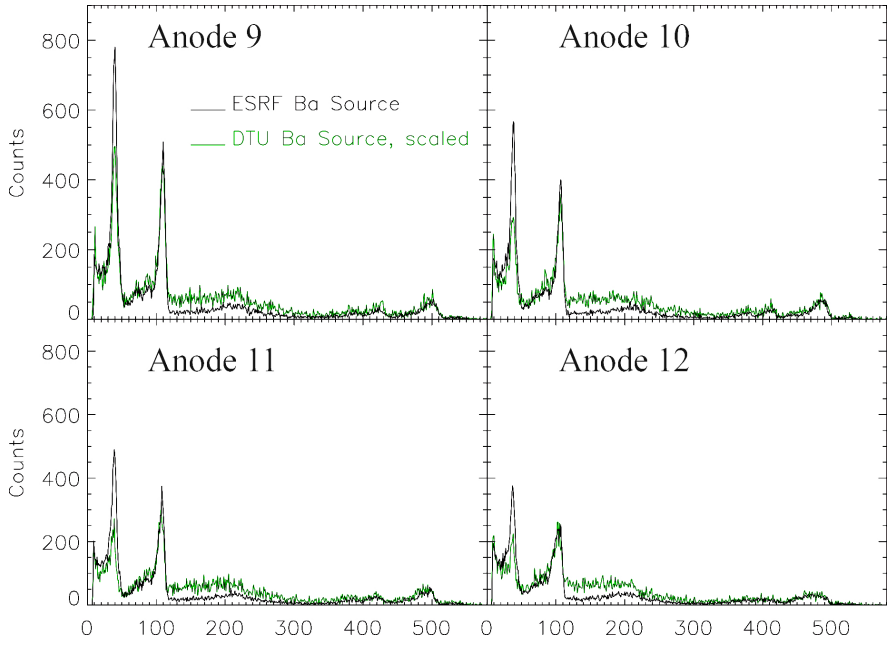

Figure 4.14: Ba-133 spectra recorded by the detector at DTU Space lab (green) and at ESRF (black).

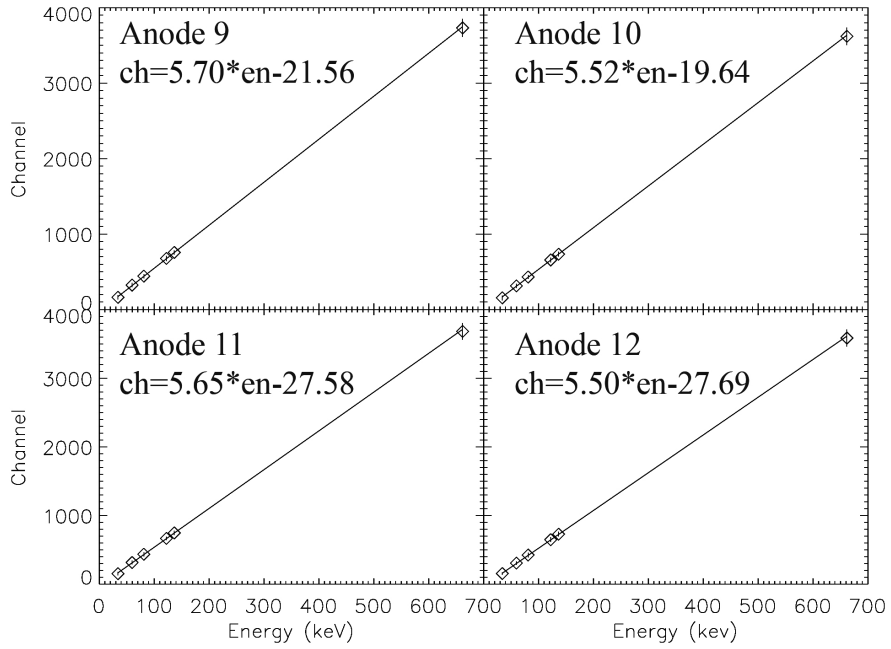

Figure 4.15: Energy calibration of the detector system.

ID15A beam profile

The beam at ESRF was shaped by using two different tungsten collimator in the optical hutch, in front of the white beam and the second in the experimental hutch, after the monochromator. Fig. 4.16 shows the plot of the beam profile measurements in the x-direction (top) and y-direction (bottom) respectively, carried out at ID15 beam line at ESRF during beam size preparation. The beam was adjusted and shaped to be about 50 μm x 50 μm size for the selected energies of 150 keV, 300 keV, 400 keV and 580 keV.

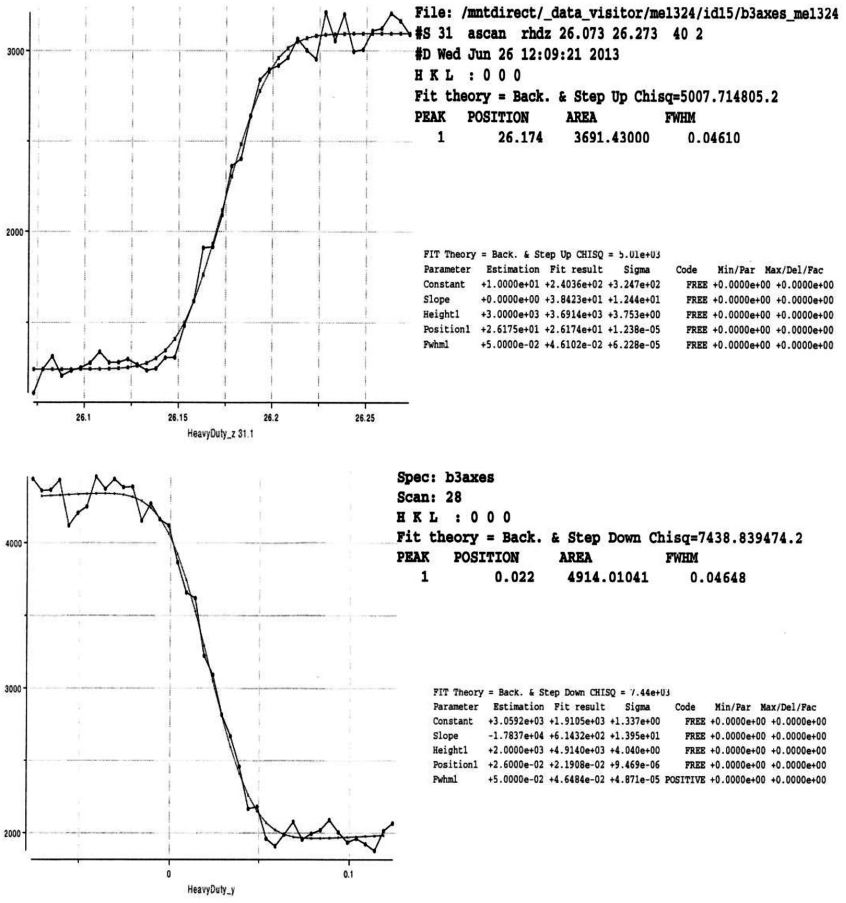

Figure 4.16: ESRF ID15 beam profile in x-direction (top) and in y-direction (bottom).

2D Scans

A number of 2D scans were performed on the selected detector on plane x-y and z-y. Before each scan, it was necessary to perform the beam preparation including changing beam energy, intensity adjustment and beam start position check. The last check is necessary since changing

the beam energy can result in position shift for the beam. All these preparation work toke an average amount of time of about 2 hours. At high energies (>500 keV, the intensity drops from 10^3 to 10^2 photons (for 50 μm square beam) so recording time for high energies were adjusted to record at least 10^3 events for each beam position at high energies. The readout strips and the segmented cathode were connected to eV5093 preamplifiers. CZT drift strips detector with its PCB, the preamplifier and the passive components PCB are enclosed in a special box, placed onto the xyz translational stage as depict in Fig 4.17. This system is capable of moving the detector box in 3 directions, controlled by a DTU developed program. Its main function is to record detector data for 2D scan in an autonomous way based on user-defined parameters. The scan software contains a main program, which interfaces and controls the data acquisition (DAQ) software and the xyz-stage controllers.

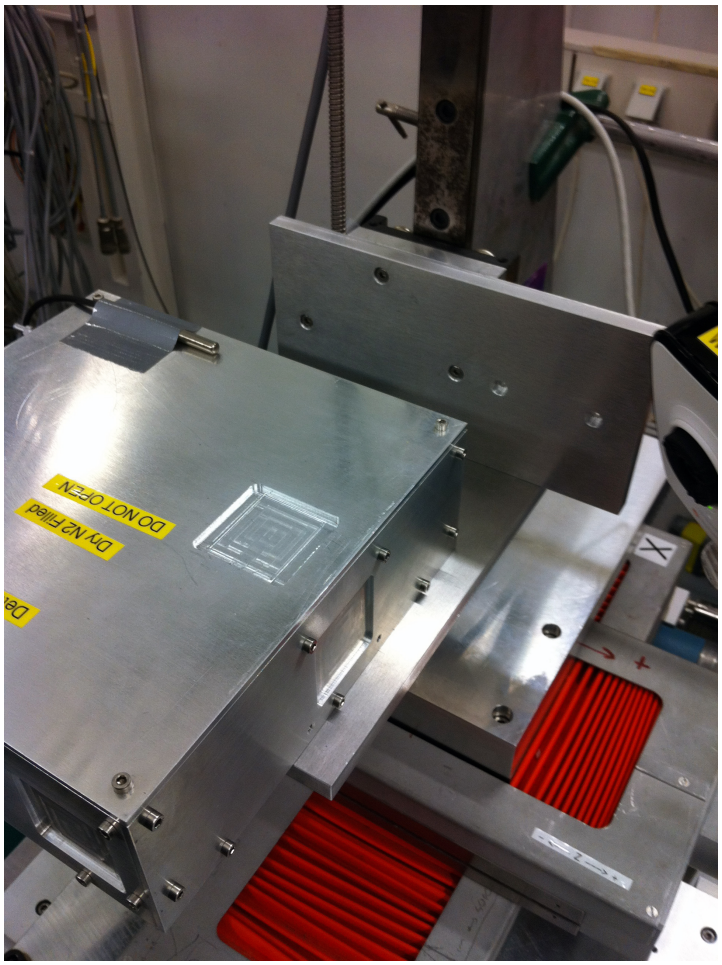

Figure 4.17: Detector box mounted on mechanical translational xyz-stage at ESRF.

Each scans was performed in the "side illumination" configuration, the so-called PTF (Photon Transverse Field). Photons enter the detector perpendicular to its side; this mode has the advantage that photons can be absorbed in the full length of the detector (20 mm) while the created charge at most will drift through the thickness of the detector (5mm). Therefore this detector illumination mode will provide high efficiency, preserving the excellent spectroscopic performances obtained for the CZT drift strip detectors. At each energy all scans were repeated on the same scan area which cover only 4 of the 12 drift cells (Fig. 4.18). Signals from 4 anode strips, the relative non collecting grids and 8 (of 10) cathode strips were collected for each events, resulting in about 15 thousands recorded events for each position of the scan.

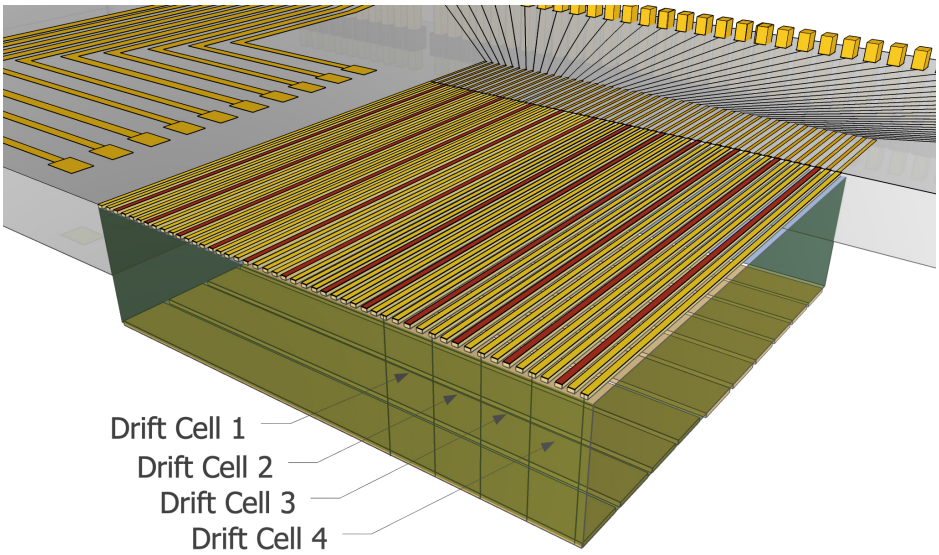

Figure 4.18: The four drift cells used for all the measurements at ESRF.

x-y scans illumination in PTF configuration

In the first experiment, the synchrotron beam impinged on the lateral surface of the detector, with anode strips perpendicular to it as represented in Fig. 4.19. It's worth repeating that all the scans for different energies were repeated on the same scan area which cover only 4 of the 12 drift cells, on x-y plane with 25 steps of 200 μm along x direction and 28 steps of 200 μm along y direction, covering 5.0 mm x 5.6 mm scan area (Tab. 4.3).

One 2D scan approximately takes 25 x 28 x 8 seconds (6 seconds recording time + 2 seconds overhead time) for a total time of about 2 hours. Overhead time is the fixed time for the software developed by DTU to save the recorded data in a file and move the beam to a new

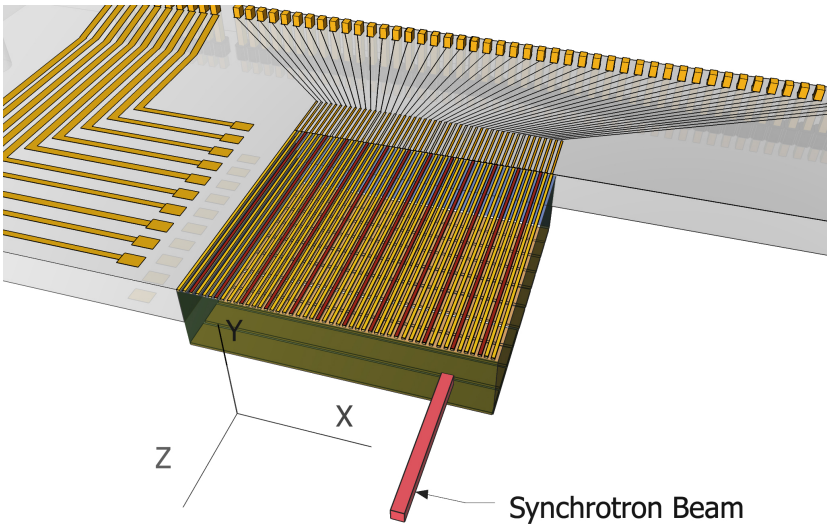

Figure 4.19: Geometry of the first scanning experiment (x-y scans).

Energy (keV)	dx (mm)	N. x steps	dy (mm)	N. y steps	2D scan area (mm x mm)	Integration time for each beam position (sec) + overhead time (sec)
150	0.2	25	0.2	28	5.0 x 5.6	6+2
300	0.2	25	0.2	28	5.0 x 5.6	6+2
400	0.2	25	0.2	28	5.0 x 5.6	6+2
580	0.2	25	0.2	28	5.0 x 5.6	10+2

Table 4.3: 2D scans performed on x-y plane.

position and start the recording again.

z-y scans illumination in PTF configuration

In the second experiment, the synchrotron beam impinged on the lateral surface of the detector, with cathode strips perpendicular to it as represented in Fig. 4.20. All the scan for different energies were repeated on the same scan area in the z-y plane with 40 steps of 600 μm along z direction and 5 steps of 800 μm along y direction, totally covering 24 mm x 4 mm scan area (Tab. 4.4).

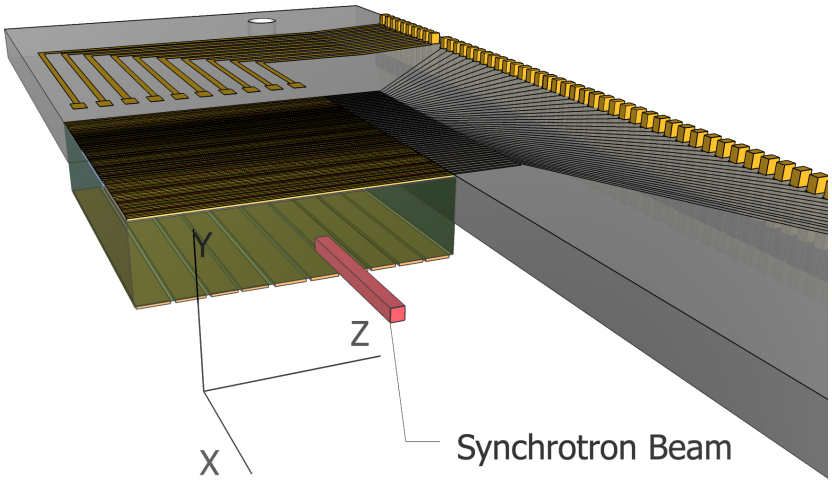

Figure 4.20: Geometry of the second scanning experiment (z-y scans).

Energy (keV)	dz (mm)	N. z steps	dy (mm)	N. y steps	2D scan area (mm x mm)	Integration time for each beam position (sec) + overhead time (sec)
150	0.6	40	0.8	5	24.0 x 4.0	8+2
300	0.6	40	0.8	5	24.0 x 4.0	8+2
400	0.6	40	0.8	5	24.0 x 4.0	8+2
580	0.6	40	0.8	5	24.0 x 4.0	8+2

Table 4.4: 2D scans performed on z-y plane.

Energy scans

In order to investigate position resolution function of energy in 3D, we have performed energy scans with beam illumination on same position on the detector in x-y plane and z-x plane. Beam energies used for both planes are:150 keV, 200 keV, 225 keV, 250 keV, 275 keV, 300 keV, 350 keV, 400 keV, 450 keV, 500 keV, 550 keV and 600 keV.

4.4 Results and discussion

In the following sections 3D position capabilities, spectral performance and amount of charge sharing will be achieved from the ESRF acquired data.

4.4.1 3D position capabilities

It's worth repeating that not only the drift strip readout technique provide an improved energy resolution for CZT detectors, but it also yields information about the interaction depth of the detected photon.

Resolution along Y direction

First of all the problem of the resolution along Y direction will be considered. This parameter can be determined using the set of data from the first experiment (2D scan data in x-y plane). The so-called depth information (depth sensing) in the Y-direction can be derived in this case, at a given energy, for each event, from the ratio:

$$Y_{pos} = \frac{\sum_{n=1}^{8} SCn}{SAm} \tag{4.1}$$

where SCn is the signal related to n-cathode and SAm is the signal relative to the anode that showed a signal different from zero so, in other terms, the signal from the drift cell in which the event occur. In the case that more than one anode shows a signal different from zero (charge sharing effects), the signal from the two quantities are summed. It will be discussed in section 4.4.3. The quantity Y_{pos} is almost linearly dependent on the photon interaction depth, with a value close to unit for interaction close to the cathode and a value close to zero for interaction near the strip electrodes. Real position in Y-direction can be calculated using $Y_{pos} \cdot L_d$ where L_d is the detector thickness.

For each beam position, the centroid of the distribution of the events (Gaussian) represents the position of the beam along the Y-axis and FWHM of the Gaussian represents the resolution in the Y-direction (some example will be show in Fig. [4.31-4.34]).

However, measured position resolution is affected by three main sources, hence for evaluating the effective detector resolution we must take into accounts all these effects. The first one is the finite beam size of the synchrotron beam which had a diameter of 50 μm. The second is the electronic noise associated with the signal acquisition (cathode and anode signals). The last is the dimension of the electronic cloud generated by the absorption event, that is dominant at high energies.

The electronic noise $Y_{pos,noise}$ associated with the determination of Y_{pos} , can be written as [71]:

$$Y_{pos,noise} = \frac{1}{SAm} \sqrt{\sum_{n=1}^{8} SCn_{noise}^2 + SAm_{noise}^2 Y_{pos}^2} \tag{4.2}$$

where SCn_{noise} is the electronic noise of the n-cathode (FWHM) and SAm_{noise} is the electronic noise of the m-anode. The electronic chains of all the 4 anodes and of all the 8 cathodes employed during experiments at ESRF were checked with an external pulser. The FWHM for the anodes is in the range $(3.4 \div 3.7)$ keV. Similarly, for the cathodes the FWHM is in the range $(3.7 \div 3.9)$ keV. The beam size is fixed for all beam energies and it is 50 μm x 50 μm. Its contribution as noise source to the position resolution is negligible compared to the contribution from readout electronic noise and the dimension of the electronic cloud generated by the absorption event. This last contribution as noise source to the position resolution is dominant at high energies and it increases with photon energy. All the above mentioned sources of noise contribute to determine the actual position resolution.

The value Y_{pos} linearly depends on the beam position along the Y-axis as shown in Fig. 4.21, with a value close to unity for interactions close to cathode and a value close to zero for interaction near strip electrodes. This demonstrates that the value of Y_{pos} can be used for the absolute determination of the beam position along the Y axis.

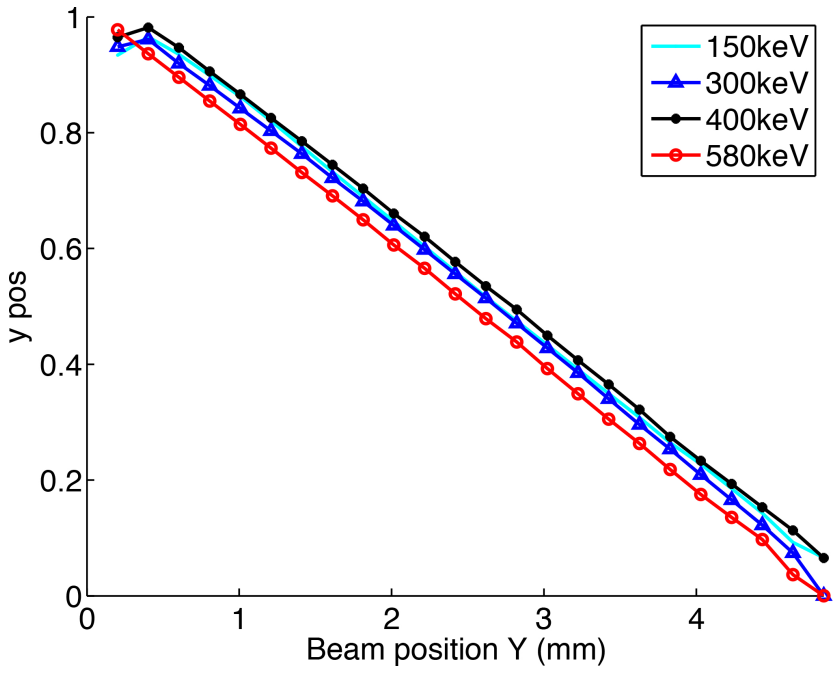

Figure 4.21: The measured and derived Y_{pos} value versus depth for energies 150 keV, 300 keV, 400 keV, and 580 keV.

In this plot, data points shown for 2D scan point in the anode A11 section at x=10, y=0...24 for all energies. Measured beam positions are the peak centroids after the fitting procedures

described above. There is an offset shift between data for different energies caused by the different scan start positions (around ± 0.2 mm).

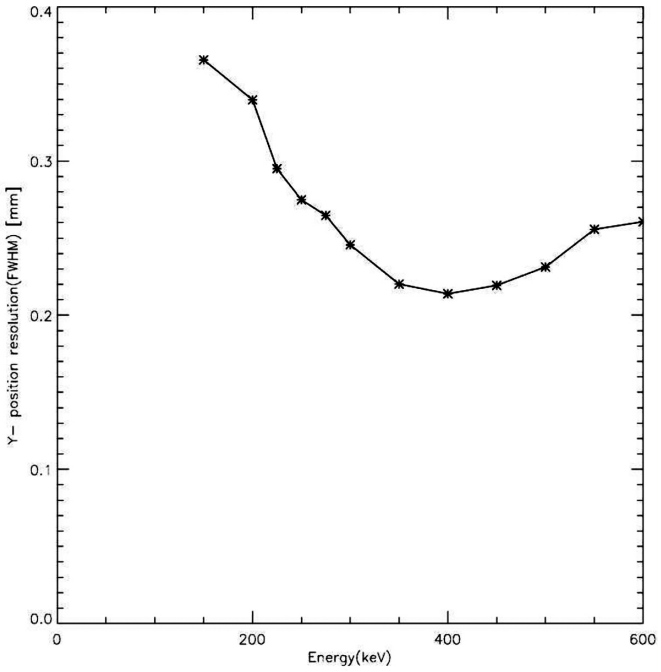

Figure 4.22: Position resolution along the Y direction as function of energy.

As pointed above, the measured position resolution in the Y direction is dependent and affected by the finite beam size, electronic noise and the dimension of the electronic cloud generated by the absorption event. Fig. 4.22 shows position resolution in Y-direction as function of energy. The plot indicates a strong photon energy dependency for the position resolution and it has a minimum at ∼0.2 mm FWHM at 400 keV. At higher energies (> 500 keV), the detector position resolution decreases with increase of the dimension of the electronic cloud generated in the detector material. The photoelectron absorption length increases together with its kinetic energy thus it creates larger electron cloud size. At low energies, position determination is mainly dominated by signals uncorrelated electronic noises, as described in Eq. 4.2. Therefore, a better electronic noise performance in the system will provide an improved position resolution at low energies. On the contrary, only the material properties can determine the photoelectron absorption length and the resolution at high energies.

Resolution along X direction

Also in the case of resolution determination in X direction, data from the first experiment (x-y scans, illumination in PTF configuration) were exploited. For each scanning point, at fixed energy, the drift cell of interest must be determined. If the signal of one anode is high and the signal of the other anodes is zero than the interaction is located in the drift cell of the nonzero anode. Details on the position determination in X-direction are object of the patent **EP13194445** deposited by DTU Space and cannot be revealed yet.

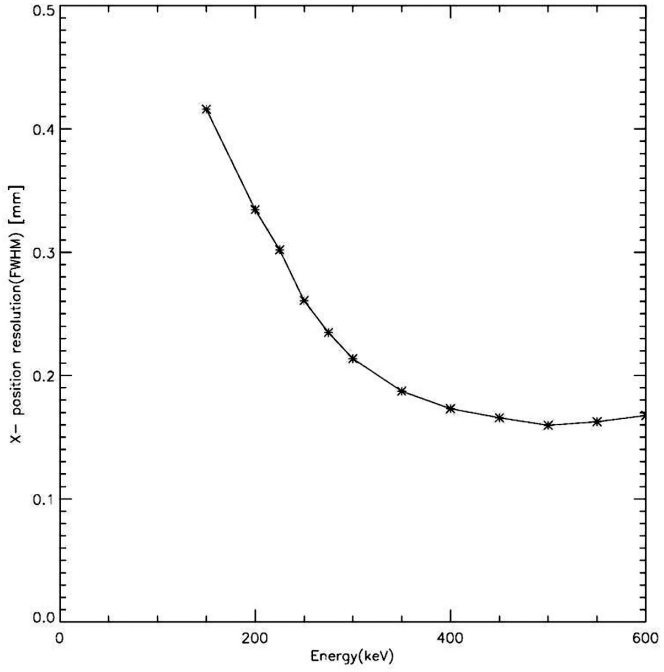

Figure 4.23: Position resolution along the X direction as function of energy.

Fig. 4.23 shows position resolution in X-direction as function of energy. The plot indicates a strong photon energy dependency for position resolution: the minimum is ∼0.2 mm FWHM at 500 keV.

This is demonstrated in this project using ESRF 400 keV x-y scanning data (anode 11 area, shown in Fig. 4.25). A look-up table was created from correlating measured beam positions (fit results as averaged positions from X and Y direction) and actual beam positions (step of 0.2mm in both directions). Corrected positions (X_c,Y_c) are obtained from this look-up table using bi-linear interpolation. The look-up table applied on the ESRF 400 keV x-y scan result is shown in Fig. 4.25. Here, data from only each second beam positions are shown (0.4 mm

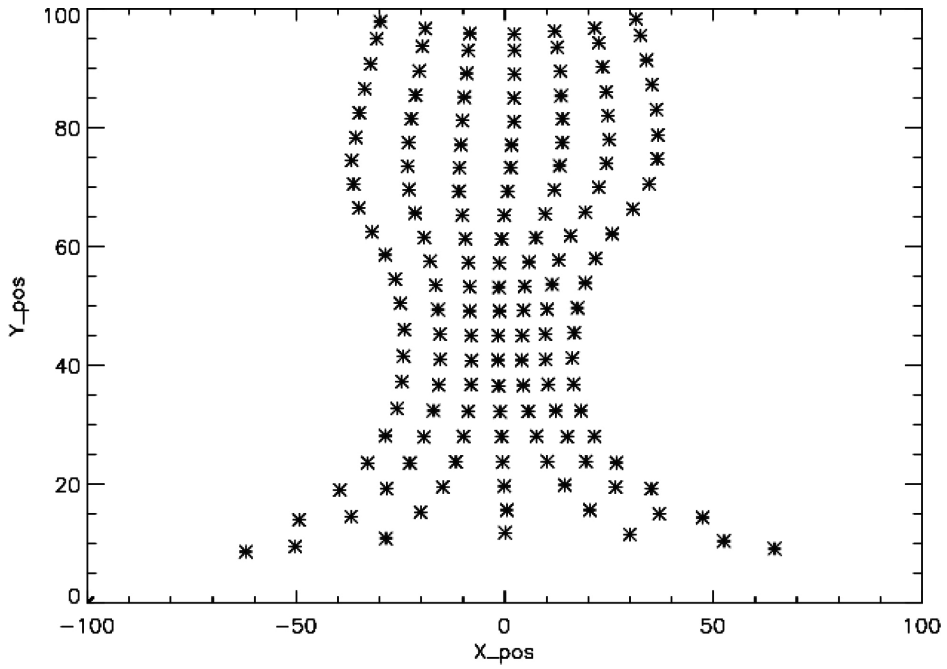

Figure 4.24: 400 keV beam positions for x-y scanning (anode 11 area). Y_{pos} measured values are in the range of (0.0 to 1.0)*100. X_{pos} measured values are in the range of 100*(-1.0 to 1.0).

For XY positions, the measured beam position linearly depends on the real beam position along the Y-direction but for the X-direction, the measured beam position dependency is non-linear and depends on the Y-position. This is shown in Fig. 4.24 for 400 keV beam positions for x-y scanning (same anode 11 area). In that plot Y_{pos} measured values are in the range of (0.0 to 1.0)*100 and equivalent 0 to 4.5 mm (0 at the anode side and 4.5 mm at the cathode side). X_{pos} measured values are in the range of 100*(-1.0 to 1.0); and it must be noted that range (-80 to 80) is equivalent to anode pitch W_{pitch} =1.6 mm. It is possible to calibrate and perform position correction for the detector using 2D scan data. This requires performing a 2D scan with fine collimated beam and fine steps in both direction.

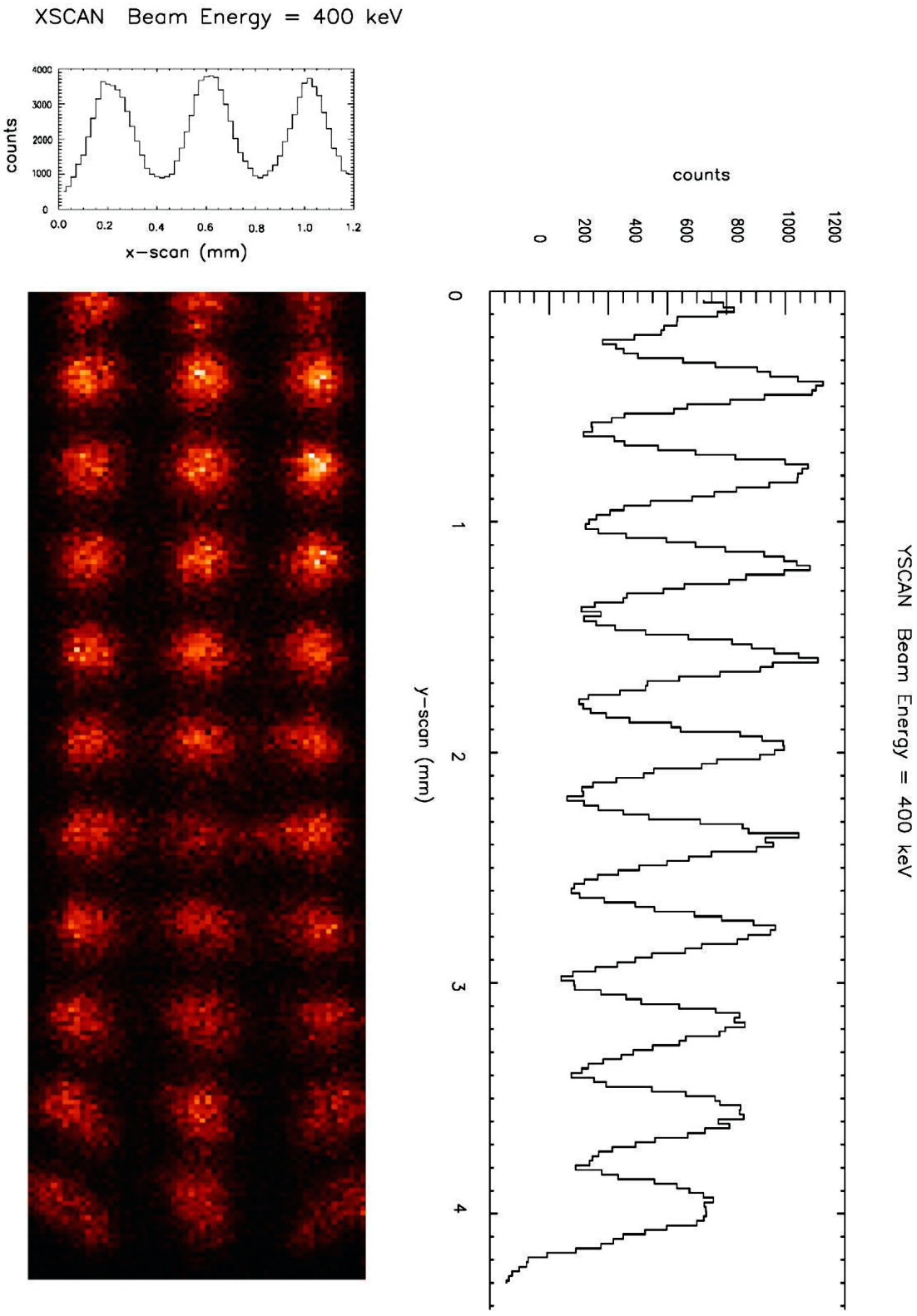

Figure 4.25: 400 keV x-y scanning corrected positions.

distance between beam spots in both directions). Beam is resolved very well with 0.2 mm FWHM in both directions.

Resolution along Z direction

In order to obtain the resolution in the Z direction, 2D scan data in the z-y plane from the second experiment were exploited. For each scanning points at fixed energy, and for every photon interaction, the signals induced on the 8 cathodes are used for finding the centroid position as Z_{pos}.

$$Z_{pos} = \frac{\sum_{n=1}^{8} n \cdot SCn}{\sum_{n=1}^{8} SCn} \tag{4.3}$$

where SCn is again the cathode strip signals. The histogram of the obtained maxima for all the events recorded at a fixed beam position fitted again with a Gaussian. The width of the obtained Gaussian is the resolution in the Z direction.

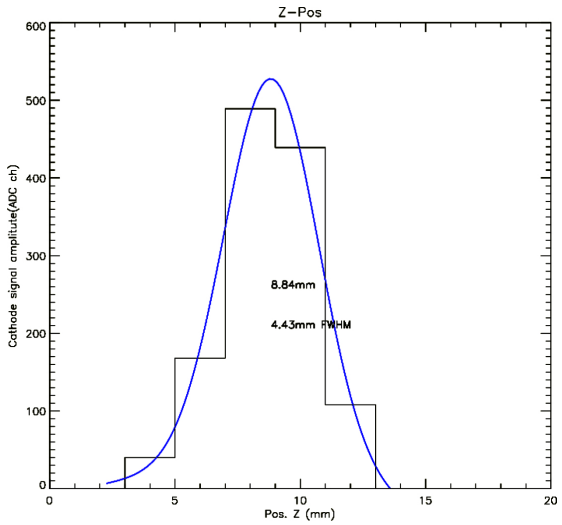

Figure 4.26: Signal recorded by 8 cathodes in a single event, together with the Gaussian fitting.

The Z resolution of the detector can be studied for different positions in the detector and for different energies. After data processing the position resolution in Z direction is obtained. As an example, the signal recorded by 8 cathodes, in a single photon event, is reported in Fig. 4.26, together with the total Gaussian fitting. An average position resolution around 0.6 mm FWHM is measured for $(200 \div 600)$ keV energy range, which is $\sim 1/3$ of the cathode strip pitch. The calculated value of Z linearly depends on the beam position along Z axis as shown in Fig. 4.27. This demonstrates that the value of Z as determined by the described procedure

can be used for the absolute determination of the beam position along Z axis. Fig. 4.28 shows the detectors measured position resolution as function of energy in Z-direction.

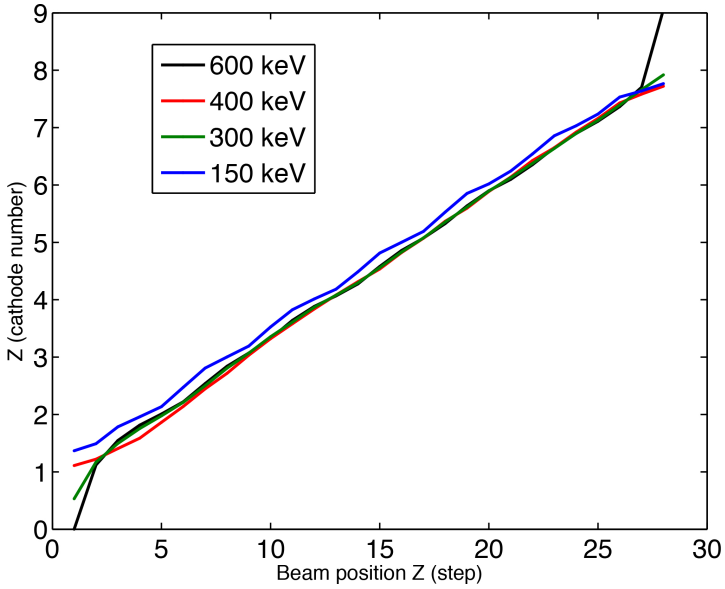

Figure 4.27: The measured beam position dependence of the actual beam position in the Z direction for a given value of Y position (2.0 mm from the cathode side) for all energies.

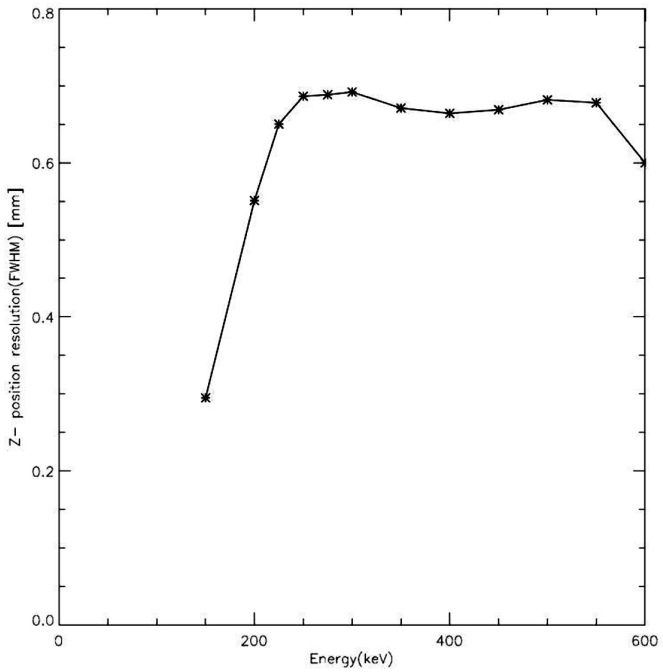

Figure 4.28: Position resolution along the Z direction.

4.4.2 Spectral performance

The ESRF monochromatized synchrotron beam is not 100% mono-energetic. For this reason, spectra of the beam were recorded for selected energies for the 2D scans by using a germanium detector (see Fig. 4.29). In particular at high energy (600 keV), the energy spreading is not negligible ($\sim$ 7 keV FWHM) and affects the energy resolution of the 3DCZT detector. As above mentioned a second effect that must be taken into account in order to correctly evaluate the detector energy resolution is the electronic noise of the readout chains. In order to determine electronic noise, detector is tested with an external pulser. The electronic chains of all the 4 anodes employed during experiments at ESRF were checked. Table 4.5 shows achievable energy

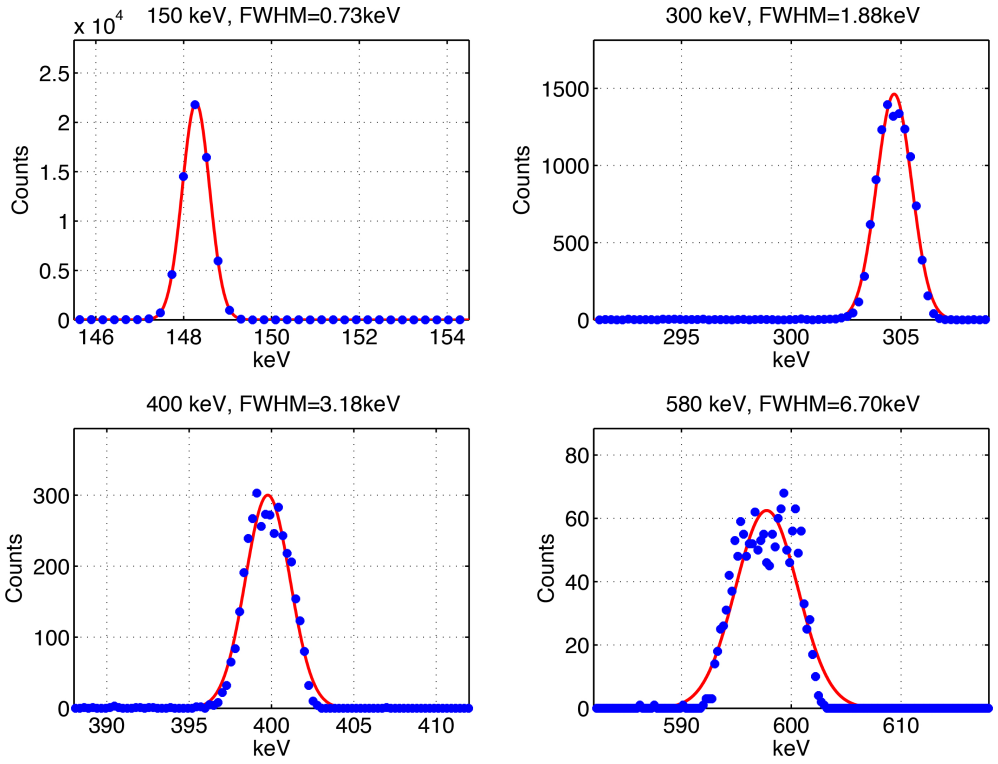

Figure 4.29: Energy profile of the synchrotron beam at different energies, as measured by a germanium detector at ESRF.

resolution for the detector calculated using the following equation :

$$FWHM_{det} = \sqrt{FWHM_{tot}^2 - FWHM_{sync}^2 - FWHM_{el}^2} \tag{4.4}$$

where $FWHM_{tot}$ is the measured energy resolution (uncorrected), $FWHM_{sync}$ the synchrotron beam energy spreading, $FWHM_{el}$ the electronic noise and finally $FWHM_{det}$ the actual achievable detector energy resolution. The result show that $\sim$ 1.5% FWHM at 600 keV can easily

Energy (keV)	$FWHM_{tot}$ (keV)	$FWHM_{sync}$ (keV)	$FWHM_{el}$ (keV)	$FWHM_{det}$ (keV)
150	4.20	0.73	3.67	1.91
300	6.10	1.88	3.67	4.50
400	7.40	3.18	3.67	5.58
580	10.8	6.70	3.67	7.63

Table 4.5: The detector (Anode 10) measured energy resolutions.

be achieved and also improved, if position calibration table (including energy calibration) is adopted.

4.4.3 Charge sharing effect

The so-called "shared events" may occur when the beam is in the region between two adjacent anode strips where more than one anode shows a signal different from zero. In this case, a reconstruction procedure is processed. The anode with maximum signal is reconstructed with the sum of the anode signals involved in the event and the signals for all the other anodes are set to 0. The data analysis will provide statistics for the shared events. It is possible to calculate the percentage of these events where more than one anode shares the detector signal. The shared events are identified and reconstructed in the data analysis for each energy and 2D scans in x-y plane. Results for shared events statistics are shown as 2D map.
In Fig. 4.30 we show the maps of charge sharing for the x-y scanning experiments at different energies. For each point it is given the percentage of events that gave an appreciable signal on more than one anode. The maps clearly show that charge sharing effect is limited to regions between adjacent drift cells. The results show that shared events statistic is around $(5 \div 10)\%$ for energies $(150 \div 600)$ keV. The energy resolution gets slightly worse for reconstructed shared events due to the sum of the signals with their uncorrelated noises.

Combined position sensing capabilities and energy determination

After an interaction of photon within the CZT detector, time coincident signals from all electrodes were recorded. Analyzing the data will provide energy, time and 3D position information for each event. 3D position information will be determined:

- **Y-direction:** ratio between anode signal and sum of all coincident cathode signals will provide the interaction position in y-direction.

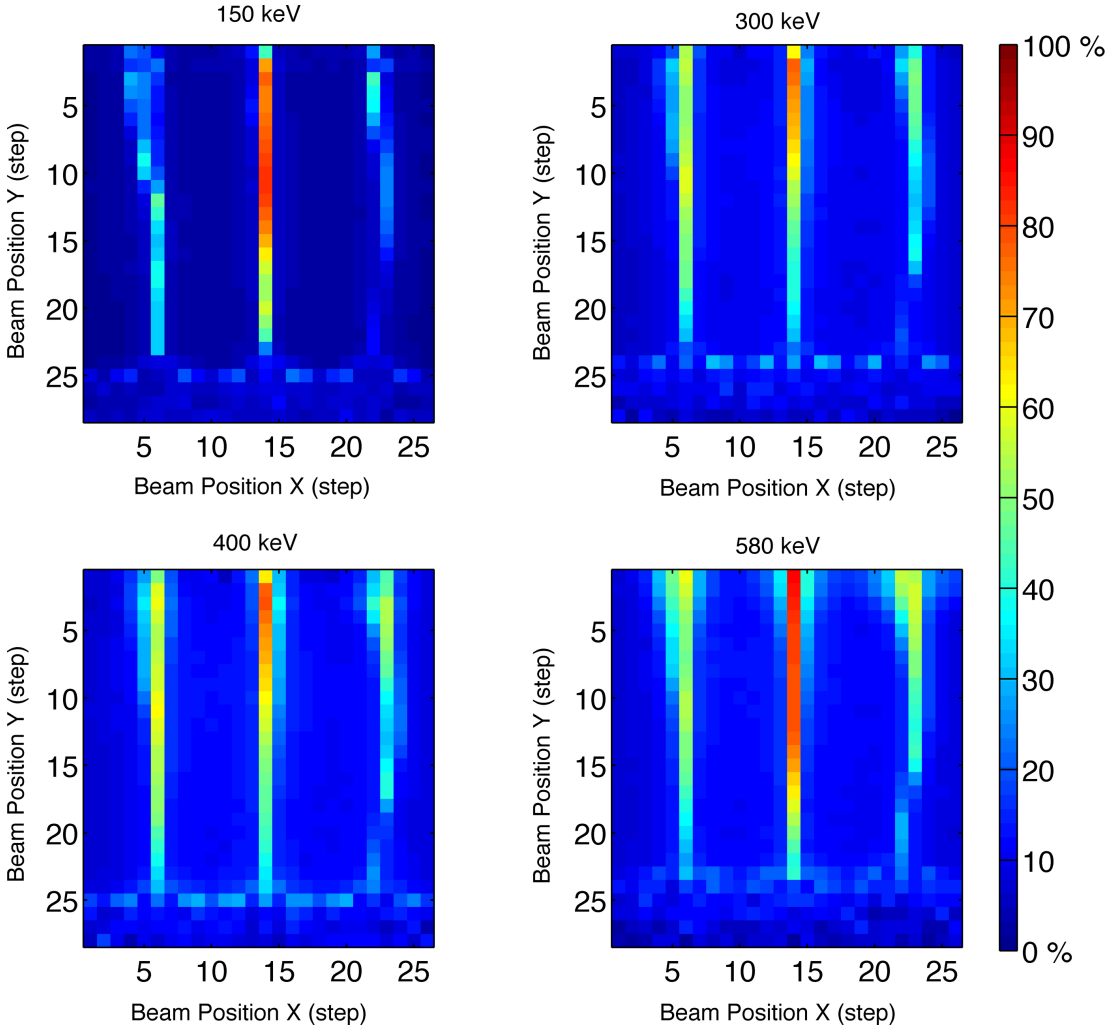

Figure 4.30: Maps of charge sharing for the X-Y scanning experiments at different energies. For each point it is given the percentage of events that gave an appreciable signal on more than one anode.

- **X-direction:** triggered anode signal will provide the interaction position in x-direction and signal ratio between drift strip signals of the left side and right side of the triggered anode will provide the fine position.
- **Z-direction:** coincident signal amplitudes from 8 cathode strips will provide the interaction position in z-direction.

Fig. [4.31-4.34] shows an example using above described procedure for x=10 and y=8 of 2D scans data for beam energies of 150, 300, 400 and 580 keV respectively. Plots show demonstration of 2D position capability of the detector when illuminated with the ID15A beam. Lower right plots show the spectral performance of the detector for different energies. Upper left plots show 2D image of the D15A beam (50 μm x 50 μm).

Upper right plots show histograms of the measured Y_{pos} values. Fitting this peak with Gaussian provides the measured beam position and the beam width as the peak centroid and its FWHM, respectively in Y-direction. Lower left plots show histograms of the measured X_{pos} values. Again here, we fit the peak with Gaussian and get the X-position and its FWHM. Each scan and for each beam position, this procedure is applied for all ESRF data.

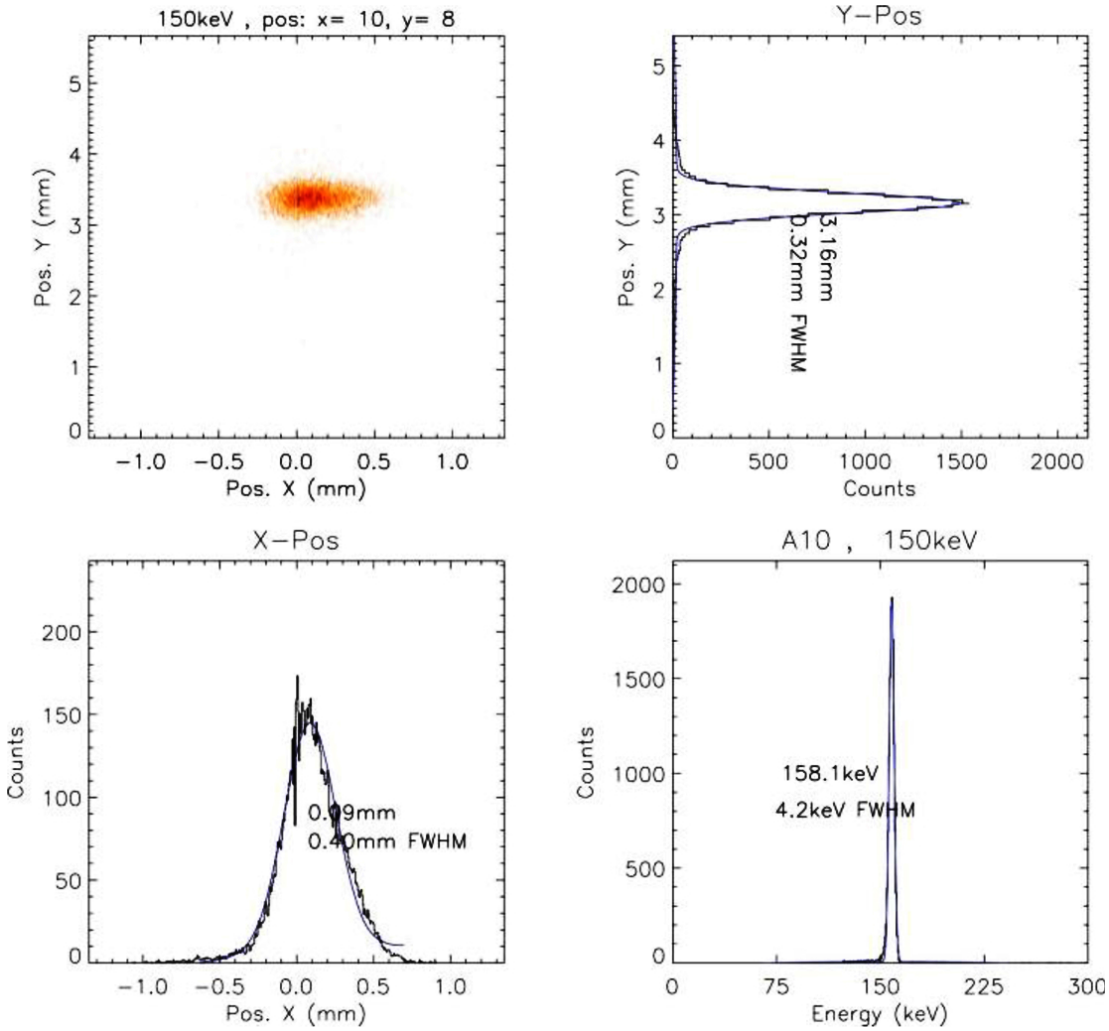

Figure 4.31: Result for x=10 and y=8 of 2D scans data for 150 keV beam energy.

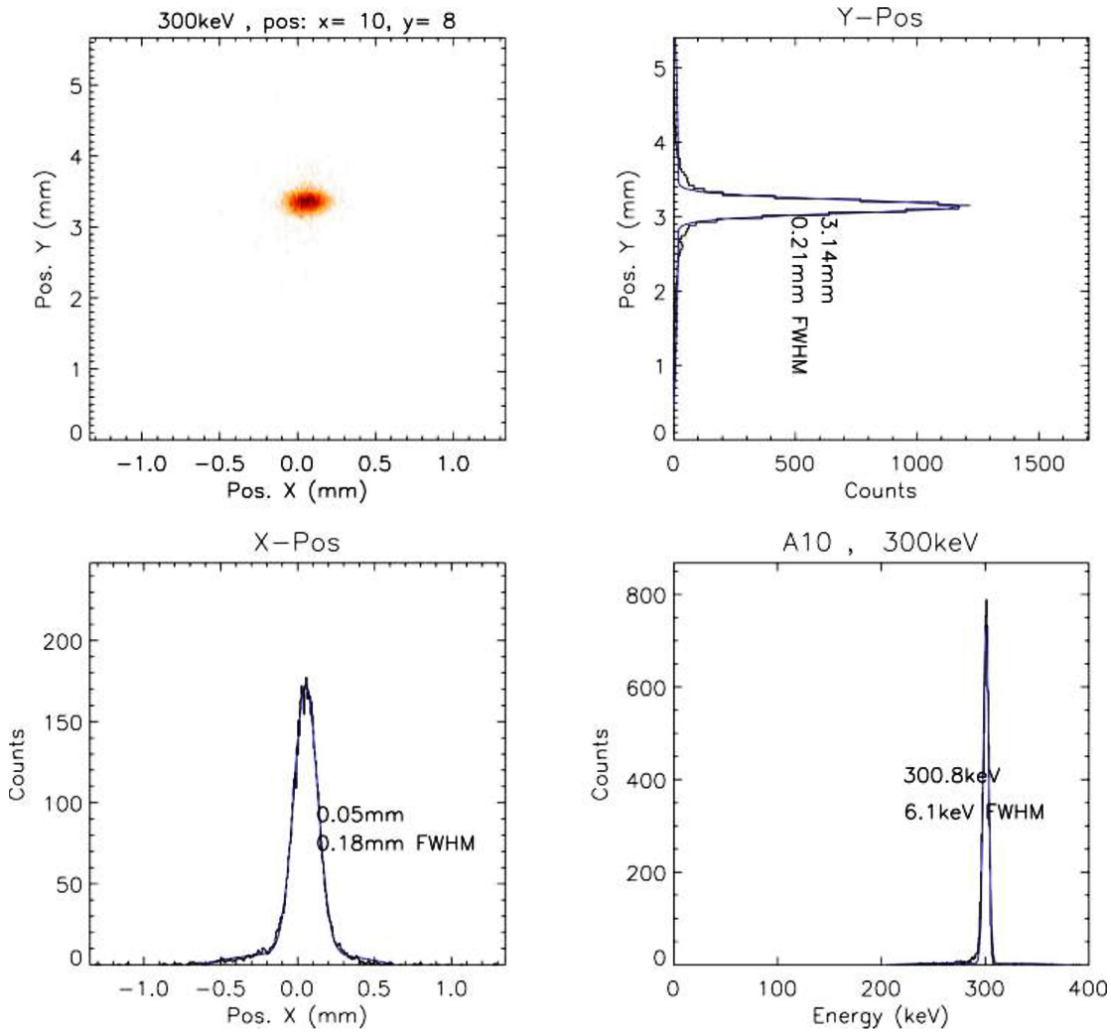

Figure 4.32: Result for x=10 and y=8 of 2D scans data for 300 keV beam energy.

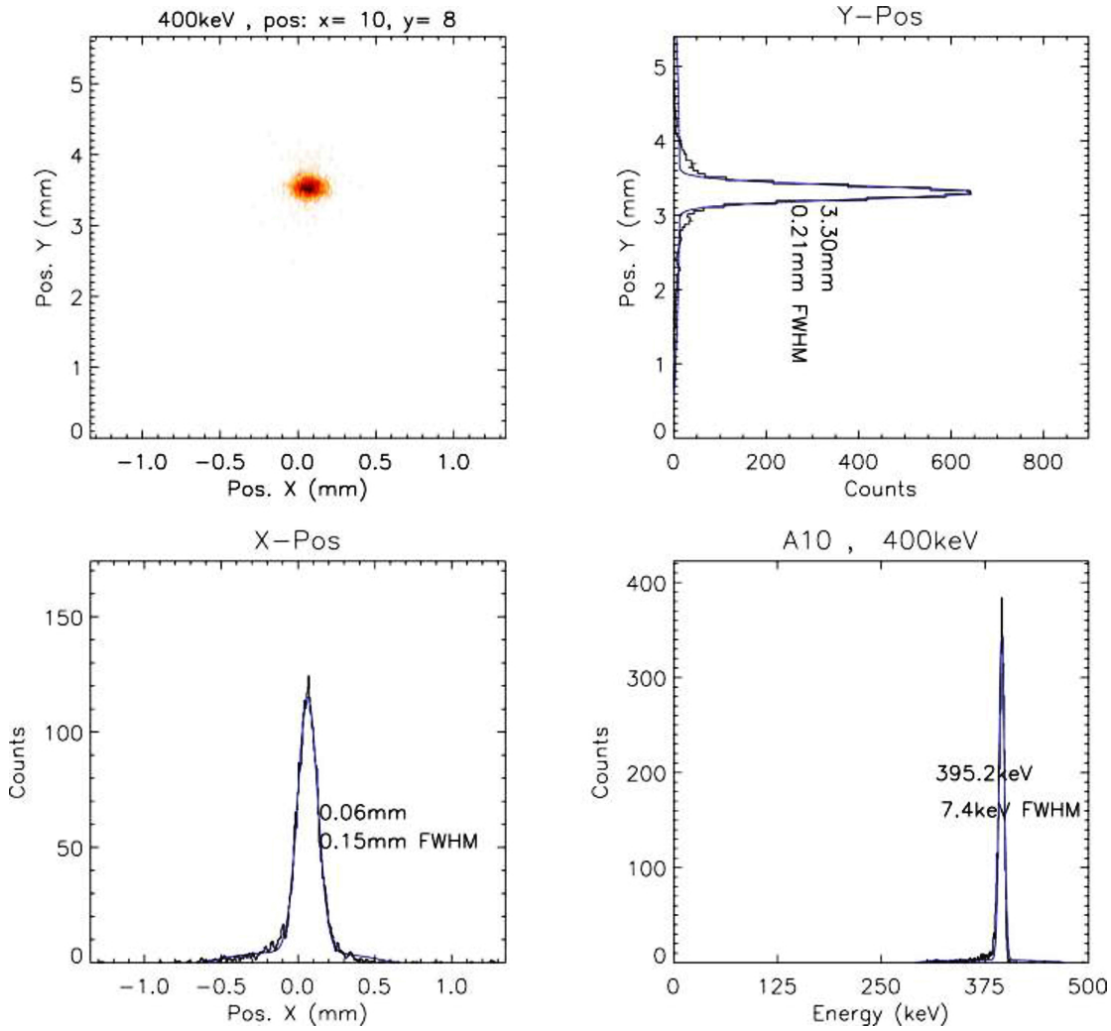

Figure 4.33: Result for x=10 and y=8 of 2D scans data for 400 keV beam energy.

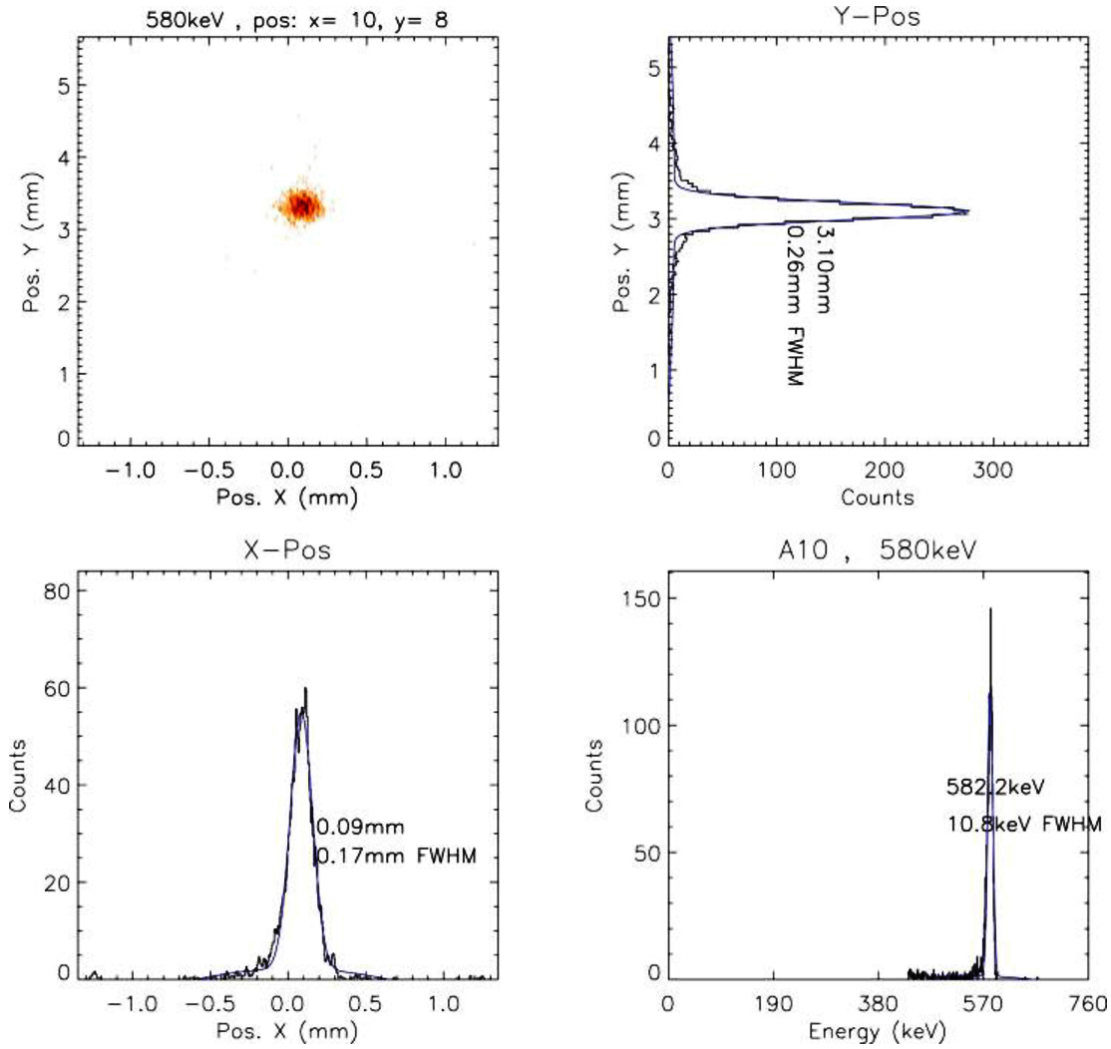

Figure 4.34: Result for x=10 and y=8 of 2D scans data for 580 keV beam energy.

4.5 Conclusion

3D position capability of the prototype detector has been demonstrated for X, Y and Z direction. Summary is shown in Table 4.6 for the X, Y, Z position resolution achieved by interpolation method. The result show that detector position resolution is mainly dominated by electronic

	Energy resolution	**Position resolution**		
Beam Energy (keV)	Energy resolution FWHM (keV)	x-direction (μm)	y-direction (μm)	z-direction (μm)
150	1.91	420	380	300
300	4.50	210	240	700
400	5.58	180	210	660
580	7.63	170	260	600

Table 4.6: Summary of the measured position resolution in 3D.

noise of the readout chains at low energies (<200 keV). That means better position resolution can be achieved by improving the noise performance of the readout electronics.

The measured detector spectral performance showed that the energy resolution is mainly dominated by energy spreading of the synchrotron beam. As discussed before the monochromatized synchrotron beam is not 100% mono-energetic and, at high energies (>400 keV), the energy spreading is not negligible (∼7 keV FWHM) affecting the energy resolution of the 3DCZT detector. A second effect is the electronic noise of the readout chains. The measured and achievable energy resolution of the detector is also shown in Table 4.6 . These performance can be further improved by calibration using position information with known energies.

As we can see about charge sharing, the effect is limited into regions between two adjacent drift cells. Electron charge cloud from such events in the region collected by two anodes. Shared event rate increases with increasing energy since high energies create larger electron clouds. In this case, a reconstruction procedure is processed. The shared event rate is around $(5 \div 7)\%$ at 150 keV and $(10 \div 12)\%$ at 580 keV.

Summary

Three dimensional mapping of tellurium inclusions in CdZnTe crystals

In the first part of the thesis a setup for the determination of the inclusion distribution in 3D was described. The proposed method can be implemented on standard transmission optical microscopes. Inclusions down to 1 μm can be detected and evaluated. The vertical resolution of the system is controlled by the numerical aperture of the employed objective and can be decreased to 9 μm. Thanks to a proper collection of images and use of patented algorithm for image reconstruction, it is possible to obtain a fully 3D reconstruction of the inclusion distribution, so that the position and the dimension are identified for each inclusion. Using this system, it is possible to study in much better detail important features of the inclusion distribution that can be locally correlated with material properties.

Tellurium inclusions and charge collection in CZT X and Gamma ray detectors

A set of IMEM grown CZT samples was studied in collaboration with Brookhaven National Laboratory. Several high resolution techniques were used, leading to complementary results in the characterization of the well known defects affecting the material. Te inclusions were identified using IR microscopy. The entire thickness of a sample was scanned and a collapsed image, containing information on the whole sample depth, was acquired on the entire area of the sample. X-ray response map were performed using a 24 keV synchrotron X-ray beam and a raster scan resolution down to 20 μm, on a large number of samples. The response map showed high uniformity of the response, with a fluctuation of about 2% in the device charge collection efficiency. Tellurium precipitates located in the IR images fully correlate with detector's deterioration of spectroscopic X-ray response. A correlation was also found between the spatial position of the inclusions in the detector thickness and the local effect on charge collection. Results of this study shows that defects close to the cathode widely affect the local gamma response when the 24 keV beam was used. At this energy, and for CZT material, the

penetration of the photons is about 100 μm; it suggest that for more energetic photons defects positioned deeper in the crystal become more important.

Luminescence properties of CZT crystals around tellurium inclusions

By means of tellurium inclusion 3D reconstruction instrumentation it was possible to prepare samples having large tellurium inclusions close to the surface. In this way, the modification of the luminescence properties of a CdZnTe sample in the presence of Te inclusions was studied. PL maps showed a strong enhancement of mid-gap emission band in the volume of the sample surrounding the inclusions. The origin of this emission band can be ascribed to the dislocation network surrounding the inclusion or to the presence of large density of point defects such as tellurium anti-sites. However, whatever the defect responsible for this emission, mid-gap levels act typically as lifetime killers for carriers. Thus, the shown results indicate that the degradation of detector properties induced by inclusions could be attributed to the recombination properties of defects surrounding them.

Inclusion density reduction in CZT crystals by pulsed laser irradiation

In this section a new approach to reduce tellurium inclusion density was proposed. Results shows that tellurium inclusions can really thermo-diffuse and dissolve in the presence of Nd:YAG laser irradiation. That effect is driven by the strong absorption of the light by Te inclusions and calculation of amount of energy transferred to the system is compatible with the proposed diffusion mechanism. Even if it was not possible to obtain large inclusion thermo-diffusion, previsions showed that by using laser pulses of longer duration (about 100 ns) also large tellurium inclusions can diffuse and dissolve without damaging the sample surface.

Electroless gold contact deposition on CZT detectors by scanning pipette technique

Scanning pipette technique was proposed for the deposition of gold contacts on CZT crystals. Deposition of patterned contacts with electroless method without using photolithography procedures was demonstrated: large area squared and circle contacts, micro-dots, pixels, micro-stripes, whose dimensions are compatible with the ones required by typical devices were successfully deposited. Alumina pipettes can be advantageously employed because inert to acid solution, mechanical stable, and enable the formation of a proper meniscus between the pipette and the sample surface. PVC pipette can also be adopted, although in the case of alumina one, pipettes with nozzle diameter down to few microns are available on the market (the same is not true for PVC pipettes).

Obtained electrical characteristic of deposited electrodes was optimal for realization of X-ray detectors. X-ray detector response was measured showing good spectroscopic characteristics.

Moreover, detectors with contacts deposited by the scanning pipette technique show at least the same energy resolution and charge collection efficiency of detectors with standard electroless gold contacts.

The scanning pipette technique showed to be versatile and can be used also for deposition of others metals by using proper metal precursor solution.

3D CZT Detectors

3D position capability, good spectral resolution and quite low charge sharing effect was achieved for the "DTU2" 3D CZT sample characterized at ESRF synchrotron beam facilities.

Position resolution of about 200 μm for both X and Y position direction was achieved. About Z direction the obtained resolution was about 600 μm. For each position directions measured resolution was less than physical "pixel size" of detector. However results show that detector position resolution is mainly dominated by electronic noise of the readout chains at low energies (<200 keV). That means better position resolution can be achieved by improving the noise performance of the readout electronics.

Measured detector spectral performance showed that the energy resolution is mainly dominated by energy spreading of the synchrotron beam. Monochromatized synchrotron beam is not 100% mono-energetic and, at high energies (>400 keV), the energy spreading is not negligible ($\sim$7 keV FWHM) affecting the energy resolution of the 3DCZT detector. A second effect is the electronic noise of the readout chains

Results show that charge sharing effect is limited into regions between two adjacent drift cells. Electron charge cloud from such events in the region collected by two anodes. Shared event rate increases with increasing energy since high energies create larger electron clouds. Measured shared event rate is around $(5 \div 7)$% at 150 keV and $(10 \div 12)$% at 580 keV.

Future Plans

In the last three years, my work on radiation detection concerned several topics: radiation detectors preparation, material characterization and instrumentation development. In particular, during this time, I developed many skills CZT device preparation. Moreover, in collaboration with Giacomo Benassi, I developed a process for the realization of 3D high performance CZT based detectors. In the world few other research centres have this technology for fabricating such type of detectors. We also realized, during 3D detectors project, that also few companies

in the world can make these high performance custom 3D detectors. Therefore, driven by the results obtained in the frame of this project, on January 9 2014 we started, in collaboration with other colleagues of IMEM-CNR, a company for CZT detector realization called "due2lab s.r.l.". Several companies have already shown their interest in our company and in our CZT detector technology. This represents a personal goal but also a recognition of the quality of my PhD work.

Publications

Some of the results of this work have been published in different papers and conference proceedings as shown in the list of publications at the beginning of the thesis.

Bibliography

[1] S. Del Sordo et al. Progress in the development of cdte and cdznte semiconductor radiation detectors for astrophysical and medical applications. *Sensors*, 9:3491–3526, 2009.

[2] J. M. Boone and A. E. Chavez. Comparison of x-ray cross sections for diagnostic and therapeutic medical physics. *Med. Phys.*, 23:1997–2005, 1996.

[3] S. Ramo. Currents induced by electron motion. *Proceedings of the IRE*, 27:584–585, 1939.

[4] J.D. Jackson. *Classical Electrodynamics, 2rd Ed.* Wiley: New York, NY, USA, 1999.

[5] K. Hecht and Z. Zum. Zum mechanismus des lichtelektrischen primarstromes in isolierenden kristallen. *Z. Physik*, 77:235–245, 1932.

[6] R. Devanathan et al. Signal variance in gamma-ray detectors-a review. *Nucl. Instrum. Meth. in Phys. Res. A*, 86:637–649, 2006.

[7] A. Owens and A. Peacock. Compound semiconductor radiation detectors. *Nucl. Instrum. Meth. in Phys. Res. A*, 531:18–37, 2004.

[8] A.G. Kozorezov et al. Resolution degradation of semiconductor detectors due to carrier trapping. *Nucl. Instrum. Meth. in Phys. Res. A*, 546:209–212, 2005.

[9] R.B. James et al. $Cd_{1-x}zn_xte$ spectrometers for gamma and x-ray applications. *Semiconductors and Semimetals*, 43:335–381, 1995.

[10] T.E. Schlesinger et al. Cadmium zinc telluride and its use as a nuclear radiation detector material. *Material Science and Engineering*, 32:103–189, 2001.

[11] A. Zappettini et al. Boron oxide fully encapsulated cdznte crystals grown by the vertical bridgman technique. *Journal of Crystal Growth*, 307:283–288, 2007.

[12] C. Szeles et al. Growth and properties of semi-insulating cdznte for radiation detector applications. *SPIE proc.*, 3446:2–9, 1998.

[13] P. Rudolph et al. Defects in cdte bridgman monocrystals caused by nonstoichiometric growth conditions. *Journal of Crystal Growth*, 128:582–587, 1993.

[14] A.E. Bolotnikov et al. Cumulative effects of te precipitates in cdznte radiation detectors. *Nuclear Instruments and Method in Physics Research A*, 571:687–698, 2007.

[15] A. Zappettini et al. Stoichiometric deviations and partial-pressure measurements in solid-vapour cadmium telluride system. *Materials Chemistry and Physics*, 66:138–142, 2000.

[16] R. Grill and A. Zappettini. Point defects and diffusion in cadmium telluride. *Progress in Crystal Growth and Characterization of Materials*, 48-49:209–244, 2004.

[17] U. Becker et al. Characterization of p-type cdte bridgman crystals by infrared extinction spectra. *Physica Status Solidi (a)*, 120:653–660, 1990.

[18] R. J. Pieper and A. Korpel. Image processing for extended depth of field. *Appl. Opt.*, 22:1449–1453, 1983.

[19] A.E. Bolotnikov et al. Effect of te inclusions on the performance of cdznte radiation detectors. *IEEE Transactions on nuclear science*, 55:2757–2764, 2008.

[20] G. P. Sini. *Problemi tecnici della microscopia ottica.* 2005.

[21] N. Zambelli and A. Zappettini. Patent. a method and system for the three-dimensional reconstruction of formations dispersed in a matrix of a material, in particular of inclusions in crystalline matrices, 09 2013.

[22] A. Zappettini et al. Boron oxide encapsulated vertical bridgman grown cdznte crystals as x-ray detector material. *IEEE Trans. Nuc. Sci.*, 56:1743–1746, 2009.

[23] L. Marchini et al. Characterization of czt crystals grown by the boron oxide encapsulated vertical bridgman technique for the preparation of x-ray imaging detectors. *Nuclear Instruments and Method in Physics Research A*, 633:S92–S94, 2011.

[24] P. Rudolph et al. Distribution and genesis of inclusions in cdte and (cd,zn)te single crystals grown by the bridgman method and by the travelling heater method. *Journal of Crystal Growth*, 147:297–304, 1995.

[25] A. Zappettini et al. Growth and characterization of czt crystals by the vertical bridgman method for x-ray detector applications. *IEEE Trans. Nucl. Sci.*, 58:2352–2356, 2011.

[26] M. Zha et al. Heat treatment in semi-closed ampoule for obtaining stoichiometrically controlled cadmium telluride. *J. Crystal Growth*, 237:1720–1725, 2002.

[27] M. Zha et al. Full encapsulated vertical bridgman method. *J. Crystal Growth*, 310:2072–2075, 2008.

[28] L. Marchini et al. Study of surface treatment effects on the metal-cdznte interface. *IEEE Trans. Nucl. Sci.*, 56:1823–1826, 2009.

[29] M. Prokesch and C. Szeles. Accurate measurement of electrical bulk resistivity and surface leakage of cdznte radiation detector crystals. *J. Appl. Phys.*, 100:14503–14509, 2006.

[30] G.A. Carini et al. High-resolution x-ray mapping of cdznte detectors. *Nuclear Instruments and Methods in Physics Research Section A*, 579:120–124, 2007.

[31] G.A. Carini et al. Effects of te precipitates on the performance of cdznte detectors. *Appl. Phys. Letters*, 88:143515–1–3, 2006.

[32] A. E. Bolotnikov et al. Extended defects in cdznte radiation detectors. *IEEE Trans. Nucl. Sci.*, 56:2757–2764, 2009.

[33] A. E. Bolotnikov et al. Modelling the effects of te precipitates on the electron transpoirt in cdznte radiation detectors. *Nuclear Instruments and Methods in Physics Research Section A*, 579:125–129, 2007.

[34] K. H. Kim et al. Defect levels of semi-insulating cmt: In crystals. *J. Appl. Phys.*, 109:113715, 2011.

[35] F. Bissoli et al. Stoichiometry related defects in cdte crystals. *Phys. Stat. Sol. C*, 1:735–738, 2004.

[36] G. Yang et al. Low-temperature, spatially resolved micro-photoluminescence mapping in cdznte single crystals. *Appl. Phys. Letters*, 98:261901, 2011.

[37] A. Burger et al. Investigation of electrical contacts for cdznte nuclear radiation detectors. *IEEE Trans. Nucl. Sci.*, 44:934–938, 1997.

[38] A. A. Rouse et al. Interfacial chemistry and the performance of bromine-etched cdznte radiation detector devices. *IEEE Trans. Nucl. Sci.*, 49:2005–2009, 2002.

[39] J. Franc et al. Cdte and cdznte crystals for room temperature gamma-ray detectors. *Nucl. Instrum. Meth. in Phys. Res. A*, 434:146–151, 1999.

[40] W. Stadler et al. Optical investigations of defects in $cd_{1-x}zn_xte$. *Phys. Rev. B*, 51:10619–10630, 1995.

[41] H. Hermon et al. Evaluation of czt crystals from the former soviet union. *Nucl. Instrum. Meth. Phys Res. A*, 428:30–37, 1999.

[42] K. Lischka et al. Deep donor levels due to isolated fe in cdte. *J. Cryst Growth*, 72:335–359, 1985.

[43] R. Kernocker et al. Luminescence of fe^+-implanted cdte. *J. Cryst Growth*, 86:625–628, 1988.

[44] M. Chu et al. Tellurium antisites in cdznte. *Appl. Phys. Lett.*, 79:2728–2730, 2001.

[45] V. Babentsov et al. Photoluminescence and electric spectroscopy of dilocations-induced electronic levels in semi-insulating cdte and cdznte. *J. Luminescence*, 130:1425–1430, 2010.

[46] E. S. Elshazly and G. Tepper. Correlation of tellurium inclusions and carrier lifetime in detector grade cadmium zinc telluride. *Appl. Phys. Lett.*, 93:042112–042112, 2008.

[47] G. Yang et al. Post-growth thermal annealing study of cdznte for developing room-temperature x-ray and gamma-ray detectors. *Journal of Crystal Growth*, 379:16–20, 2013.

[48] P. Yu et al. Effect of te atmosphere annealing on the properties of cdznte single crystals. *Nuclear Instruments and Method in Physics Research A*, 643:53–56, 2011.

[49] G. Li et al. Thermal treatment of detector-grade cdznte. *Nuclear Instruments and Method in Physics Research A*, 643:31–35, 2011.

[50] J. Franc et al. Melt growth and post-grown annealing of semiinsulating (cdzn)te by vertical gradient freeze method. *Crystal Research and Technology*, 48:214–220, 2013.

[51] K. H. Kim et al. Temperature-gradient annealing of cdznte under te overpressure. *Journal of Crystal Growth*, 354:62–66, 2012.

[52] M. Meier et al. Laser-induced thermomigration of te precipitates in cdznte crystals. *Journal of Crystal Growth*, 311:4247–4250, 2009.

[53] J. H. Greenberg. Vapor pressure scanning implications of cdte crystal growth. *Journal of Crystal Growth*, 197:406–412, 1999.

[54] S. Sen et al. Crystal-growth of large-area single-crystal cdte and cdznte by the computer-controlled vertical modified-bridgman process. *Journal of Crystal Growth*, 86:111–117, 1988.

[55] K. C. Mills. *Thermodynamic data for inorganic sulphides, selenides and tellurides.* Butterworths (London), 1974.

[56] M. J. Soileau et al. Laser-induced damage measurements in cdte and other ii-vi materials. *Applied Optics*, 21:4059–4062, 1982.

[57] D. de Nobel. Phase equilibria and semiconducting properites of cadmium telluride. *Philips Res. Repts.*, 14:361, 1959.

[58] A. Raulo et al. Ion beam (rbs) and xrf analysis of metal contacts deposited on cdznte and cdte crystals. *IEEE Trans. Nucl. Sci.*, 58:1964–1971, 2011.

[59] M. Age Ali et al. Cdte nuclear detector electroless contact studies - new results on contact structures, interfaces and stress. *IEEE Nucl Sci. Symp. Conf. Ref.*, 5:3300, 2004.

[60] M. Roumie et al. Ion beam analysis of cdte nuclear detector contact grown by electroless process. *Nucl. Instrum. Meth. B*, 240:386, 2005.

[61] Jie Hu et al. Meniscus-confined three-dimensional electrodeposition for direct writing of wire bonds. *Science*, 329:313, 2010.

[62] C. Laslau et al. Scanned pipette techniques for the highly localized electrochemical fabrication and characterization of conducting polymer thin films, microspots, microribbons, and nanowires. *Adv. Funct. Mater.*, 21:4607, 2011.

[63] Q. Zheng et al. Electroless deposition of au, pt, or ru metallic layers on cdznte. *Thin Solid Films*, 525:56–63, 2012.

[64] A. E. Bolotnikov et al. Development of high spectral resolution cdznte pixel detectors for astronomical hard x-ray telescopes. *Nuclear Instruments and Methods in Physics Research A*, 458:585–592, 2001.

[65] Y. Du et al. Monte carlo investigation of the charge sharing effects in 3-d position sensitive cdznte gamma ray spectrometers. *IEEE Trans. Nuc. Sci.*, 46:844–847, 1999.

[66] A. E. Bolotnikov et al. Effects of bulk and surface conductivity on the performance of cdznte pixel detectors. *IEEE Trans. Nucl. Sci.*, 49:1941–1948, 2002.

[67] M. Pavesi et al. Czt x-ray detectors obtained by the boron encapsulated vertical bridgman method. *Proc. SPIE*, 6706:670, 2007.

[68] Y. Nemirovsky et al. Study of contacts to cdznte radiation detectors. *J. Electronic Materials*, 26:756–764, 1997.

[69] M. Roumie et al. Depth profiling and stoichiometry of constituents in platinum electroless contacts on cdte(111) under different ph values. *Thin Solid Films*, 515:7843, 2007.

[70] Q. Zheng et al. Comparison of radiation detector performance for different metal contacts on cdznte deposited by electroless deposition method. *Cryst. Res. Technol.*, 46:1131, 2011.

[71] I. Kuvvetli et al. Czt drift strip detectors for high energy astrophysics. *Nuclear Instruments and Method in Physics Research A*, 624:486–491, 2010.

[72] E. Gatti and P. Rehak. Czt drift strip detectors for high energy astrophysics. *Proceedings of 1983 DPF Workshop on Collider Detectors*, 624:97, 1983.

[73] M.A.J. van Pamelen and C. Budtz-Jorgensen. boh. *Nucl. Instr. and Meth.*, 403:390, 1998.

[74] I. Jung et al. Thick pixelated czt detectors with isolated steering grids. *IEEE Nucl Sci. Symp. Conf. Ref.*, N10-5:206–210, 2005.